PÁZMÁNY PÉTER CATHOLIC UNIVERSITY

FACULTY OF INFORMATION TECHNOLOGY AND BIONICS

ROSKA TAMÁS DOCTORAL SCHOOL OF SCIENCES AND TECHNOLOGY

NÉMETH, Afrodité

Role of extracellular vesicles in cancer progression and diagnosis

PhD Dissertation

Supervisor:

Tamás Márton Garay PhD

2025

Abstract:

Extracellular vesicles (EVs) are nanoscale, membrane-bound particles that mediate intercellular communication by transferring bioactive molecules. Present in all body fluids, EVs can be isolated and analyzed as potential biomarkers in malignancies.

The aim was to elucidate the functional role of EVs in melanoma progression, specifically examining their contribution to primary tumor growth versus metastatic dissemination. Using pairs of syngeneic melanoma cell lines, EVs were found to exert minimal influence on 2D proliferation and 3D spheroid growth, yet markedly enhanced single-cell migration, implicating a predominant role in metastasis formation. This pro-migratory effect persisted under BRAF inhibitor (BRAFi) treatment (vemurafenib, dabrafenib), particularly with EVs derived from resistant cell lines. However, EVs from cell lines derived from patients who had received BRAFi treatment alone showed limited ability to overcome migration inhibition under combined BRAFi and MEKi therapy. To better model resistance, new melanoma lines with acquired resistance to both BRAFi and MEKi were generated. Only EV-preconditioned cells exhibited partial rescue of migration under dual inhibition, indicating a possible role for EVs in supporting adaptive resistance mechanisms related to cell motility.

In parallel, the biomarker potential of EVs was assessed using pleural effusion (which represents the pleural disease microenvironment) samples from patients with non-small cell lung cancer (NSCLC), pleural mesothelioma (PM), and pleuritis (benign control). Surface marker profiling of isolated EVs (37 markers) revealed disease-specific patterns: CD326 was elevated in NSCLC, CD44 and MCSP in PM, and CD8 in pleuritis. Marker differences (CD4, CD44) were also detected between epithelioid and non-epithelioid PM subtypes. A machine learning algorithm was applied to classify patients based on EV profiles, and classified most of the patients into their respective groups. Furthermore, the algorithm was able to detect classification errors and achieved the highest accuracy when patients with secondary malignancies were excluded (ROC_{AUC}: NSCLC 0.81, PM 0.95).

Together, these findings highlight the functional role of EVs in promoting melanoma cell migration and therapy resistance, and their diagnostic utility in thoracic malignancies. EVs thus represent both therapeutic targets and potential biomarker in cancer research.

Table of Contents

1. List of abbreviations

ADC	Adenocarcinoma
AUC	Area Under the Curve
Bini	Binimetinib
BRAFi	BRAF inhibitor
CAF	Cancer-associated fibroblast
cfDNA	cell-free DNA
CI	Combination index
CTC	Circulating tumor cells
ctDNA	Circulating tumor DNA
Dabr	Dabrafenib
DMEM	Dulbecco's Modified Eagle's Medium
ECM	Extracellular matrix
EMT	Epithelial-mesenchymal transition
Enco	Encorafenib
EpCam	Epithelial cancer marker
EV	Extracellular vesicle
FBS	Fetal bovine serum
IQR	Interquartile range
lncRNA	long non-coding RNA
LOOCV	Leave-one-out cross-validation
MCSp	Melanoma chondroitin sulfate proteoglycan
MEKi	MEK inhibitor
miRNA	microRNA

mRNA	messenger RNA
MSD	Mean square displacement
nFCM	Nano-flow cytometry
NSCLC	Non-small cell lung cancer
ORR	Objective response rate
OS	Overall survival
PBS	Phosphate buffered saline
PD-L1	Programmed death-ligand 1
PE	Pleural effusions
PFS	Progression-free survival
PM	Pleural mesothelioma
PSA	Penicillin-streptomycin-amphotericin
Res	Resistant
ROC	Receiver operating characteristics
RT	Room temperature
SCC	Squamous cell carcinoma
SEC	Size exclusion chromatography
Sens	Sensitive
SCLC	Small cell lung cancer
SPV	Sulfophosphovanillin
SRB	Sulforhodamine B
TME	Tumor microenvironment
Tram	Trametinib
TTD	Total travelled distance
Vem	Vemurafenib

2. Introduction

During my PhD, my primary focus was to develop expertise in the field of extracellular vesicles (EVs) within the context of cancer biology. In parallel, I explored the potential of EVs as biomarkers in pleural effusion samples from patients with non-small cell lung cancer (NSCLC), pleural mesothelioma (PM), and pleuritis – leveraging the fact that EVs are present in all body fluids and that pleural effusions provide a direct window into the tumor microenvironment. As a relatively young and rapidly evolving field, EV research holds substantial promise for advancing our understanding of cancer progression and development of novel diagnostic strategies.

The following literature overview covers key findings on EVs in melanoma, targeted therapy resistance, as well as general background on thoracic malignancies and liquid biopsy approaches.

2.1. Extracellular vesicles: general characteristics and biological functions

Extracellular vesicles (EVs) are nanosized, lipid bilayer-enclosed particles released by basically all cells and incapable of independent replication. Initially considered as cellular waste or as byproducts released only under specific conditions. However, EVs are now recognized as critical mediators of intercellular communication, carrying valuable molecular information between cells [1].

EVs can be **categorized** based on their size or cellular origin. Small EVs (sEVs) are generally defined as vesicles smaller than 200 nm, while large EVs (lEVs) exceed this threshold. However, this size cut-off is not absolute, and differences in measurement techniques can affect the outcome of size-based fractionation. The term exosomes refers to vesicles formed via the endosomal pathway, released when multivesicular bodies (MVBs) fuse with the plasma membrane. These are considered a subtype of sEVs. In contrast, ectosomes (also known as microvesicles) are shed directly from the plasma membrane and may vary broadly in size [2]. There are additional vesicle types specific to certain cellular processes, such as apoptotic bodies released during programmed cell death [3] and migrasomes formed during cell migration [4]. However, distinguishing vesicles by their biogenetic origin remains challenging due to the lack of exclusive markers [2]. Many studies, use specific terms like 'exosome' or 'microvesicle' without always providing clear evidence of their biogenetic origin, which can sometimes lead to ambiguity. To ensure consistency, the term 'extracellular vesicles' (EVs) will be used throughout this dissertation as a general descriptor. Similarly, when referencing the literature, I will adopt the general EV term, rather than the specific terms used in the original studies.

EVs **cargo** includes diverse macromolecules such as lipids, proteins, multiple RNA types, DNA fragments, and various signaling molecules [5]. Transferred molecules can be classified either by their chemical structures or by the mechanisms through which they influence recipient cell function. However, as the functional mechanisms of many molecules remain unresolved, I will organize the discussion according to their chemical properties.

The intraluminal contents are encapsulated by the lipid bilayer, which protects them from enzymatic degradation. EV membranes consist of a variety of lipids, including glycerophospholipids, sphingolipids, and cholesterol, each with structural variants that can influence interactions with recipient cells. Lipid rafts within the membrane can also facilitate the activation of specific signaling pathways [6].

EVs can carry growth factors that regulate cellular proliferation, growth, and angiogenesis [7]. Their membrane often displays tetraspanins, integrins, and adhesion molecules, along with biogenesis markers such as Alix and TSG101, heat shock proteins, enzymes like ATPase (e.g. PMCA4, ATP1A3) and GAPDH, cytoskeletal proteins, and other cell-type-specific proteins [1]. Additionally, drug efflux transporters such as P-glycoprotein are present in EVs and may contribute to the removal of chemotherapy agents [8], [9]. Hormones have also been identified in certain EV types [10]. Moreover, EVs can present antigens via MHC molecules and influence immune activation [11]. Their cargo may also include pro- or anti-inflammatory cytokines and immunomodulatory proteins such as programmed death-ligand 1 (PD-L1), impacting immune responses [12], [13].

EVs are rich in various RNA species, including fragmented (25-4000 nt) and full-length messenger RNAs (400-12,000 nt), which may function differently from their parent transcripts [14]. Small non-coding RNAs such as microRNAs (miRNAs, 18-22 nt) can modulate gene expression in recipient cells by targeting mRNAs [15]. Long non-coding RNAs (lncRNAs, >200 nt) in EVs can influence transcriptional regulation [16]. Other, less characterized RNA species have also been found in EVs, including Y RNAs, circular RNAs, small nucleolar RNAs, small nuclear RNAs, piwi-interacting RNAs, transfer RNAs, and ribosomal RNAs [17]. Both single-stranded and double-stranded DNA – including genomic and mitochondrial DNA – can be present on the surface or within the lumen of EVs [18]. Additionally, they transport various metabolites, such as amino acids, nucleotides, and sugars [19].

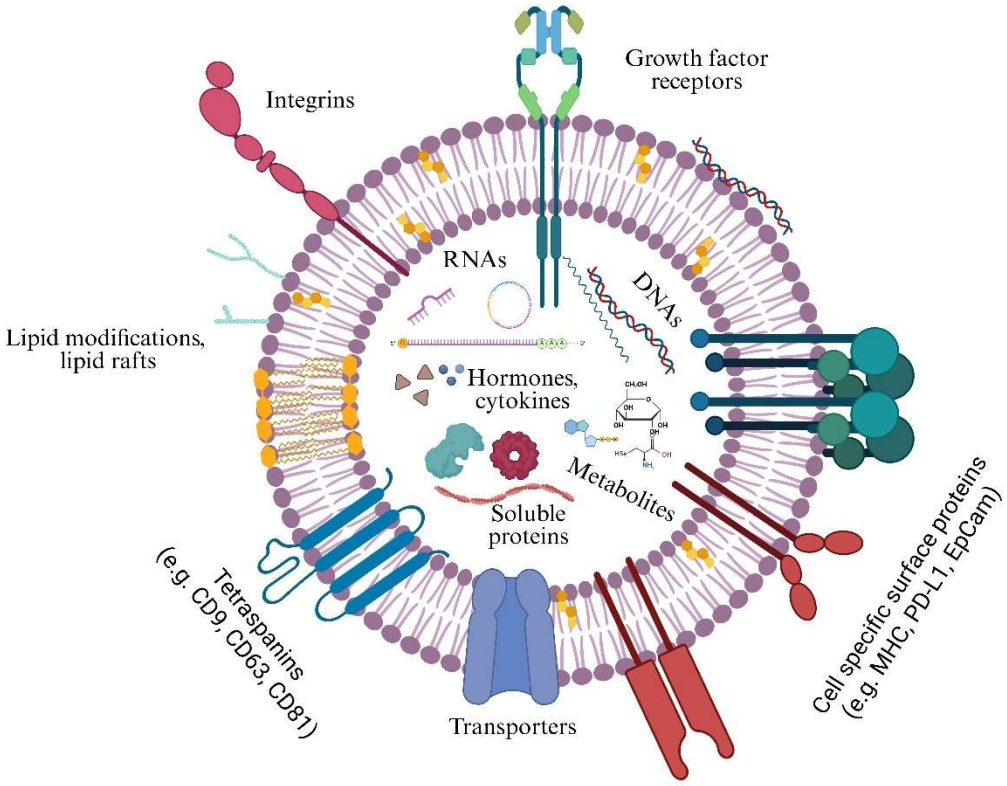

Figure 2.1. Representative image of extracellular vesicles cargo. *Their cargo includes diverse macromolecules such as lipids, proteins, multiple RNA types, DNA fragments, and various signaling molecules. Created with Biorender.com.*

EVs play a central role in intercellular communication by modulating the behavior of recipient cells. This can occur through surface binding, membrane fusion, or endocytic uptake [20]. EVs are involved in a wide range of **physiological processes**, including fertilization [21], [22], embryonic development [23], neural communication [24], and immune regulation [25]. They also contribute to the pathogenesis of numerous diseases, including cancer [26], neurodegenerative disorders [27], cardiovascular diseases [28], diabetes [29], autoimmune conditions [30], and viral infections [31].

EVs are present both in the immediate cellular microenvironment and in various **body fluids**, allowing them to reach distant organs [32]. They can be found in blood [33], pleural fluid [34], amniotic fluid [35], cerebrospinal fluid [36], lymph [37], saliva [38], urine [39], and breast milk [40]. Thus, isolating EVs from these fluids holds significant promise for their use as prognostic and predictive biomarkers [41] - [43].

2.2. Tumor progression

2.2.1. From cellular homeostasis to tumor initiation

Cells in the human body are inherently cooperative, relying on complex systems of communication to maintain tissue homeostasis. Under normal physiological conditions, cells tightly regulate their responses to extracellular signals: they divide only in response to specific signals, refrain from proliferating when damaged beyond repair, and do not migrate away from their tissue of origin. This tightly regulated behaviour ensures that individual cells serve the greater functional integrity of the organism [44], [45].

However, over the course of an individual's lifetime, somatic cells can acquire **genetic alterations** that confer selective advantages [46]. These mutations may occur spontaneously during DNA replication or be induced by environmental factors such as chemical carcinogens [47] - [50], ionizing radiation [51], [52], or ultraviolet (UV) light [53], [54]. Individuals with inherited defects in DNA repair mechanisms are especially prone to accumulating such mutations and, consequently, face an increased cancer risk [55], [56].

Over time, successive rounds of cell division may lead to the accumulation of further mutations and epigenetic modifications, resulting in deregulated gene expression [57]. These altered cells may gain the ability to bypass cell cycle checkpoints, evade apoptosis, and sustain uncontrolled proliferation. As a result, a **clonal population** of abnormal cells can emerge, forming a tumour or neoplasm. Within the growing tumour mass, genetic instability and selective pressures foster the emergence of subclonal populations. These subclones compete for dominance, with the most aggressive variants often gaining a proliferative or survival advantage [58], [59]. The dynamic interplay between tumour cells and their microenvironment – including stromal components, immune cells, and the extracellular matrix – further influences disease progression and therapeutic resistance [60], [61].

Tumors are broadly **categorized** based on their tissue of origin. Carcinomas, which arise from epithelial cells, represent the most common cancer type in humans. Sarcomas originate from connective tissue or muscle cells. Hematologic malignancies include leukemias and lymphomas, which derive from hematopoietic cells and lymphoid tissues, respectively. Tumors may also emerge from the nervous system, either as primary brain tumours or peripheral nerve sheath neoplasms [62].

2.2.2. Local invasion and migration

If the growth remains confined to the tissue of origin, the tumor is considered benign and may be curable through surgical excision. However, when cells acquire the capacity to invade surrounding tissues and breach the basement membrane, they are classified as malignant [44], [45]. Malignant cells may further develop the ability to intravasate into the bloodstream or lymphatic vessels, disseminate to distant sites, and establish secondary tumours – a process known as metastasis formation [63], [64]. Disruption of the adhesive behaviour is one of the first steps of metastasis formation, during this process carcinomas undergo epithelial-mesenchymal transition (EMT). They downregulate adhesion molecules such as E-cadherin, remodel the actin cytoskeleton, and secrete proteolytic enzymes (e.g., matrix metalloproteinases (MMP) to degrade components of the extracellular matrix (ECM) [65]. Cell migration is a critical component of the metastatic process. Cancer cells can adopt various migratory modes – such as mesenchymal, amoeboid, or collective migration – and often transition between them in response to microenvironmental signals, enabling them to navigate through tissue and ultimately access blood vessels nearby [66] - [68].

2.2.3. Metastatic dissemination and colonization

Lymphatic vessels, being wider than blood capillaries, allow cancer cells to enter in clusters; these clusters may become lodged in lymph nodes, giving rise to lymph node metastases [69]. In contrast, **circulating tumour cells** (CTCs) found in the bloodstream typically travel as single cells, however, due to immune surveillance, only a small fraction survive to reach distant sites [70].

Organotropism – the tendency of certain cancers to metastasize preferentially to specific organs – is governed by a complex interplay between tumour-intrinsic properties and the microenvironment of potential target sites. This phenomenon aligns with Paget's classical *"seed and soil" theory* [71], which posits that metastatic dissemination depends not only on the characteristics of the cancer cells (the "seeds") but also on the receptivity of the distant organ microenvironment (the "soil") [72]. Tumor cells may express specific surface receptors, integrins, or chemokine receptors that guide them toward favourable environments [73]. Furthermore, the anatomical distribution of blood and lymphatic vessels significantly influences metastatic dissemination. The pattern and diameter of lymphatic and blood vessels can determine which organs or tissues are more accessible to circulating tumour cells, thereby contributing to the organotropism observed in different cancers [62]. Simultaneously, target tissues can be primed

by tumour-secreted factors (such as extracellular vesicles) to form a so-called pre-metastatic niche – a supportive environment that facilitates tumour cell adhesion, survival, and colonization [32].

Following extravasation, disseminated tumour cells encounter a foreign microenvironment that is not inherently supportive of growth. Many cells enter a state of dormancy, remaining quiescent for extended periods. Successful **colonization**, the final step of metastasis, involves adaptation to the local tissue niche, evasion of immune responses, and reactivation of proliferative programs. The few cells that survive and adapt can give rise to clinically detectable secondary tumours [74], [75].

Despite the inefficiency of the metastatic cascade, the emergence of even a small number of viable metastatic lesions often marks a turning point in disease progression and is associated with poor prognosis [76]. Understanding the molecular and cellular mechanisms underlying each step of this process remains essential for the development of therapies aimed at preventing or halting metastasis.

2.2.4. Extracellular vesicles in cancer progression

EVs act as critical mediators of intercellular communication, from local remodeling of the primary tumor microenvironment to systemic effects on immune modulation and metastatic spread [26]. Therefore, tumor-derived extracellular vesicles play pivotal roles in nearly every stage of cancer progression.

Rather than providing an exhaustive review of the field, this section aims to illustrate the major mechanisms through which EVs contribute to cancer progression, using representative and well-established examples from the literature.

2.2.4.1. EV-mediated remodelling of the primary tumor microenvironment

Cancer progression is profoundly influenced by the dynamic interplay between malignant cells, the tumor microenvironment, and distant tissues. Cancer cells secrete EVs at higher levels than their non-malignant counterparts, contributing to the remodeling of the tumor niche and facilitating metastatic dissemination [77].

EVs mediate the **horizontal transfer** of oncogenic signals among cancer cells by delivering proteins such as PDGFR, Met, β-catenin, Ras, and Akt, as well as RNAs that promote more

aggressive phenotypes, such as altered morphology, increased proliferation, enhanced invasion, accelerated colony formation [78]. Notably, studies suggest that oncogenic DNA could be also transferred via EVs [79], [80]. Furthermore, they can enhance migration by promoting the formation of nascent adhesions, filopodia, and invadopodia [81] - [83].

Beyond influencing cancer cell behavior, EVs actively **reprogram the tumor microenvironment** [84]. For instance, in mesothelioma, EVs enriched in membrane-bound TGF-β and betaglycans can induce fibroblast-to-cancer-associated fibroblast (CAF) differentiation [85]. Moreover, melanoma-derived EVs have been shown to transfer miRNAs that stimulate CAF proliferation, migration, and proinflammatory activation [86]. In models of metastatic adenocarcinoma, tumor-derived miRNAs within EVs upregulate matrix metalloproteinases (MMPs) while suppressing cadherin expression in fibroblasts, thereby promoting extracellular matrix (ECM) remodeling and the formation of a more invasion enabling niche [87]. Importantly, this communication is bidirectional; CAF-derived EVs have also been reported to support the migratory capacity of breast cancer cells [88], [89]. Furthermore, tumour-derived extracellular vesicles can drive the differentiation of mesenchymal stem cells and other bone marrow-derived cells into tumour-supportive phenotypes via delivering TGFβ and specific miRNAs [90]. EVs contribute to the direct remodeling of the ECM by promoting proteolytic degradation and the deposition of ECM components [91].

EVs could also facilitate **angiogenesis**, the formation of new blood vessels by transferring angiogenic factors to endothelial cells. For instance, EVs from lung and colorectal cancer cells have been shown to transfer EGFR to endothelial cells, activating MAPK and AKT pathways and enhancing VEGF signaling [92]. Hypoxia further amplifies this process, as seen in glioblastoma and colorectal cancer, where EVs enriched in tissue factor, miRNAs, or Wnt4 stimulate endothelial proliferation, vessel maturation, and tumour vascularization [93], [94].

In addition to modulating cellular behavior, EVs contribute to tumor invasiveness through the transport of proteolytic enzymes such as MMPs, which facilitate ECM degradation [95]. Extracellular vesicles deposited by migrating cells can act as pathfinding cues, guiding the directional movement of follower cells [96].

2.2.4.2. Systemic impact of tumor-derived extracellular vesicles in cancer progression

In addition to mediating local microenvironmental changes, tumor-derived EVs can enter the circulation and exert systemic effects by interacting with distant recipient cells [1]. Once in the bloodstream, EVs can contribute to a pro-thrombotic state by promoting **coagulation** [97].

Notably, elevated levels of coagulation factor–enriched EVs have been detected in cancer patients, correlating with an increased risk of thrombosis [98].

Tumor-derived EVs are also key players in systemic **immunosuppression** [99]. EVs carrying programmed death-ligand 1 (PD-L1) have been shown to promote T cell exhaustion, thereby impairing anti-tumor immunity [13]. In head and neck squamous cell carcinoma, the abundance of PD-L1-positive EVs is associated with disease progression [100]. Additional immune regulatory molecules packaged in EVs, such as arginase-1 from ovarian cancer cells, interfere with dendritic cell (DC)–mediated antigen presentation and diminish $CD8^+$ T cell cytotoxicity [101]. Similarly, tumor EVs can suppress natural killer (NK) cell function by upregulating the NKG2D ligand and serving as decoys for receptor binding [102]. Glioblastoma-derived EVs containing the LGALS9 ligand have also been shown to inhibit antigen processing in DCs through interaction with the TIM3 receptor, further impairing anti-tumor immune responses [103].

EVs have been shown to drive **organotropic metastasis** by preferentially interacting with specific resident cells in target organs, such as lung fibroblasts and epithelial cells, liver Kupffer cells, and brain endothelial cells. This organ-specific interaction is mediated by distinct integrins on EVs – α6β4 and α6β1 for lung metastasis, and αvβ5 for liver metastasis [104]. Furthermore, EVs from pancreatic ductal adenocarcinoma (PDAC) promote liver pre-metastatic niche formation by recruiting bone marrow-derived macrophages and enhancing fibronectin deposition via macrophage migration inhibitory factor (MIF) [105]. Additionally, tumor EVs have been implicated in compromising **vascular integrity**, such as disrupting the blood-brain barrier, to facilitate metastatic seeding in the brain [106]. These vesicles may also modulate the metabolic activity of recipient cells, creating a microenvironment that supports the survival and outgrowth of metastatic cancer cells [107].

2.3. Melanoma

Melanoma is originating from the malignant transformation of melanocytes, the pigment-producing cells of the skin. Although it accounts for only a small fraction of skin cancer cases, melanoma is responsible for the majority of skin cancer-related deaths due to its pronounced metastatic potential and treatment resistance [108], [109]. A deep understanding of its biological drivers and clinical challenges is essential to improving therapeutic strategies and patient outcomes.

2.3.1. Epidemiology and clinical overview

Melanoma incidence is rising faster than any other malignancy worldwide and is projected to continue increasing across most regions. According to the European Cancer Information System, the average incidence in the EU-27 stands at 11,9 cases per 100,000 inhabitants per year. However, this figure varies across countries; for example, Hungary reported an incidence of 8,4 per 100,000 for both sexes and all ages in 2020. Central and Eastern Europe bear the highest mortality burden, with 1,7 deaths per 100,000 inhabitants per year [110]. Crucially, prognosis depends on disease stage: while localized melanoma carries a five-year survival rate of ~90%, this decreases to approximately 16% in metastatic disease [111].

Ultraviolet (UV) radiation from sun exposure remains the predominant **risk factor** for melanoma development, with UVB (280-315 nm) causing direct DNA mutagenesis and UVA (315-400 nm) inducing indirect DNA damage via reactive oxygen species [112]. Additional risk factors include genetic susceptibility, family history, and the presence of melanocytic nevi (moles), where both total nevus count and nevus size correlate positively with melanoma risk [113], [114].

Clinically, melanoma **diagnosis** involves multiple steps. Dermoscopy is the frontline tool in practice, allowing clinicians to examine subsurface pigment patterns. Suspicious lesions undergo biopsy and histopathological evaluation [115]. Staging follows the American Joint Committee on Cancer (AJCC) guidelines: stages I and II reflect localized disease, stage III involves regional lymph node metastases, and stage IV indicates distant metastasis [116].

2.3.2. Molecular pathogenesis

Melanoma development is driven by a complex, multi-layered molecular landscape shaped by environmental, genetic, and epigenetic factors. As mentioned, UV radiation is a key environmental driver, inflicting both direct and indirect genomic damage. At the genetic level, **somatic mutations** in tumor suppressor genes and oncogenes disrupt normal regulatory mechanisms, promoting unchecked cell proliferation, survival, and dissemination [117].

Central to this process is the mitogen-activated protein kinase **(MAPK) pathway**, a pivotal signaling cascade governing cell proliferation, differentiation, survival, apoptosis, and cell migration. Under physiological conditions, extracellular stimuli such as growth factors activate receptor tyrosine kinases, triggering RAS activation and sequential downstream signaling through RAF, MEK, and ERK. This tightly regulated cascade ensures appropriate nuclear transcriptional responses, including modulation of key transcription factors (e.g., ETS, ELK-1, MYC), intracellular

regulators of apoptosis (e.g., BAD, BIM, MCL-1, BCL-2), and cytoskeletal regulators critical for cell motility [118], [119].

Importantly, aberrant MAPK signaling influences melanoma cell migration by modulating cytoskeletal dynamics (via targets like focal adhesion kinase, paxillin, and myosin light chain kinase) and upregulating matrix metalloproteinases, which degrade the extracellular matrix and promote invasive behavior. Additionally, MAPK-driven changes contribute to phenotypic plasticity and invasive switching, allowing melanoma cells to adapt and migrate efficiently within different tissue environments [44], [45].

In melanoma, mutations in components of this pathway – such as BRAF (37-50%), NRAS (13-25%), NF1 (12%), MAP2K1 (6-7%), KIT (2-8%), and others – are major oncogenic drivers, disrupting normal signal transduction and fostering malignant transformation [120]. Among **BRAF mutations**, the vast majority (~80-90%) involve the V600E substitution, where valine is replaced by glutamic acid at position 600, leading to constitutive activation of BRAF kinase activity. Less frequent but clinically relevant variants include V600K and V600R mutations [121], which also hyperactivate the pathway and contribute to melanoma progression. Beyond genetic alterations, epigenetic mechanisms – including DNA methylation, histone modifications, chromatin remodeling, and non-coding RNA dysregulation – further contribute to melanoma pathogenesis by reshaping gene expression landscapes [122].

The **tumor microenvironment (TME)** plays a crucial role in melanoma progression, invasion, and metastasis by driving metabolic reprogramming and altering various factors such as pH, oxygen levels, and extracellular matrix composition. The TME, enriched in cytokines, growth factors, and transcription factors, facilitates a "phenotypic switch" in melanocytes, promoting their transition from a proliferative to a dedifferentiated and invasive state, which enhances melanoma's metastatic potential [123].

2.3.3. Current therapies

The management of melanoma is highly stage-dependent. While early-stage melanomas are effectively treated with surgical excision, advanced or metastatic cases necessitate systemic therapies [124]. Among the most transformative systemic treatments are **immune checkpoint inhibitors**, which disrupt the mechanisms of immune tolerance by reactivating T cells, thereby enhancing tumor cell killing while limiting off-target inflammatory responses in normal tissues. A major therapeutic approach targets the interaction between programmed cell death protein 1

(PD-1) and its ligand PD-L1, reinvigorating exhausted T cells within the tumor microenvironment to restore their cytotoxic capacity. Agents such as nivolumab, pembrolizumab, atezolizumab, and durvalumab exemplify this strategy [125] - [127]. Another key immune checkpoint target is CTLA-4, a receptor expressed on activated regulatory T cells that normally serves to downregulate immune function; its inhibition by agents like ipilimumab enhances antitumor immune activity [126], [128].

In addition to systemic immunotherapies, **intralesional therapeutics** offer a complementary strategy by directly injecting agents into the tumor mass. For example, talimogene laherparepvec (T-VEC), a genetically modified herpes simplex virus type 1, selectively infects and replicates within tumor cells, inducing targeted lysis and stimulating local and systemic antitumor immune responses [129], [130]. Interleukin-2 (IL-2) therapy promotes the proliferation and activation of tumor-infiltrating lymphocytes, particularly cytotoxic T cells and natural killer (NK) cells, amplifying immune-mediated tumor clearance [131], [132].

Topical agents, including imiquimod and 5-fluorouracil (5-FU), provide additional therapeutic avenues. Imiquimod functions by activating toll-like receptors 7 and 8, enhancing cytokine production, stimulating both innate and adaptive immune responses, and inhibiting angiogenesis within the tumor microenvironment. In contrast, 5-FU, a pyrimidine analog, disrupts DNA synthesis in rapidly dividing tumor cells, leading to apoptosis. These locally applied agents can improve tumor control, particularly when combined with surgical or systemic therapies, by enhancing immune recognition or directly reducing residual malignant cells [133], [134].

Beyond these strategies, inhibitors targeting the mitogen-activated protein kinase (MAPK) pathway have become a fundamental aspect of **targeted** melanoma **therapy**. The subsequent section will focus on BRAF-targeted treatments, given that BRAF mutations are the most prevalent in melanoma [120].

2.3.3.1. BRAF-signalling targeted therapies

BRAF mutation in melanoma was identified in 2002 and its started a new era in the management of melanoma [135]. Early efforts to inhibit BRAF using non-RAF-isoform-selective inhibitors proved unsuccessful; however, later structure-based drug design approaches enabled the development of clinically effective BRAF-specific inhibitors. ***Vemurafenib*** was the first BRAF inhibitor to demonstrate a dramatic improvement in treatment outcomes for melanoma. In the phase III BRIM-3 trial, vemurafenib monotherapy significantly increased the objective response rate (ORR) from 5% (observed with dacarbazine chemotherapy) to 48%. Additionally, both median

progression-free survival (PFS) and overall survival (OS) were notably extended, reaching 5,3 months and 13,3 months, respectively [136], [137]. Following this, ***dabrafenib*** was developed as a second BRAF-targeted agent, showing comparable therapeutic efficacy, with an ORR of approximately 50% and a median PFS of 5,1 months [138]. The usual side effects of BRAF-inhibitor therapies are nausea, photosensitivity, fatigue, rash and arthralgia, notably these adverse effects are less frequent is dabrafenib usage. Unfortunately, despite an initial period of sensitivity, most melanoma cases eventually relapse and develop resistance to BRAF inhibitors. Moreover, patients treated with vemurafenib often exhibit a notable rise in the number of brain metastases [139], [140].

BRAF inhibitor **resistance** can occur with several **mechanisms**, and in the following section, I will outline some of the proposed pathways, which are visualized in Figure 2.3. Multiple studies have shown that it can arise through increased expression of various receptor tyrosine kinases, including AXL, EGFR, FGFR, PDGFRB, and IGF1R, whose activation does not necessarily imply BRAF activation. These receptors act as upstream activators of MAPK/ERK signaling, allowing resistant cells to bypass BRAF inhibition [141] - [144]. Besides receptor tyrosine kinase activation, BRAF inhibitor resistance can arise from secondary mutations or alternative splicing events within the MAPK/ERK pathway itself. These include additional BRAF mutations, NRAS or KRAS mutations, MEK1 alterations, or COT overexpression, all of which restore MAPK/ERK signaling. Such adaptations allow resistant melanoma cells to maintain proliferation and survival despite BRAF inhibition [145] - [147]. Beyond MAPK/ERK reactivation, BRAF inhibitor-resistant melanoma cells often activate alternative survival pathways, particularly PI3K/AKT signaling. This leads to upregulation of anti-apoptotic proteins like Mcl-1, activation of NF-κB, and secretion of factors that enhance both tumor cell survival and the supportive tumor microenvironment [148] - [150]. In addition to MAPK/ERK reactivation and PI3K/AKT-mediated survival, microRNAs (miRNAs) have emerged as key post-transcriptional regulators contributing to melanoma resistance [151]. Reduced levels of miR-200c, for example, increase the expression of proliferation and drug-resistance genes [152], while miR-579-3p directly targets BRAF [153]. Together, these mechanisms often cooperate within the same tumor, underscoring the complexity of BRAF inhibitor resistance and the need for combinatorial therapeutic strategies.

Given the complex and heterogeneous mechanisms underlying BRAF inhibitor resistance, combination strategies have been developed to enhance treatment efficacy. One of the most successful approaches has been the dual targeting of the MAPK pathway through **combined BRAF and MEK inhibition.** Clinical trials have shown that the combinations of ***vemurafenib-cobimetinib*** [154], [155] and ***dabrafenib-trametinib*** [156], [157] significantly improve response

rates, progression-free survival, and overall survival compared to BRAF inhibitor monotherapy. Notably, while both vemurafenib-cobimetinib and dabrafenib-trametinib and are highly effective, they differ in toxicity profiles: dabrafenib-trametinib is more often linked to febrile events (high fever), whereas vemurafenib-cobimetinib is associated with higher rates of cutaneous and gastrointestinal adverse effects [158]. More recently, the combination of ***encorafenib and binimetinib*** has emerged, showing further improvements in progression-free and overall survival compared to the earlier combinations [159]. Importantly, febrile events are less common with this regimen, although it carries a higher risk of serous retinopathy, while photosensitivity is most pronounced with vemurafenib-cobimetinib treatment [160]. Together, these findings have established BRAF–MEK inhibitor combinations as the standard of care for patients with BRAF-mutant melanoma, with the choice of regimen tailored to individual patient tolerability and clinical context.

Despite these advances, **resistance to combination therapy** remains a major clinical challenge, as most patients eventually experience disease progression [161]. Notably, in *in vitro* experiments, melanoma cells developed resistance to the encorafenib-binimetinib combination later than to the other combinations [162]. Although several mechanisms have been proposed – such as MAPK pathway reactivation, activation of alternative survival pathways, and receptor tyrosine kinase upregulation – the full spectrum of resistance processes is still not fully understood. Importantly, many of these adaptations are thought to contribute not only to BRAF inhibitor monotherapy resistance but also to resistance against BRAF-MEK inhibitor combinations [163], [164]. In recent years, extracellular vesicles have gained attention as potential mediators of drug resistance, contributing to these processes through intercellular communication, transfer of resistance-associated molecules, modulation of the tumor microenvironment and through drug sequestration [165]. The following section will explore the emerging role of EVs in melanoma targeted therapy resistance, highlighting their mechanisms and potential as therapeutic targets.

2.3.4. Extracellular vesicles in melanoma targeted therapy resistance.

Melanoma cells under targeted therapy produce EVs with altered cargo and these vesicles could effect resistant transfer and other changes in the recipient cells [165].

One key finding is that BRAF inhibitor treatment modifies the miRNA content of melanoma cell-derived EVs, particularly increasing levels of **miR-211-5p**, which has been associated with resistance. Cells with elevated miR-211-5p showed reduced sensitivity to vemurafenib, and

suppressing this miRNA in resistant cells impaired their proliferation. However, it remains to be clarified whether EVs can actively deliver functional miR-211-5p to sensitive cells [166].

Vella et al. [167] explored whether extracellular vesicles (EVs) released by BRAF inhibitor-resistant melanoma cells could transfer resistance traits to otherwise sensitive cells. They showed that resistant cells secreted EVs enriched in **PDGFRβ**, a receptor tyrosine kinase linked to PI3K/AKT pathway reactivation – one of the key mechanisms driving resistance to MAPK pathway inhibitors. When sensitive melanoma cells were exposed to these resistant-cell-derived EVs, they became less responsive to BRAF inhibitor treatment and showed dose-dependent activation of the PI3K/AKT pathway, with higher levels of pathway activation observed following greater EV exposure. Importantly, this EV-mediated resistance was not limited to one cell line, suggesting a broader relevance of PDGFRβ transfer in melanoma resistance [167].

A novel and particularly concerning study identified a truncated form of the **anaplastic lymphoma kinase (ALK) receptor**, termed ALK^{RES}, which is upregulated in several cancers, including melanoma [168]. This truncated variant plays a pivotal role in BRAF-inhibitor resistance by reactivating the MAPK pathway. When sensitive melanoma cells, which lack ALK^{RES}, were exposed to EVs derived from resistant cells (expressing ALK^{RES}), they exhibited a significant increase in IC50 for the BRAF inhibitor vemurafenib. Proteomic analysis of the EV cargo from resistant A375 cells revealed the presence of ALK^{RES}, and subsequent treatment of sensitive cells with these EVs demonstrated the transfer of ALK^{RES}. Confocal microscopy further confirmed the incorporation of ALK^{RES} into the sensitive recipient cells, where it remained functional, capable of activating the MAPK pathway [168]. These findings highlight the potential for EVs to transport not only regulatory molecules but also functional protein variants, which can directly alter the behavior of recipient cells.

These studies collectively demonstrate that EVs from BRAF inhibitor-resistant melanoma cells could transfer functional proteins, such as PDGFRβ and ALK^{RES}, as well as regulatory miRNAs like miR-211-5p. The altered cargo of EVs in response to BRAF inhibitor treatment is a key mechanism by which resistance can be transferred and propagated. In this dissertation, I aim to further investigate the role of EVs in vemurafenib resistance, with a specific focus on how these vesicles influence cell migration, a key process in melanoma progression. Additionally, I will explore the potential impact of EVs on resistance in combination therapies, which may offer new strategies to overcome the challenges of targeted therapy resistance in melanoma.

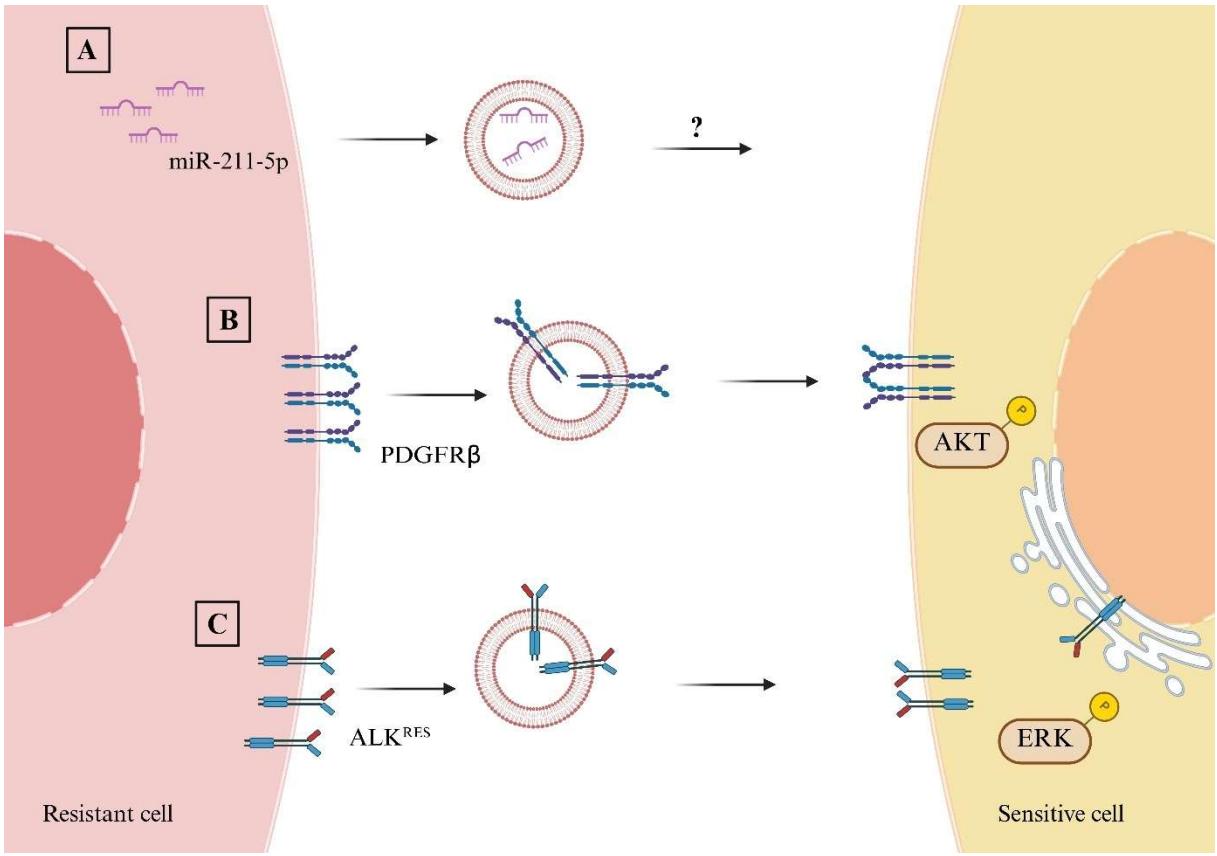

Figure 2.2. Extracellular vesicle (EV)-mediated mechanisms contributing to resistance against targeted therapy in melanoma. A) miR-211-5p expression is elevated in vemurafenib-resistant melanoma cells, and treatment with vemurafenib increases the EV-associated miR-211-5p levels. However, functional transfer of this miRNA to recipient cells was not assessed [166]; B) PDGFRβ is overexpressed in PLX-4720-resistant melanoma cells and is enriched in their secreted EVs. When these vesicles were applied to sensitive cells, a dose-dependent increase in AKT phosphorylation was observed [167]; C) A novel ALK isoform was identified in vemurafenib-resistant melanoma cells and detected in their EVs. Treatment of sensitive cells with these EVs resulted in functional transfer of the ALK protein. Confocal microscopy confirmed the presence of AKT in the cell membrane structures and cytoplasmatic regions. In addition, ERK phosphorylation levels were elevated in recipient cells [168]. Figure c*reated with Biorender.com*.

2.4. Thoracic diseases

Thoracic diseases include a wide range of malignant and non-malignant conditions affecting the lungs, pleura, mediastinum, and chest wall. These disorders range from highly aggressive tumors, such as non-small cell lung cancer (NSCLC) and malignant pleural mesothelioma, to benign yet clinically significant conditions like pleuritis [169], [170]. Thoracic malignancies represent a major global health burden, accounting for a substantial proportion of tumor-related mortality, with lung cancer alone being the leading cause of cancer deaths worldwide [171]. While the majority of research focuses on malignant diseases, benign pleural conditions are also clinically relevant, particularly when they lead to complications such as pleural effusion, which can mimic malignant presentations and complicate differential diagnosis [170].

From this point onward, this chapter will focus specifically on **non-small cell lung cancer (NSCLC)**, **pleural mesothelioma (PM)**, and **pleuritis**, as these three diseases form the basis of the experimental work described in this dissertation. NSCLC and mesothelioma represent the malignant thoracic diseases analyzed in this study, with pleuritis included as a benign control to highlight differences in EV profiles within the pleural environment.

2.4.1. Non-small cell lung cancer (NSCLC)

2.4.1.1. Epidemiology and clinical overview

According to the Global Cancer **Statistics** 2020 (GLOBOCAN) [172], lung cancer ranks as the second most commonly diagnosed cancer worldwide, following breast cancer, and remains the leading cause of cancer-related mortality among men. The incidence rate is notably higher in men (31,5 per 100,000 individuals) compared to women (14,6 per 100,000 individuals), with mortality patterns closely mirroring this distribution. Importantly, Eastern Europe reports some of the highest lung cancer incidence rates globally in both sexes, with Hungary exhibiting the highest incidence rate among females [172].

The main **risk factor** of lung cancer is smoking, which leads to 75 to 90% of all lung cancer cases. Beyond active tobacco smoking and second-hand smoke exposure, several environmental and occupational factors significantly elevate lung cancer risk, including a family history of lung cancer and exposure to carcinogenic agents such as radon gas, asbestos, arsenic, chromium, beryllium, and nickel. Additionally, certain medical conditions – such as pulmonary fibrosis and HIV infection – as well as alcohol consumption have also been implicated in lung cancer development [173], [174].

Lung cancer is broadly **categorized** into two major types: non-small cell lung cancer (NSCLC), which accounts for approximately 85% of cases, and small cell lung cancer (SCLC), comprising the remaining 15%. According to the World Health Organization (WHO), NSCLC is further divided into three principal histological subtypes: adenocarcinoma (40%), squamous cell carcinoma (25-30%), and large cell carcinoma (5-10%) [175].

2.4.1.2. Molecular pathogenesis of NSCLC

NSCLC develops through a series of genetic and epigenetic alterations that disrupt normal regulatory mechanisms and promote malignant transformation [176]. Several critical molecular drivers have been identified, particularly in adenocarcinoma, the most common NSCLC subtype. In the following section, the key molecular components involved in NSCLC pathogenesis, as

summarized in Figure 2.3, will be discussed. One of the most studied alterations is in the **epidermal growth factor receptor (EGFR)** gene [177]. These mutations, especially exon 19 deletions and exon 21 L858R point mutations, lead to constitutive kinase activation and persistent downstream PI3K/AKT and RAS/RAF/MEK/ERK signaling, driving uncontrolled proliferation and survival [177]. **KRAS** mutations, present in roughly 25-30% of NSCLC (particularly in smokers), act as another key oncogenic driver, promoting MAPK pathway activation independently of upstream receptor signaling [178]. **ALK** rearrangements, most commonly EML4-ALK fusions, are found in approximately 5% of NSCLC cases, typically among younger, non-smoking adenocarcinoma patients. These fusions result in constitutive ALK kinase activity and potent oncogenic signaling [179]. Similarly, **ROS1** [180] and **RET** [181] rearrangements, though less frequent, act as targetable oncogenic fusions in small subsets of NSCLC. Inactivation of tumor suppressor genes is another hallmark, especially **TP53** mutations [182], which impair genomic stability, and **STK11 (LKB1)** loss [183], which alters cellular metabolism and suppresses AMPK signaling. Epigenetic modifications, such as hypermethylation of promoters in genes like **CDKN2A (p16)** and **RASSF1A**, also play a crucial role in NSCLC pathogenesis by silencing tumor suppressor gene expression [184]. Furthermore, NSCLC tumors often escape immune surveillance through **PD-L1 overexpression**, which suppresses T cell activity via the PD-1/PD-L1 axis [185]. This has led to the development of immune checkpoint inhibitors targeting these pathways, transforming treatment outcomes for subsets of NSCLC patients [186].

Advances in understanding NSCLC's molecular mechanisms have led to breakthroughs in targeted therapies (e.g., EGFR, ALK, ROS1 inhibitors) and immunotherapies, significantly improving patient outcomes [186], [187]. However, beyond treatment advances, optimizing early and accurate diagnosis remains a critical challenge in clinical practice. Therefore, the following sections will specifically explore current and emerging diagnostic strategies for NSCLC, which are central to the objectives of this dissertation.

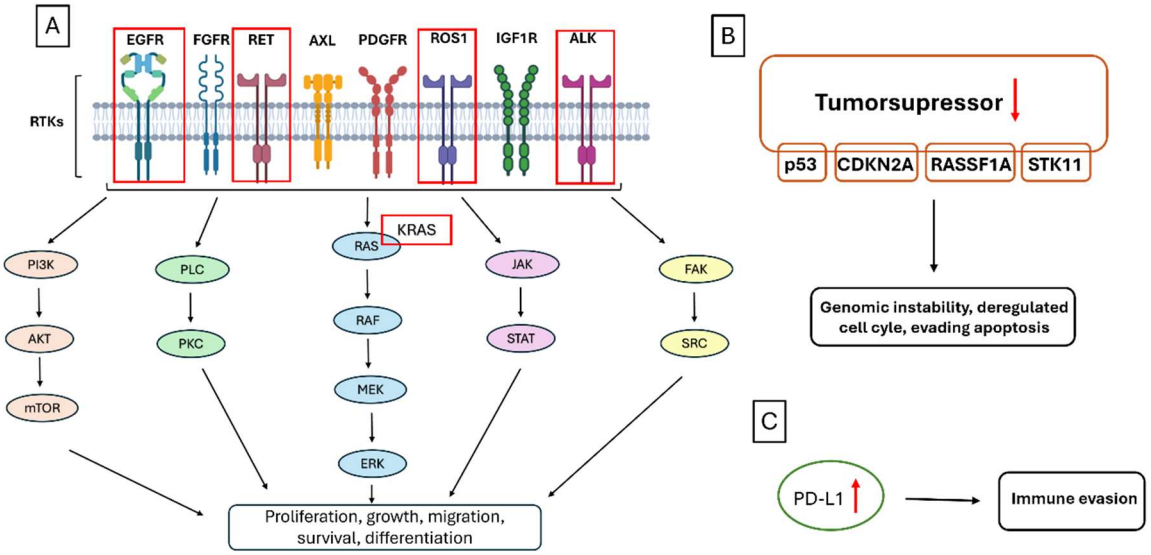

Figure 2.3. Overview of key cell signaling pathways in tumors. *A) Receptor tyrosine kinases (RTKs) and their downstream signaling cascades. Potential alternative pathways relevant to BRAF/MAPK signaling and red rectangles indicate critical molecular drivers in NSCLC pathogenesis; B) Frequently inactivated tumor suppressors and their downstream effects in NSCLC; C) PD-L1 overexpression on NSCLC facilitating immune evasion. Figure created with Biorender.com.*

2.4.1.3. Current diagnostic methods for NSCLC

The diagnosis of non-small cell lung cancer (NSCLC) relies on a combination of clinical evaluation, imaging, tissue sampling, and molecular analysis [188]. Patients commonly present with symptoms such as persistent cough, dyspnea, hemoptysis, unexplained weight loss, and chest pain. Pleural effusion, which can be observed as the accumulation of pleural fluid, is also a frequent clinical finding and may be indicative of malignancy. **Imaging techniques**, such as chest computed tomography (CT) and positron emission tomography (PET) scans, are used to assess the location and extent of disease. If radiographic findings are suspicious, **tissue diagnosis** is pursued through bronchoscopic biopsy, endobronchial ultrasound-guided needle aspiration (EBUS-TBNA), CT-guided transthoracic needle biopsy, or – in selected cases – surgical resection [186], [188], [189]. Once a diagnosis is established, molecular testing (such as EGFR, ALK, ROS1, KRAS, and PD-L1 status) is crucial to guide targeted and immunotherapy treatments [190].

However, while current diagnostic strategies remain essential, tissue biopsies are invasive, sometimes risky, tumor heterogeneity is not necessarily captured, often yield limited material, especially in patients with advanced or metastatic disease. These limitations have spurred growing interest in liquid biopsy approaches, which aim to detect and analyze tumor-derived components, such as circulating tumor DNA (ctDNA), circulating tumor cells (CTCs), microRNAs, and extracellular vesicles (EVs), from body fluids [191] – a topic that will be explored in more detail in a later section.

2.4.2. Pleural mesothelioma (PM)

2.4.2.1. Epidemiology and clinical overview

Malignant mesothelioma arises from the mesothelial cells lining the pleura. According to GLOBOCAN data, its **incidence** is approximately 0,5 per 100,000 men and 0,2 per 100,000 women [172]. Pleural mesothelioma (PM) represents about 80-90% of all mesothelioma cases, while the remaining cases develop in the peritoneum, pericardium, or tunica vaginalis [192]. Although PM is rare, it is highly aggressive, with a five-year survival rate of less than 5% [193]. Globally, its incidence is closely linked to past **asbestos exposure**, with a long latency period often exceeding 30-40 years between exposure and disease onset. While asbestos use has been banned or strictly regulated in many countries, cases continue to emerge due to historic exposure, and regions where asbestos is still in use report increasing incidence [194]. Other potential risk factors include asbestos-like minerals, ionizing radiation, carbon nanotubes, and certain oncogenic viruses [195].

Clinically, PM is typically classified into three main **histological subtypes**: epithelioid (the most common, with relatively better prognosis), sarcomatoid (associated with the poorest outcomes), and biphasic or mixed type, which contains both components [196].

2.4.2.2. Molecular pathogenesis of PM

PM develops from the malignant transformation of mesothelial cells, most commonly after prolonged asbestos exposure. Asbestos fibers penetrate the pleura and induce persistent inflammation, chronic oxidative stress, and DNA damage, creating a tumor-promoting microenvironment [194].

At the genetic level, PM is primarily driven by inactivation of **tumor suppressor genes** rather than activating oncogene mutations. Frequent alterations include deletions or mutations in **BAP1** (BRCA1-associated protein 1), **CDKN2A** (p16/INK4A, p14/ARF), and **NF2** (neurofibromin 2/merlin), which impair cell cycle regulation, DNA repair, and contact inhibition [197]. The Hippo signaling pathway, crucial for regulating proliferation and apoptosis, is often disrupted by NF2 loss, promoting uncontrolled growth [198].

Epigenetic changes, such as promoter methylation and histone modifications, further contribute to PM progression [199]. Additionally, chronic exposure to asbestos stimulates the release of cytokines like TNF-α and HMGB1, which enhance survival signaling and inflammation, fostering a pro-tumorigenic environment [200].

Despite advances in molecular profiling and the identification of therapeutic targets, translating these insights into effective treatments remains challenging. Current strategies include surgery, chemotherapy, emerging immunotherapies, and targeted therapies under clinical investigation, but overall outcomes remain poor [197]. However, these molecular insights have also opened new opportunities for improving diagnostics, which will be the focus of the following sections.

2.4.2.3. Current diagnostic methods for PM

PM typically presents with nonspecific symptoms, including chest pain, shortness of breath (dyspnea), chronic cough, fatigue, and unintended weight loss. A hallmark clinical feature is the accumulation of pleural effusion, which contributes to respiratory compromise and often prompts initial medical attention. Unfortunately, these vague symptoms often emerge only at advanced disease stages, leading to diagnostic delays [201].

The diagnosis of PM is based on integrating clinical assessment, imaging, and tissue confirmation. Initial clinical and **radiological evaluations** frequently reveal pleural abnormalities, such as effusion or thickening, on chest radiographs or CT scans [202]. However, definitive diagnosis requires **histopathological confirmation** from pleural tissue, most commonly obtained via thoracoscopy [203]. Immunohistochemistry is essential for differentiating PM from other pleural conditions, using markers such as calretinin, WT1, and cytokeratin 5/6 [204], [205]. Despite these established methods, current diagnostic strategies face several challenges. Many patients are diagnosed at late stages due to delayed symptom onset and nonspecific clinical signs. Furthermore, obtaining sufficient, high-quality tissue samples can be difficult, especially in patients with poor performance status or inaccessible lesions [196]. These challenges highlight the urgent need for improved, less invasive diagnostic tools, such as liquid biopsy approaches that will be explored later.

2.4.3. Pleuritis

Pleuritis, refers to inflammation of the pleural membranes surrounding the lungs. It is most often **caused by** viral or bacterial infections but can also arise secondary to autoimmune diseases (e.g., systemic lupus erythematosus, rheumatoid arthritis), pulmonary embolism, malignancies, or certain medications. Although pleuritis is generally a benign condition, it can still cause considerable clinical symptoms and discomfort [206].

Clinically, pleuritis typically presents with sharp, pleuritic chest pain that worsens with inspiration, coughing, or movement. Patients may also experience shortness of breath and pleural

friction rub on auscultation [207]. Imaging, such as chest X-ray or CT scan, may reveal pleural effusion or pleural thickening, but these findings are non-specific. In cases where malignant or infectious pleural disease is suspected, pleural fluid analysis (including cytology, microbiological tests, and biochemical markers) or pleural biopsy may be necessary to rule out malignancy or tuberculosis [208], [209].

Because pleuritis can produce pleural effusions that superficially mimic malignant pleural disease, it serves as an important non-malignant comparator in studies investigating pleural fluid as a diagnostic medium.

2.4.3. Liquid biopsies in NSCLC and PM

Liquid biopsy has emerged as a promising, minimally invasive tool for cancer diagnostics, offering an alternative or complement to traditional tissue-based methods. Unlike conventional biopsies, which require invasive sampling of tumor tissue, liquid biopsy analyzes tumor-derived materials circulating in body fluids. This approach enables real-time monitoring of tumor dynamics, detection of minimal residual disease, identification of resistance mechanisms, and, potentially, early diagnosis [191], [210]. In this section, I will discuss both **blood-based and pleural fluid-derived biomarkers**, highlighting blood as the most widely studied material in thoracic malignancy diagnostics, while also emphasizing pleural effusions – a valuable and underexplored alternative, which I investigate in my dissertation. Pleural effusion refers to the abnormal accumulation of fluid in the pleural space – the thin cavity between the visceral and parietal pleura surrounding the lungs [206]. Notably, the majority of malignant pleural effusions are linked to lung or breast cancer, while approximately 90% of PM cases are accompanied by pleural effusion [211]. This fluid typically contains a complex mixture of cellular components (including inflammatory cells, mesothelial cells, and, in malignancy, tumor cells), soluble proteins, nucleic acids, and extracellular vesicles. The pleural fluid microenvironment offers a more localized reflection of the tumor milieu than blood [212], [213]. Importantly, pleural effusions are routinely drained from patients as part of cytological examination to detect malignant cells, but the sensitivity of cytology is around 60%. On the other hand, pleural effusions are aspirated for symptomatic management also (e.g., to relieve dyspnea or chest discomfort), making them an accessible and ethically less invasive alternative source of diagnostic material [211]. This practical advantage, combined with the tumor-proximal nature of the fluid, motivated my choice to investigate pleural effusions as an alternative and potentially superior liquid biopsy material in thoracic malignancies.

While the term “liquid biopsy” can encompass a wide array of circulating biomarkers – including circulating tumor cells (CTCs), cell-free nucleic acids, extracellular vesicles (EVs), proteins, metabolites, and other soluble factors – there is currently no universally accepted definition regarding which components fall strictly under this umbrella term. Different research groups and reviews emphasize different aspects, and the field’s focus has evolved over time as new technologies and biomarker classes have emerged. In this chapter, without aiming to cover every molecular and analytical dimension of liquid biopsy, I will focus on the components that currently dominate research efforts: CTCs, cell-free nucleic acids, and EVs [191], [210].

Among the most widely studied components in liquid biopsy are **circulating tumor cells (CTCs)**, which are intact cancer cells shed from primary or metastatic tumors into the bloodstream. CTCs hold promise for early cancer detection, prognostic evaluation, and real-time treatment monitoring. However, their rarity poses major technical challenges for detection [214]. Currently, the CellSearch® system [215] is the only FDA-approved clinical platform for CTC enumeration from blood, used primarily in metastatic breast, prostate, and colorectal cancers. Its EpCAM-based capture approach, however, limits its utility in malignancies like pleural mesothelioma (PM), where tumor cells lack epithelial markers. In mesothelioma patients' blood, alternative platforms – such as podoplanin-targeting CTC-chips – have shown improved detection performance [216]. In NSCLC, several studies have demonstrated that CTC counts in blood can correlate with prognosis and treatment response, and experimental approaches have explored CTCs as early diagnostic markers [191], [217], [218]. Studies have also shown that the enumeration and characterization of CTCs from pleural fluid can provide prognostic information, help distinguish malignant from benign effusions, and potentially inform therapeutic decisions. For example, Lustgarten et al. [219] analysed the Cellsearch system on pleural effusions and demonstrated that high counts of pleural epithelial cells (PECs) could accurately distinguish malignant from benign effusions, even identifying malignancy in cases where standard cytology was negative. In another study, EpCam-based flow cytometry demonstrated higher sensitivity (91.9%) compared to cytology (70.3%) for diagnosing epithelial malignancies, while maintaining comparable specificity (98.7%) [220].

Circulating tumor DNA (ctDNA) refers to small fragments of tumor-derived DNA released into body fluids, through processes such as apoptosis, necrosis, or active secretion. It has become an extensively studied noninvasive biomarker, particularly in NSCLC. Blood-based ctDNA analyses are now widely implemented, with the European Medicines Agency (EMA) since 2014 recommending plasma ctDNA genotyping for patients where tissue samples are unavailable, underscoring its clinical relevance [191]. Numerous studies report significantly elevated ctDNA

levels in NSCLC patients compared to healthy controls or individuals with chronic respiratory diseases [221], [222], with strong correlations between ctDNA levels and tumor burden [223]. Importantly, blood-based ctDNA assays can robustly detect actionable mutations, including EGFR, ALK, BRAF, MET, ROS1, and NTRK alterations, with concordance rates as high as 94-100% compared to tissue-based next-generation sequencing (NGS) [224]. Notably, ctDNA testing has been shown to improve driver mutation detection by up to 65% when tissue material is limited or inaccessible, facilitating precision therapy decisions [225]. In parallel, pleural fluid-derived ctDNA have demonstrated substantial diagnostic value. Studies show that pleural effusion supernatants achieve high sensitivity (up to 89.5%) and specificity (up to 100%) for detecting mutations such as EGFR, KRAS, HER2, and fusions in ALK or ROS1, often outperforming cell blocks or cell pellets [226] - [228]. Meta-analyses further support the use of pleural effusion, as reliable surrogates for tumor tissue in EGFR mutation testing, with pooled sensitivities around 86% and specificities of 93% [229].

While blood-based ctDNA testing in mesothelioma is still emerging, recent studies have shown that personalized chromosomal junctions can be detected in plasma cfDNA in 78% of patients, with detection rates closely reflecting disease status [230]. Moving beyond plasma, pleural fluids have shown even greater potential. One study using whole-exome sequencing and droplet digital PCR (ddPCR) detected patient-specific somatic mutations in 94% of pleural fluid samples, with ctDNA levels similar to those in solid biopsies but far higher than in plasma [231]. Silvestri et al. [232] further reported that pleural fluids contain more single nucleotide variants (SNVs) than matched tumor biopsies, capturing mutations that would otherwise be missed in tissue alone. Additionally, Sriram et al. [233] demonstrated that the DNA integrity index in pleural fluids is significantly higher in PM patients compared to benign effusions, supporting its value as a diagnostic biomarker. Together, these findings highlight pleural fluids as a rich and underused source for molecular profiling and liquid biopsy in mesothelioma.

Besides quantitative and mutational analyses, cfDNA also carries epigenetic information, such as methylation patterns, which offer an additional layer of biomarker potential for cancer detection and characterization; accordingly, analysing the cfDNA methylation profile in both blood [234] - [236] and pleural effusion [237], [238] of NSCLC and mesothelioma has also gained increasing attention.

Despite its promise, ctDNA detection is limited by low abundance, short half-life, and background cfDNA, requiring highly sensitive methods such as ARMS, digital PCR, or NGS. Broader clinical use still awaits standardized protocols and validation in large trials [239].

MicroRNAs (miRNAs) are small non-coding RNAs that regulate gene expression and have emerged as promising non-invasive biomarkers for cancer detection. Several studies comparing miRNA profiles in lung cancer versus healthy tissue have identified promising panels for early detection. The plasma microRNA signature classifier (MSC) for lung cancer patients, built from 24 miRNAs, showed 87% sensitivity and 81% specificity in the MILD trial, and when combined with low-dose CT (LDCT), improved screening sensitivity from 84% (LDCT alone) to 98% [240]. A large meta-analysis covering 134 studies (6,919 lung cancer patients and 7,064 controls) reported circulating miRNAs' overall diagnostic performance with 83% sensitivity and 84% specificity, particularly highlighting multi-miRNA panels (like miR-21-5p, miR-223-3p, miR-155-5p, and miR-126-3p) as stronger biomarkers than single miRNAs [241].

Several circulating miRNAs have shown promise as PM biomarkers, with reported diagnostic sensitivities ranging from ~70% to 96% and specificities from ~61% to 90%. For example, low serum miR-126 levels, linked to high VEGF, differentiated PM from asbestos-exposed and healthy individuals and were associated with worse prognosis [242]. A combined panel of miR-126, SMRP, and methylated thrombomodulin improved diagnostic accuracy over SMRP alone [243]. Additional markers like miR-132 [244], miR-625-3p [245], and combinations such as miR-103a-3p + mesothelin [246] further enhanced discrimination. Interestingly, miR-1260a, miR-518f-3p, and miR-597-5p were specifically upregulated in lung adenocarcinoma, helping distinguish it from PM [247].

Recent studies have identified several miRNAs in pleural effusions that show distinct expression patterns in lung cancer. Shin et al. found significantly lower miR-134, miR-185, and miR-22 levels in malignant pleural effusions (MPE) compared to non-malignant cases ($p < 0.001$), and combining these miRNA profiles with carcinoembryonic antigen (CEA) measurements yielded a diagnostic sensitivity of 91.9% and specificity of 92.5% [248]. Additionally, miR-198 was expressed at lower levels in lung adenocarcinoma-associated MPE, and combining its measurement with CEA and cytokeratin fragment (CYFRA) provided a test with 89.2% sensitivity and 85.0% specificity [249].

Extending beyond lung cancer, miRNA profiling of pleural effusions in mesothelioma has also shown promising diagnostic potential. For example, miR-21 and miR-126 can assist in distinguishing mesothelioma from reactive mesothelial cells, while miR-130a expression helps differentiate mesothelioma from lung adenocarcinoma, with 77% sensitivity and 67% specificity [250]. Moreover, studies comparing PM with benign asbestos-related pleural effusion (BAPE) identified eleven significantly upregulated miRNAs, including miR-484, miR-320, and let-7a [251].

Notably, a combined panel of miR-143, miR-210, and miR-200c in pleural effusion samples showed excellent diagnostic performance, achieving an AUC_{ROC} of 0.92 for distinguishing PM from non-PM cases [236].

While most studies have focused on miRNAs, other circulating RNA species – such as messenger RNAs (mRNAs), long non-coding RNAs (lncRNAs) and circular RNAs (circRNAs) – are also emerging as promising biomarkers, although their clinical utility in mesothelioma and lung cancer remains less well explored [252] - [255].

Importantly, most studies measuring circulating biomarkers such as different types of RNAs or ctDNA analyze the total pool, which includes both free molecules and those encapsulated in extracellular vesicles; therefore in the next section, I will explore EVs in more detail as distinct and promising carriers of cancer-related biomarkers.

2.4.3.1. Extracellular vesicles diagnostic potential in NSCLC and PM

As previously discussed, EVs are produced by basically all human cell types and carry molecular signatures reflective of their cell of origin. Importantly, EVs can enter body fluids and mediate intercellular communication at distant sites. This capacity not only underscores their functional relevance but also makes them accessible for enrichment, purification, or isolation from body fluids, where they hold considerable promise as prognostic and predictive biomarkers in various diseases.

Despite significant advances in optimization, the isolation of EVs from body fluids remains technically challenging. This difficulty arises primarily from the overlap in size and density between EVs and other abundant circulating components, such as lipoproteins, protein aggregates, and viruses. To address these challenges, a range of **isolation strategies** has been developed, each exploiting distinct physicochemical properties of EVs [256]. Size-based methods include size-exclusion chromatography (SEC), ultrafiltration, tangential flow filtration (TFF), and asymmetric flow field-flow fractionation (AF4). Sedimentation-based approaches rely on differential and ultracentrifugation (dUC), while density-based methods employ density gradient or cushion ultracentrifugation. Additionally, techniques leveraging both size and isoelectric point, such as free-flow electrophoresis (FFE), or those based on charge (various affinity chromatography), have been explored. Importantly, immunoaffinity-based strategies target EV surface markers, most commonly the canonical tetraspanins CD9, CD63, and CD81, or, in case of cancer-derived EVs, tumor-specific markers such as epithelial cell adhesion molecule (EpCAM/CD326). Given that different isolation methods enrich for distinct EV subpopulations and

may co-isolate non-EV contaminants, it is critical that studies reporting EV biomarkers clearly document the isolation strategy used, to ensure reproducibility, transparency, and appropriate interpretation of results [2].

Extracellular vesicles diagnostic potential in NSCLC patients

Several studies have demonstrated the promising role of EVs as diagnostic biomarkers in NSCLC, leveraging their molecular cargo, including DNA, RNA, proteins, and lipids, isolated from patient blood samples.

EV-derived DNA has emerged as a valuable diagnostic tool. For example, co-isolation of EV-associated DNA and RNA together with cell-free DNA (cfDNA) using ExoLution™ Plus extraction technology from plasma to detect EGFR mutations, yielded a diagnostic sensitivity of 98%, compared to 82% when relying on cfDNA alone [257]. Castellanos-Rizaldos et al. [258] similarly applied this combined approach among NSCLC patients and achieved 92% sensitivity and 89% specificity in detecting EGFR T790M mutations (threonine to methionine shift at codon 790, which is responsible for acquired resistance against EGFR therapy). In another study, EV DNA isolated by ultracentrifugation outperformed plasma cfDNA in detecting EGFR mutations [259]. Furthermore, mitochondrial DNA (mtDNA) is also transferred via EVs, and elevated levels of specific mtDNA fragments (e.g., mtDNA79, mtDNA230, MTATP8) were observed in EVs isolated from NSCLC patients' plasma (using the Total Exosome Isolation Reagent kit) compared to healthy controls, correlating with disease invasiveness [260].

EV-associated ***microRNAs*** (miRNAs) are also widely explored as diagnostic markers. Rabinowitz et al. showed that plasma-derived EVs, isolated via SEC and EpCAM-coated beads, contained significantly elevated miRNA levels in lung cancer patients compared to non-cancer controls [261]. Specific miRNA signatures, such as reduced levels of let-7f, miR-20b, and miR-30e-3p (isolated using BerEP4 antibody-coated beads), distinguished NSCLC patients from healthy individuals [262]. Interestingly, although total serum miR-126 levels did not differ between NSCLC patients and controls, EV-associated miRNA-126 (after sucrose cushion isolation) was significantly elevated in stage I-III NSCLC patients [263]. Further studies using ultracentrifugation and EpCAM bead-isolated EVs identified miRNA panels (let-7b-5p, let-7e-5p, miR-23a-3p, miR-486-5p) capable of distinguishing NSCLC from non-NSCLC individuals with 80% sensitivity and 92% specificity, while additional miRNA sets discriminated adenocarcinoma (miR-181-5p, miR-30a-3p, miR-30e-3p, miR-361-5p) from squamous cell carcinoma (miR-10b-5p, miR-15b-5p, miR-320b) [264]. Another EV miRNA profile (7 miRNAs: hsa-miR-451a, hsa-miR-486-5p, hsa-miR-363-

3p, hsa-miR-660-5p, hsa-miR-15b-5p, hsa-miR-25-3p, hsa-miR-16-2-3p), isolated using the exoRNeasy Serum/Plasma RNA kit, effectively distinguished NSCLC patients from healthy volunteers [265]. Notably, some EV miRNAs (e.g., hsa-miR-331-5p, hsa-miR-451a, hsa-miR-363-3p) could even differentiate small cell lung cancer (SCLC) from NSCLC with 100% sensitivity and specificity [265]. Additionally, EV-associated miR-1290 (isolated using Invitrogen™ Total Exosome Isolation Kit) outperformed established diagnostic markers (CEA, CYFRA21-1, NSE) for lung adenocarcinoma, achieving 80% sensitivity and 97% specificity, with levels decreasing post-resection and correlating with tumor stage, size, lymph node involvement, and metastasis [266].

Beyond small RNAs, EV-associated ***long non-coding RNAs*** (lncRNAs) such as RP5-977B1 [267] (isolated by ultracentrifugation) and DLX6-AS1[268] (isolated using ExoQuick Exosome Precipitation) demonstrated superior diagnostic performance compared to conventional markers (CEA, CYFRA21-1) in differentiating NSCLC patients from healthy or pulmonary tuberculosis controls.

EV membrane ***proteins*** are also gaining attention. Yamashita et al. [269] measured soluble EGFR and EV-associated EGFR in plasma (via CD81- and EGFR-based ELISAs), finding that while soluble EGFR levels were comparable between NSCLC and control groups, CD81-positive EV-associated EGFR was elevated in NSCLC [269]. The combined analysis of EV EGFR and CXCR4 expression (ultracentrifuge-isolated EVs) further improved diagnostic accuracy in distinguishing advanced NSCLC from healthy controls [270]. CD91 analysis on EVs using sandwich ELISA (with CD9 as the capture antibody) also outperformed CEA in adenocarcinoma diagnosis, while the combined markers (EV-CD91+CEA) were achieving the highest sensitivity (71%) and specificity (92%) [271]. Moreover, SEC-isolated EVs from early-stage NSCLC patients showed elevated GRIP and coiled-coil domain-containing 2 (GCC2) protein levels compared to healthy individuals, reaching 90% sensitivity and 75% specificity [272].

Lipidomics has started gaining recognition in the EV diagnostic field. Soupir et al. reported significant differences in the lipid profiles of SEC-isolated EVs between NSCLC patients and healthy individuals, highlighting another promising molecular layer for diagnostic exploration [273].

Recent approaches have explored detecting EV-associated mutational or ***molecular signatures*** using advanced technologies. For example, surface-enhanced Raman spectroscopy (SERS) combined with deep-learning algorithms successfully discriminated lung cancer patients carrying EGFR mutations from controls with 93% accuracy [274]. Notably, a SERS-based deep-learning algorithm trained on lung cancer cell-derived EVs successfully identified corresponding

patterns in patient-derived EVs (ultracentrifuge-isolated) and differentiated lung cancer patients from healthy controls [275], [276]. SERS applied to SEC-isolated plasma EVs, combined with AI analysis, achieved 83% sensitivity and 92% specificity in diagnosing lung cancer and could further distinguish between lung, breast, colorectal, liver, pancreatic, and stomach cancers [277]. In another study, immunocapture-isolated EVs (targeting PTX3 and THBS1), when labeled with SERS nanotags and analyzed via AI, reached 92% sensitivity and 100% specificity in differentiating early-stage lung cancer from benign lung diseases [278].

Notably, several clinical trials are investigating different biomarkers on plasma-derived extracellular vesicles [279].

While plasma remains the most widely investigated source for EV-based diagnostics, **pleural effusion** fluid represents a less frequently explored but highly promising material, particularly in thoracic malignancies such as NSCLC. Lee et al. [280] have demonstrated that EV-derived ***DNA*** isolated from pleural effusion can outperform both cell-free DNA (cfDNA) and conventional cytology for the detection of EGFR mutations and resistance-associated alterations, such as the T790M mutation [280].

Among ***miRNAs*** the miR-200 family has shown strong diagnostic potential in distinguishing NSCLC patients from those with benign inflammatory conditions when analyzing pleural effusion-derived EVs (isolated using the ExoRNeasy Serum/Plasma Kit). Interestingly, in the same study, the ***mRNA*** transcript encoding Lipocalin-2 (LCN2) displayed even greater diagnostic performance [281]. Comparative analyses of EV-derived miRNAs (isolated by differential centrifugation) from pleural effusion samples of patients with lung adenocarcinoma, tuberculosis, and other benign lesions revealed that nine miRNAs (miR-205-5p, miR-483-5p, miR-375, miR-200c-3p, miR-429, miR-200b-3p, miR-200a-3p, miR-203a-3p, and miR-141-3p) were preferentially enriched in the adenocarcinoma group [282]. Furthermore, Tamiya et al. demonstrated that miR-182 and miR-210 levels were significantly elevated in adenocarcinoma patients' pleural effusion-derived EVs, than in EVs from benign pleural effusions (isolated using the Total Exosome Isolation Reagent), with receiver operating characteristic (ROC) values of 0,87 and 0,81, respectively, supporting their strong diagnostic utility [283].

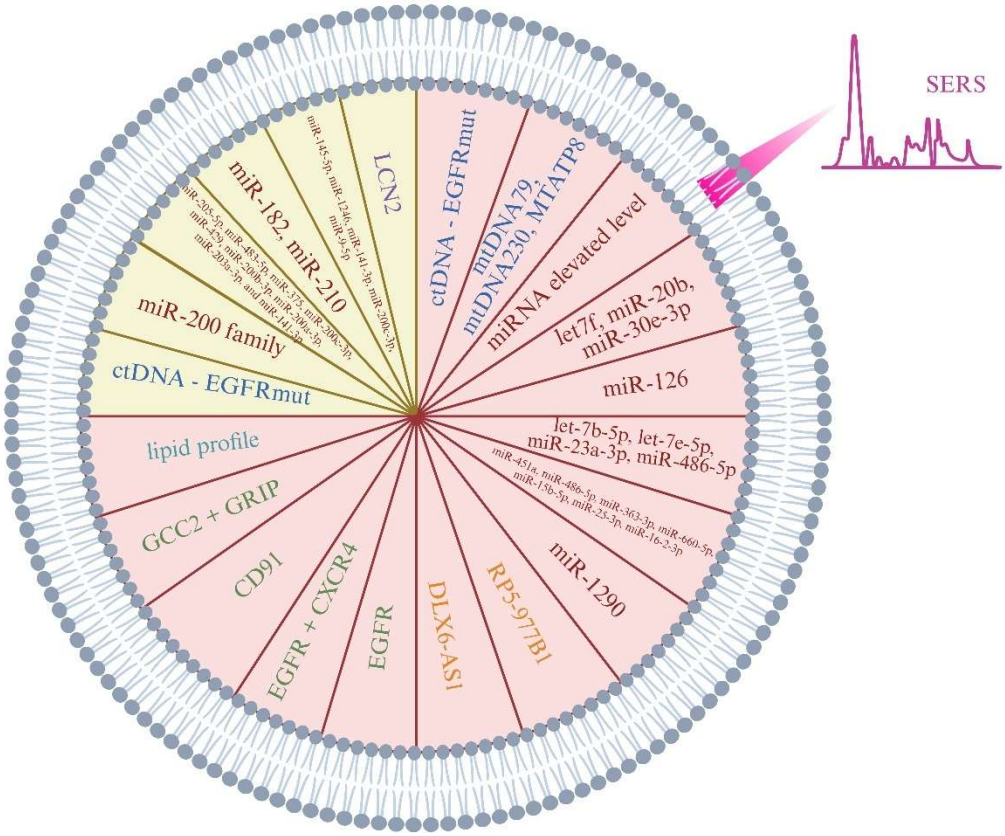

Figure 2.4. Overview of potential EV-associated biomarkers for NSCLC diagnosis. *Only markers that significantly differentiated NSCLC patients from controls are displayed. The source of EVs is indicated by background color: light red for blood-derived and light yellow for pleural effusion-derived vesicles. Marker types are color-coded: DNA (blue), miRNAs (red), lncRNAs (orange), proteins (green), and mRNAs (purple). Distinct molecular signatures of the isolates were characterized by surface-enhanced Raman spectroscopy (SERS) through pattern analyses, the method highlighted in pink. Figure created with Biorender.com.*

Extracellular vesicles diagnostic potential in PM patients

Although the diagnostic potential of EVs has been widely explored in numerous cancers, PM remains relatively understudied. Below, I summarize key findings from the existing literature on EV-based biomarkers in PM.

To begin with **blood-derived EVs**, Casalone et al. performed whole miRNome screening on serum EVs (isolated using ExoQuick precipitation) from a multicenter cohort of preclinic PM patients. They identified a ***miRNA*** signature – miR-11400, miR-148a-3p, and miR-409-3p – that was upregulated up to five years before diagnosis compared to matched controls, achieving 75% specificity and 70% sensitivity [284]. Another study evaluated plasma-derived EVs to differentiate between PM and asbestos-exposed non-PM individuals. Screening 754 miRNAs in EVs isolated by ultracentrifugation, they found that the combination of miR-103a-3p and miR-30e-3p yielded the highest diagnostic performance, with 96% sensitivity and 80% specificity for PM detection [285].

Ferrari et al. [286] further examined a similar cohort of PM patients and asbestos-exposed controls, focusing specifically on the plasma concentrations of hsa-miR-30e-3p and hsa-miR-103a-3p in EVs (isolated by ultracentrifugation). Both miRNAs were significantly decreased in PM patients, and their combined assessment reached 81% sensitivity and 78% specificity in distinguishing PM from asbestos-exposed individuals.

Beyond RNA cargo, the ***protein*** composition of plasma-derived EVs has also been investigated in PM. Hoshino et al. [287] analyzed EV protein signatures across plasma samples from patients with 16 different cancer types, including mesothelioma. Using a random forest algorithm, they identified 47 EV-associated proteins with the highest predictive value for distinguishing tumor from non-tumor plasma samples. These proteins achieved 95% sensitivity and 90% specificity, while using the full set of 372 identified EV proteins increased sensitivity to 100%. Heatmap visualizations in their study clearly showed that the 47-marker signature produced distinct expression patterns in mesothelioma compared to healthy controls and other cancer types.

Notably, pleural fluid-derived EVs have not been systematically investigated in cohorts restricted to PM versus control subjects. To date, the available studies on pleural fluid-derived EVs have included both PM and lung cancer patient groups. As my dissertation project focuses on a cohort comprising PM, NSCLC, and pleuritis patients, I will address these two relevant studies in a separate section.

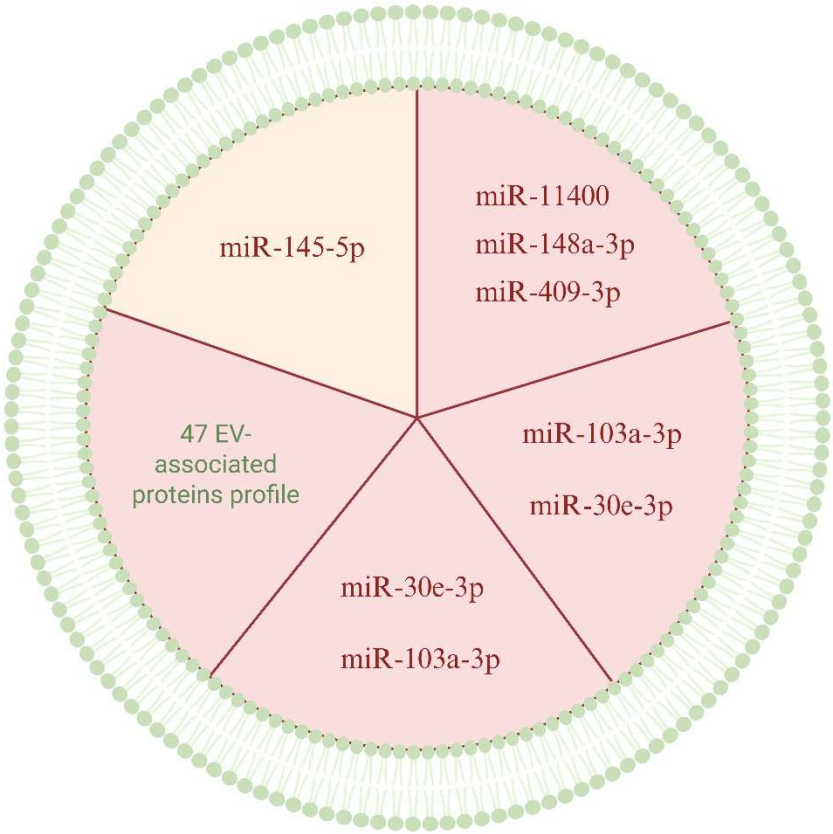

Figure 2.5. Overview of potential EV-associated biomarkers for PM diagnosis. *Only markers that significantly differentiated PM patients from controls are displayed. The source of EVs is indicated by background color: light red for blood-derived and light yellow for pleural effusion-derived vesicles. Marker types are color-coded: miRNAs (red), proteins (green). Figure created with Biorender.com.*

Extracellular vesicles potential to distinguish between NSCLC, PM and benign pleural-effusions

A recent study examined EV-miRNA profiles across PM (n = 11), lung adenocarcinoma (n = 11), and benign pleural effusion (n = 9) samples. EVs were isolated using ultracentrifugation, and miRNA expression was assessed with the Nanostring nCounter® Human v3 miRNA assay. The most significant miRNA distinguishing malignant from benign effusions was hsa-miR-145-5p, which also emerged as the only miRNA significantly differentiating PM from benign effusions. Furthermore, five miRNAs (hsa-miR-145-5p, hsa-miR-1246, hsa-miR-141-3p, hsa-miR-200c-3p, hsa-miR-9-5p) significantly distinguished benign from lung cancer patients, while three miRNAs (hsa-miR-1246, hsa-miR-141-3p, hsa-miR-200c-3p) were more highly expressed in lung cancer patients than in PM. In contrast, hsa-miR-136-5p was elevated in PM compared to lung cancer [288].

Javadi et al. [289] investigated a similar cohort comprising PM (n = 9), lung adenocarcinoma (n = 12), and benign (n = 6) pleural effusion samples. Pleural fluid EVs were fractionated by sequential

centrifugation: 2,000 × g for apoptotic bodies, 10,000 × g for microvesicles, and 100,000 × g for exosomes, with additional analysis of proteins dissolved in the supernatant. Surface marker expression of the isolates was analyzed using a multiplex bead-based assay (MACSPlex Exosome Kit). The highest median fluorescence intensity values were consistently observed in the exosome fractions across all patient groups. While the article did not report detailed statistical comparisons of surface marker profiles between groups, general trends were described. Compared to PM, exosomes from adenocarcinoma patients exhibited elevated expression of markers such as CD9, CD63, CD81, CD2, CD8, CD14, CD29, CD44, CD49e, CD62p, CD105, CD146, CD326, HLA-ABC, and MCSP, while HLA-DRDPDQ and ROR1 were lower. Adenocarcinoma-derived exosomes also expressed higher levels of these markers (except CD2 and CD8) relative to benign effusions. Notably, markers elevated in PM compared to controls included CD326, HLA-ABC, and HLA-DRDQ [289].

Together, these findings highlight both the promise and the current limitations of EV-based biomarkers in thoracic malignancies, underscoring the need for further research to refine diagnostic strategies and improve clinical utility. The following chapter outlines the specific aims and objectives that this dissertation addresses to contribute to this field.

3. Objectives

The overarching aim of this dissertation is to investigate the role of EVs in cancer progression, with particular emphasis on their involvement in cell migration, resistance to targeted therapies, and their potential application in liquid biopsy-based diagnostics. The specific objectives of the research are as follows:

- **To assess the role of EVs in tumor progression,** including their impact on primary tumor growth and metastatic potential, through proliferation assays, sphere formation assays, and migration analyses. For these experiments, cell lines representing varying stages of tumor progression but sharing similar genetic backgrounds to be employed.
- **To elucidate the contribution of EVs to resistance against BRAF and MEK inhibitors,** primarily through single-cell migration analyses using EVs derived from cells with distinct drug sensitivities:
    - Investigate the role of EVs in resistance to vemurafenib, the first-generation BRAF inhibitor used in the treatment of patients from whom some of the cell lines were derived.
    - Evaluate EV-mediated support of dual resistance to dabrafenib (BRAFi) and trametinib (MEKi) in cell lines that had been previously exposed to BRAF inhibition.
    - Establish melanoma cell line clones resistant to long-term combined encorafenib (BRAFi) and binimetinib (MEKi) exposure, characterize the resulting phenotypic alterations, and assess the potential of EVs from these clones to promote dual therapy resistance, also in the context of EV preconditioning.
- **To investigate the diagnostic utility of EVs in thoracic malignancies,** by analyzing surface marker expression profiles of EVs isolated from pleural effusion samples of patients with NSCLC, PM, and benign pleuritis using a multiplex bead-based assay:
    - Assess the diagnostic relevance of individual surface markers in distinguishing between disease groups.
    - Explore the potential of machine learning algorithms to improve patient classification based on EV surface marker signatures.
    - Evaluate alternative patient classification strategies by comparing diagnostic performance when (i) all patients are included based on clinical cancer history and (ii) patients with unclear or confounding clinical backgrounds are excluded. To help determine whether stricter patient selection improves the accuracy of EV-based diagnostic classification.

4. Methods

4.1. Cell lines and culturing

Melanoma cells used for the experiments were pairwise originating from the same patient (i.e. representing the same genetic background) and modelling the less and more advanced stages of the given tumor.

The Mel Pt-1, Mel Pt-3, and Mel Pt-4 cell line pairs were established and kindly provided by Professor Peter Hersey (Oncology and Immunology Unit, Calvary Mater Newcastle Hospital and the Kolling Institute, Royal North Shore Hospital, University of Sydney, NSW, Australia) [290]. Within each pair, the "pre" cell line was derived prior to vemurafenib treatment, while the "post" counterpart was isolated during treatment. All patients showed partial response to vemurafenib, and all cell lines harbor the BRAF V600E mutation [290].

Additional BRAF V600E mutant cell lines used included WM983A (derived from a primary tumor) and WM983B (derived from a corresponding metastasis), both available from the Wistar Institute (Philadelphia, PA, USA), as well as A2058 from ATCC. The M1 cell line, a highly tumorigenic subclone of A2058, was selected based on its tumor-forming capacity in immunosuppressed mice [291].

Unless otherwise specified, all cells were cultured in high-glucose DMEM (4.5 g/L glucose, with L-glutamine and sodium pyruvate; Capricorn-Scientific) supplemented with 10% fetal bovine serum (FBS, EuroClone) and 1% penicillin-streptomycin-amphotericin (PSA, Lonza), maintained at 37 °C in a humidified atmosphere with 5% CO_2.

4.1.1. Generating drug resistant cell line clones

The Mel Pt-3 pre and Mel Pt-4 post cell lines were exposed to low concentrations of the combination of the BRAF inhibitor (BRAFi) encorafenib (enco) and the MEK inhibitor (MEKi) binimetinib (bini) until they developed resistance to the enco-bini treatment. Cells were cultured under standard conditions in DMEM supplemented with 10% FBS and 1% PSA. Initial drug concentrations of 1 nM for both inhibitors were applied, irrespective of the baseline sensitivity of each cell line. The concentrations of enco-bini were gradually increased once the cells reached confluence at a similar rate to the original cell lines. Sensitivity to the enco-bini treatment was regularly monitored using the SRB cell viability assay (described below).

Unfortunately, the Mel Pt-3 pre cell line showed a significant decrease in proliferation when exposed to higher concentrations of enco-bini, eventually reaching a point where its growth slowed to a critical level. As a result, the process of inducing resistance in this cell line was halted. In contrast, resistance was successfully established in Mel Pt-4 post cells after approximately 8

months of treatment. The final applied enco-bini concentration was 205-205 nM. Multiple vials of these resistant clones were then cryopreserved at -80°C for future use.
Prior to each experiment, resistant clones were cultured in standard medium for a maximum of 14 days, and a new vial was thawed for each experimental setup.

4.2. Production and isolation of cell culture supernatant-derived extracellular vesicles (EVs)

Before harvesting the supernatant, cells were cultured in three 75 cm^2 tissue culture flasks in standard medium. For the original cell lines (Mel Pt-1, Mel Pt-3, Mel Pt-4 pre and post, WM983A, WM983B, A2058, M1), cultures were grown to 50-60% confluence, while for the resistant clones, they were cultured to 80-90% confluence. Subsequently, cells were washed twice with Phosphate Buffered Saline (PBS, Capricorn-Scientific) and then cultured in DMEM supplemented with 1% EV-depleted FBS (Biowest) for three days to achieve the best possible EV production.
The collected supernatants were first centrifuged at 500 g for 5 minutes to remove floating cells and cell debris. These supernatants were then stored at -80°C for later use. On the day of the isolation, the frozen supernatants were slowly thawed, centrifuged at 3,000 g for 15 minutes at 4 °C, and filtered through a 0.2 µm syringe filter unit (Sarstedt) to remove larger particles. Following this, the filtered samples were subjected to ultracentrifugation (Beckman L7-55 Ultracentrifuge, TYPE 50.2 Ti rotor) at 100,000 g for 1.5 hours at 4°C. The resulting pellets (containing EVs) were resuspended in 300 µl of PBS and used immediately for functional assays or stored at -80°C for later characterization.

4.3. Characterization of cell culture-derived EVs

EV samples were first verified using Dynamic Light Scattering (DLS). The isolation was considered successful if the EV sample's main particle population size was in the range of cell-culture supernatant EVs [2] and the EV depleted supernatant didn't contain particles larger than 10 nm.

4.3.1. Qubit protein assay

Protein concentration in EV isolates was measured using the Qubit® Protein Assay Kit (Thermo Fisher Scientific) following the manufacturer's protocol. Briefly, the Qubit reagent was diluted 1:200 in Qubit buffer to prepare the working solution. Then, 10 µl of each standard solution was added to 190 µl of working solution. After instrument calibration, 5 µl of each sample was mixed with 195 µl of working solution and inserted into the fluorometer for measurement.

4.3.2. Sulfophosphovanillin (SPV) lipid assay

The SPV assay was performed according to Visnovitz et al [292]. Initially, each EV isolates were measured in duplicates and diluted 1:1 with PBS, resulting in a final volume of 40 µl per sample. A serial dilution of the 1 mg/ml 1,2-dioleoyl-sn-glycero-3-phosphocholine (DOPC) stock solution was then prepared to generate standard concentrations of 16, 8, 4, 2, 1, 0.5, and 0.25 µg, along with a blank sample (0 µg) containing only PBS for background correction. To each 40 µl sample or standard, 400 µl of 96% sulfuric acid was added, followed by thorough vortexing to ensure homogenization. The mixtures were incubated with open lids at 90 °C for 20 minutes in an extraction cabinet. Following incubation, the samples were placed at 4 °C for 5 minutes with lids closed to cool down. Once cooled, 120 µl of phospho-vanillin reagent was added to each sample, and the mixtures were vortexed again. Subsequently, 180 µl of each solution was transferred to a 96-well plate and incubated at 37 °C for 1 hour. Absorbance was measured at 570 nm using a spectrophotometer, and the lipid content of the EV isolates was quantified based on the corresponding DOPC standard curve.

4.3.3. Particle size and concentration measurements with Nanoparticle Tracking Analyses (NTA)

Particle concentration and size distribution of the extracellular vesicle isolates were analyzed using the ZetaView® PMX120 instrument (Particle Metrix). Calibration was performed with 100 nm polystyrene beads to ensure measurement accuracy. Samples were diluted in 0.22 µm-filtered PBS at ratios ranging from 1:500 to 1:1000, depending on particle density, to maintain optimal detection conditions. Each measurement was carried out across 11 distinct positions with 3 cycles per position. Detection parameters were set to a minimum particle area of 5, a maximum area of 1000, and a minimum brightness threshold of 20. Particle concentration was automatically calculated by the ZetaView® software (version 8.05.12 SP1) following frame-by-frame analysis, with outlier positions excluded from the final dataset.

4.3.4. Surface markers expression analyses with latex bead-based flow cytometry

Extracellular vesicles were analyzed by flow cytometry using a CytoFlex flow cytometer (Beckman Coulter Inc.) based on the detection of common surface markers. To enable detection, EVs were initially attached to 3 µm aldehyde/sulfate latex beads (4% w/v; Thermo Fisher Scientific). The EV samples were incubated with a 1:1000 dilution of beads (prepared in PBS) at a 1:1 volume ratio for 30 minutes at room temperature (RT) with gentle agitation (320 rpm). The bead-to-EV ratio was optimized to ensure at least 300 vesicles per bead. Following incubation, the mixture was blocked

using glycine (100 mM final concentration) and bovine serum albumin (BSA, 0.5% final concentration) for 1 hour at RT with continuous shaking. Excess blocking reagents were removed by centrifugation at 3,000 g for 5 minutes, and the pellets were resuspended in PBS at five times the original sample volume.

For surface marker staining, the bead-bound EVs were labeled with Annexin V-FITC (1:1000; Invitrogen™), and the following primary antibodies: EpCAM (1:100; GeneTex GTX34694), CD81 (1:100; GeneTex GTX75436), CD63 (1:100; GeneTex GTX28219), and CD9 (1:100; GeneTex GTX22215). Alexa Fluor™ 488-conjugated goat anti-mouse IgG (1:200; Invitrogen A11029) was used as the secondary antibody. Staining was carried out at 37°C for 30 minutes with shaking (320 rpm). Negative control beads, blocked with glycine and BSA, were incubated only with Annexin V-FITC and the secondary antibody. All samples were analyzed directly on the CytoFlex flow cytometer, and gating of the 3 µm bead population was performed using the CytExpert software.

4.4. Treatment schemes and cell viability (SRB) assay

To explore the impact of vemurafenib (PLX4032 VWR), dabrafenib (VWR), trametinib (VWR), encorafenib (Anthelos), binimetinib (Anthelos), the combination of dabrafenib-trametinib and encorafenib-binimetinib and EVs on two-dimensional (2D) cell viability Sulforhodamine B (SRB) assay was performed.

Firstly, cells were cultured in the inner 60 wells of a 96-well plate and subsequently treated the next day with serial dilutions of the BRAF, MEK, the combination of BRAF-MEK inhibitors and EVs (10 µg/ml protein concentration) in DMEM supplemented with 10% EV-depleted FBS for 72 hours. In cases where EV treatment was combined with enco-bini, certain wells received EV treatment alone initially, and the media was changed to enco-bini-containing media after 24 hours. While in all cases cell were fixed after 72 hours of the first treatment, this step was performed using 10% trichloroacetic acid (TCA), then the plates were stained with SRB dye after washing and drying the wells. After 15 minutes the stain was recollected for further use, and the cells were washed with 1% acetic acid solution and dried out. The stain was dissolved in 10 mM Tris-HCl, pH 8 and absorbance was determined close to the stain absorbance maximum, at 570 nm. data were averaged from independent experiments, and treatment effects were represented as the ratio of treated to control conditions. The interactions between the BRAF and MEK inhibitors were analysed by Compusyn software (ComboSyn Inc), calculating the combination index (CI). $CI < 1$, $CI = 1$, $CI > 1$ represents synergism, additive effects and antagonism, respectively [293].

4.5. Spheroid formation assay

The 3D spheroid cultures were established by seeding cells into U-bottom 96-well plates, which had been coated with 30 µl of a 25 mg/ml poly(2-hydroxyethyl methacrylate) (poly-HEMA, Merck) solution prepared in 96% ethanol. Plates were placed on a rocking platform and left to dry completely over three days. Cells were seeded at a density of 1,000 cells per well in DMEM supplemented with 10% EV-depleted FBS and 0.04 mg/ml collagen (Merck). To promote spheroid formation, plates were centrifuged at 2,200 RPM for 10 minutes. After 24 hours of incubation, EVs were added at a final protein concentration of 10 µg/ml. Spheroid development was tracked over a 7-day period by capturing daily grayscale images. Quantification was performed using ImageJ, with spheroid size expressed as signal intensity (SI), incorporating spheroid area, integrated density (ID), and the well's median pixel value. The formula used was:

$$SI = 255 \times area - ID - (255 - median) \times area.$$

4.6. Video microscopy measurements

For 2D live-cell imaging, 1,000 cells were seeded into the inner 60 wells of a 96-well plate to promote multidirectional migration and maintain low confluency throughout the experiment. The applied drug concentrations were selected based on results from initial SRB viability assays, ensuring the use of doses that produced a detectable biological effect while avoiding concentrations that caused extensive loss of cell viability. Vemurafenib was applied at the following concentrations: Mel Pt-1 and Mel Pt-4 pre and post at 10 µM, Mel Pt-3 pre at 0.75 µM and post at 7.5 µM, WM983A at 0.05 µM, WM983B at 0.25 µM, and A2058 and M1 at 2.5 µM. In addition, dabrafenib and trametinib were used for Mel Pt-3 pre: 20 nM and 2 nM, respectively, and 50 nM and 5 nM, respectively, for the Mel Pt-3 post cells. Encorafenib and binimetinib were applied at the final concentrations used during the generation of resistant clones (205-205 nM). EVs were administered in volumes corresponding to 10 µg/ml protein concentration, calculated individually for each isolate based on measured protein content.

After treatment, plates were placed into an inverted phase contrast microscope with an automatic stage and surrounding incubator (Nikon TIE microscope, Prior stage, Oko-Lab incubator) and kept at 37 °C in 5% CO_2 atmosphere. Time-lapse images were acquired at 10-minute intervals for 24 hours. In cases where EV treatment was combined with encorafenib-binimetinib (enco-bini), certain wells received EV treatment alone initially, followed by the addition of enco-bini after 24 hours, at which point a second round of 24-hour video recording was initiated. Then the video recordings were preprocessed in ImageJ. First, a Gaussian Blur filter with a sigma value of 1.4 was applied to the initial frame of each recording to reduce noise. Background

correction was then performed using the rolling ball algorithm with a 12-pixel radius. Afterwards, the images were inverted, and contrast was enhanced by adjusting the saturation to 0.06. Pixel values were converted to µm, using a scale where 1 pixel equals 2.18 µm.

The preprocessed images were used for cell migration analyses, measuring cell size, shape and cell proliferation. To evaluate the cells migratory capacity semi-automated single-cell tracking were carried out using the CellTracker software [294], which provided XY coordinates of individual cells. Two parameters were derived from the tracking data: total travelled distance (TTD), calculated by summing the stepwise distances between consecutive frames, and mean square displacement (MSD), which measures the average square displacement over increasing time intervals between two points. The calculation of the two parameters were performed in MATLAB.

$$MSD_i = \left(\frac{1}{N-i}\right)\sum_{k=1}^{N-i} d^2(p_k, p_{k+i}) \qquad TTD_i = \sum_{k=1}^{i-1} d(p_k, p_{k+1})$$

In the equations, *d* is the distance between two points, *p* represents the positional vector ($p_i = (x_i, y_i)$), and i ranges from 1 to *N-1*, with *N* being the total number of frames.

To quantify treatment effects, MSD and TTD values were first averaged across untreated control cells as a function of time. Then, for each individual cell and the averaged control, the area under the curve (AUC) was calculated using MATLAB's trapz() function. In certain cases, ΔAUC values were obtained by subtracting the control AUC from each cell's individual AUC, and the average ΔAUC was reported for the treatment condition.

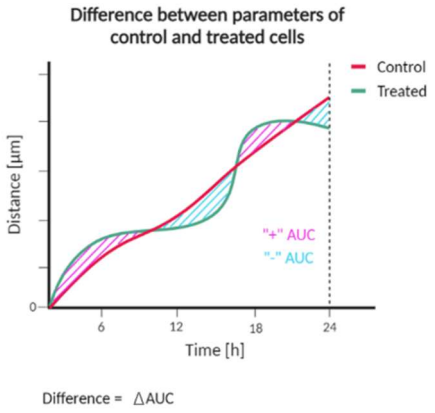

Figure 4.1. Visualization of the calculation of ΔAUC values from the time dependent MSD and TTD curves. *The area under the curve (AUC) was calculated using MATLAB's trapz() function, and the ΔAUC values were calculated by subtracting the average control AUC from each cell's individual AUC.*

Cell area and morphology were manually assessed using ImageJ. To compare the various generated cell clones, a minimum of 10 cells per well were analyzed at both 0 and 24 hours.

Cell proliferation was manually evaluated in ImageJ by counting the number of cells at both the initial time point (0 h) and after 24 hours. Relative proliferation was determined by dividing the cell count at 24 hours by the initial cell number.

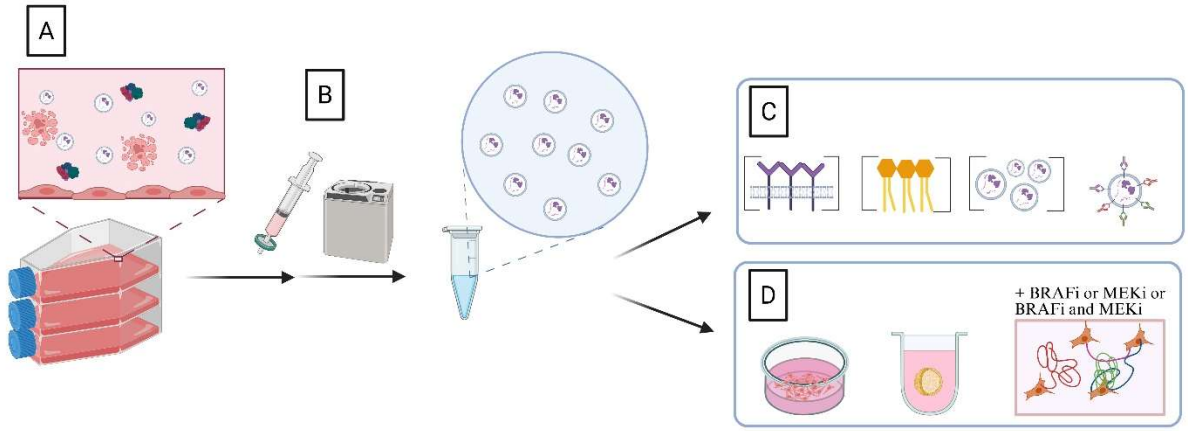

Figure 4.2. Visualization of the in vitro experiments. *A) EVs were produced over a 72-hour period, with cell culture supernatants collected thereafter; in specific experiments, drug-resistant cell line clones were established prior to EV production; B) EV isolation via sequential filtration and ultracentrifugation; C) Characterization of EV isolates, including protein quantification (Qubit protein assay), lipid content assessment (sulfo-phospho-vanillin [SPV] assay), particle size and concentration analysis (nanoparticle tracking analysis [NTA]), and bead-based surface marker profiling (EpCAM, CD81, CD63, CD9, Annexin); D) Functional assays were performed following EV treatment, including proliferation (SRB assay), 3D sphere formation, and single-cell migration tracking. Migration assays were carried out with EVs alone or in combination with BRAF inhibitor (BRAFi), MEK inhibitor (MEKi), or dual BRAFi-MEKi treatment. Figure created with Biorender.com.*

4.7. Patient cohort and classification

This study included pleural effusion samples from 82 patients which was collected at the Department of Thoracic Surgery, West German Cancer Center, University Medical Center Essen-Ruhrlandklinik, University Duisburg-Essen. The cohort consisted of 29 individuals with non-small cell lung cancer (NSCLC) (35%), 28 with pleural mesothelioma (PM, 34%), and 25 with pleuritis (30%). Among NSCLC patients, 22 had adenocarcinoma (76%) and 7 had squamous cell carcinoma (24%). The PM subgroup was composed of 19 epithelioid, 6 biphasic, and 3 sarcomatoid cases. All together 57 patients were having malignant pleural involvement. This group is composed of all patients diagnosed with NSCLC, PM, and a patient with pleuritis who also had evidence of tumor affecting the pleura. A review of clinical records revealed that some patients had a prior history of malignancies differing from those diagnosed at the time of effusion collection. Moreover, incomplete medical data in certain cases necessitated their exclusion from further analyses. Based on this, five distinct classification schemes were established.

1. “Initial”:
    a) NSCLC: Patients have NSCLC based on the current symptoms and pathologist's diagnosis at the time of sample collection (29 patients).
    b) PM: Patients have PM based on the current symptoms and pathologist's diagnosis at the time of sample collection, classified without knowledge of broader clinical history (28 patients).
    c) Pleuritis: Patients have benign pleuritis based on the current symptoms and pathologist's diagnosis at the time of sample collection, classified without knowledge of broader clinical history (25 patients).

2. “Tumor focused”:
    1. Cancer: Patients with cancer, regardless of whether they also have PM or pleuritis at the same time (46 patients).
    2. PM: Exclusive PM cases (24 patients).
    3. Pleuritis: Those with pleuritis without additional cancer or PM (10 patients).

3. “Pleura involvement”:
    a) Cancer in pleura: Patients whose cancer infiltrated the pleura (26 patients).
    b) PM: Exclusive PM cases (24 patients).
    c) Cancer not in pleura: Patients whose cancer not infiltrated the pleura (19 patients).
    d) Pleuritis: Patients with exclusively benign pleuritis (10 patients).

4. “Tumor type”:
    a) NSCLC: Patients with NSCLC and without any other type of cancer (27 patients).
    b) PM: Exclusive PM cases (24 patients).
    c) Other cancer: Patients harboring any other type of cancer then NSCLC (17 patients).
    d) Pleuritis: Cases exclusively with benign pleuritis (10 patients).

5. “Strict Criteria”:
    a) NSCLC in pleura: Those patients whose NSCLC infiltrated the pleura (23 patients).
    b) PM: Exclusive PM cases (24 patients).
    c) Pleuritis: Cases exclusively with benign pleuritis (10 patients).

4.8. Extracellular vesicles isolation from pleural fluids

Pleural fluid samples were thawed at room temperature, and EVs were isolated from 1 mL of each sample. Size exclusion chromatography (SEC) was carried out using a custom CL-2B column,

created by packing 4 mL of Sepharose CL-2B (Cytiva, Sweden) into a 5 mL three-piece Luer-lock syringe (Chirana) equipped with a filter ring at the base to retain the resin. Prior to sample application, the column was equilibrated with PBS. Following the addition of 500 µL of the sample, the flow-through was allowed to pass through the resin. An initial 750 µL of PBS was then added and discarded. Subsequently, 1 mL of PBS was applied, and the EV-rich fraction was collected for downstream processing.

The collected 2 mL EV-containing fraction was concentrated using 100 kDa molecular weight cut-off centrifugal filter units (Sigma-Aldrich), spun at 14,000 g for 15-20 minutes at 4 °C until the volume was reduced to approximately 100 µL. The concentrate was recovered by inverting the filter into a clean microcentrifuge tube and spinning at 1000 g for 2 minutes at 4 °C. Isolated EVs were stored at –80 °C until further use.

4.9. Extracellular vesicles isolation from breast cancer patients' plasma

I included data from a pilot study (containing 12 plasma samples from either HER2+ or TNBC breast cancer patients) investigated during my internship to compare the marker composition of pleural effusion and plasma-derived EVs. The experimental procedures were identical to those used for pleural effusion samples, with the sole exception being the type of SEC columns employed for EV isolation. Briefly, SEC was carried out using qEV1 70 nm columns (IZON Science) in conjunction with the Automatic Fraction Collector (AFC, IZON Science), following the manufacturer's protocol. Plasma samples (1 mL) were centrifuged at 3000g for 10 minutes at 4 °C. The resulting supernatant was loaded onto pre-equilibrated qEV1 columns. EV-containing fractions were collected using the default AFC program, which isolates a 2,8 mL EV-enriched fraction following a void volume of 4,7 mL, as specified by the manufacturer. The collected EV fractions were subsequently concentrated by ultrafiltration using Amicon Ultra-4 centrifugal filter units with a 100 kDa molecular weight cutoff (Millipore). Concentration was performed by centrifugation at 3200g at 4 °C until a final volume of 100 µL was achieved. The concentrated EV samples were stored at –80 °C until further analysis.

4.10. Body fluids-derived EVs characterization

Protein concentration was determined using the Qubit Protein Assay, employing the same protocol as described for cell culture-derived EVs (see Section 4.3.1). Nanoparticle Tracking Analysis was used to assess particle size distribution and concentration, following a methodology analogous to that applied for EVs isolated from cultured cells. The only variation involved the

dilution factor: pleural fluid-derived EVs were diluted at 1:10,000 or 1:100,000, depending on particle abundance (See Section 4.3.3).

4.10.1. Nano-flow cytometry (nFCM) for single particle characterization

To confirm the presence of extracellular vesicles, the surface expression of tetraspanins CD9, CD63, and CD81 on single EVs was analyzed via nano-flow cytometry using the Flow NanoAnalyzer (NanoFCM Inc.), following the manufacturer's protocols. The measurement was conducted on 1 isolate per patient group. Instrument calibration was performed with polystyrene fluorescence reference beads (250 nm Std FL SiNPs), while silica nanospheres (S16M-Exo, 68-155 nm; NanoFCM Inc.) were utilized to construct a standard curve for EV size determination. During acquisition, the sampling pressure was maintained at 1.0 kPa, and event rates were kept within the optimal range of 2,000-12,000 events per minute, with data collected over a one-minute interval.

Prior to immunostaining, EV concentrations were estimated by diluting the samples in TE buffer (Tris-EDTA, pH 7.4, Fisher BioReagents) to achieve the desired detection range, followed by a preliminary acquisition. Based on these measurements, EV samples were pre-diluted in PBS before antibody staining so that a 1:500 dilution after the staining procedure resulted in 6000-12000 particles per minute.

For surface marker labeling, fluorescently conjugated antibodies targeting CD9 (APC, clone M-L13), CD63 (AF647, clone H5C6), and CD81 (APC, clone JS-81) were used at final dilutions of 1:30, 1:100, and 1:30, respectively. An APC-conjugated isotype control (clone MOPC-21, 1:30 dilution) was included, along with antibody-only and buffer-only controls. Pre-diluted EVs were incubated with the antibody solutions in a total volume of 5 µL, protected from light, for 40 minutes. Following incubation, samples were diluted tenfold with PBS, and immediately before acquisition, further diluted in TE buffer to a final 1:500 dilution.

Data acquisition and analysis were conducted using NanoFCM Professional software, applying the auto-threshold and EXO-specific settings recommended by the manufacturer.

4.10.2. Bead-based multiplex EV surface marker analyses with MACSPlex kit

Surface marker expression of the isolated EVs was analyzed using the MACSPlex EV kit IO, human (Miltenyi Biotech) following the manufacturer’s overnight protocol with filter plates. The kit enables the simultaneous detection of 37 surface markers (CD1c, CD2, CD3, CD4, CD8, CD9, CD11c, CD14, CD19, CD20, CD24, CD25, CD29, CD31, CD40, CD41b, CD42a, CD44, CD45,

CD49e, CD56, CD62p, CD63, CD69, CD81, CD86, CD105, CD133/1, CD142, CD146, CD209, CD326, HLA-ABC, HLA-DRDPDQ, ROR-1, SSEA-4 and MCSP) along with two isotype controls (mIgG1control and REAcontrol).

Filters were pre-wetted with MacsPlex buffer and centrifuged at 300g for 3 minutes at room temperature. Subsequently, 5×10^9 EVs (quantified by NTA) were diluted in the buffer to a final volume of 120 µl and pipetted into the wells. Each sample was analyzed in triplicate, with three blank PBS included in parallel. Next, 15 µl of MacsPlex Capture Beads was added to each well, and the plate was incubated overnight on an orbital shaker in the dark at room temperature. Following incubation, the beads were washed twice with the buffer and after each wash the plate was centrifuged at 300g for 3 minutes at room temperature. Then, 15 µl of the detection cocktail (5 µl each of CD9, CD63, and CD81) was added to each well. Samples were incubated with antibodies for 1 hour on an orbital shaker in the dark at room temperature. Finally, the membranes were washed twice with the buffer, and after the final wash, beads were resuspended in 150 µl of buffer and transferred to flow cytometry tubes. Samples were acquired using a BD FACSVerse™ Flow Cytometer with BD FACSuite™ software (BD Biosciences). Fluorescence intensities for FITC, PE and APC were recorded, with 10,000 beads analyzed per sample. Bead populations were gated based on their fluorescence properties in the PE and FITC channels using FlowJo Software™ version 10.9 (Tree Star Inc.) and median APC signals were exported and further analyzed in Excel. The mean APC signals of PBS blanks were subtracted from each marker APC intensity, to account for inter-sample variability, marker intensities within each patient's sample were normalized to the corresponding mean intensity of CD9, CD63, and CD81. Mean values of the triplicates were calculated, and values below zero were excluded from further analysis.

4.11. Applied machine-learning algorithm

Leave-One-Out Cross-Validation (LOOCV) was employed to evaluate the performance of the model on this dataset. LOOCV is a robust validation technique wherein, for a dataset comprising n samples, the model is iteratively trained n times – each iteration utilizing n–1 samples for training and the remaining single sample for testing. This approach ensures that every data point is used exactly once as a test set, thereby offering a thorough evaluation of the model's generalizability. LOOCV is especially suitable for small datasets, as it optimizes data usage without requiring a separate validation cohort. The implementation of this validation strategy was based on the algorithm developed by Ádám Rák. A detailed description of the method is provided in the Supplementary Information.

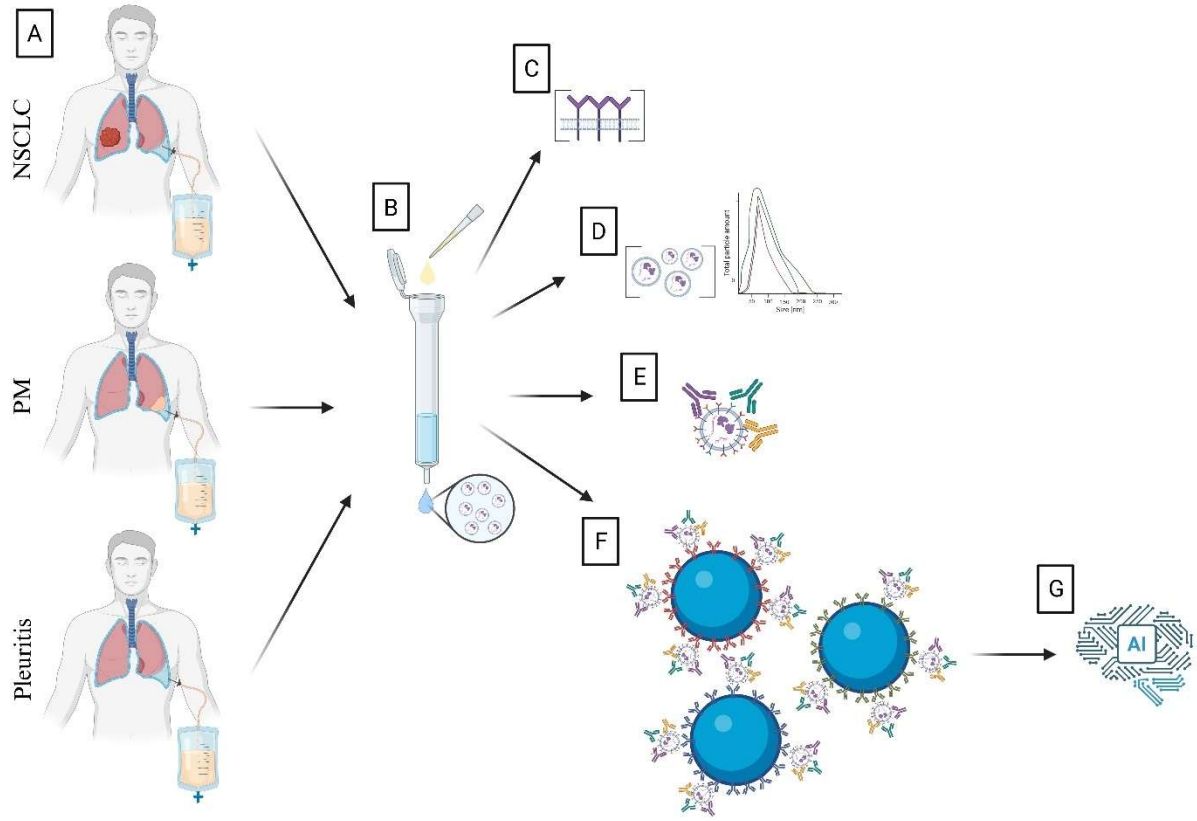

Figure 4.3. Workflow of clinically derived EV analyses. *A) Patient cohort establishment, including individuals with non-small cell lung cancer (NSCLC), pleural mesothelioma (PM), and pleuritis; B) EV isolation from pleural effusions using size exclusion chromatography (SEC); C) Quantification of total protein content using the Qubit protein assay; D) Determination of particle size distribution via nanoparticle tracking analysis (NTA); E) Representative single-EV analysis of tetraspanin expression using nano-flow cytometry (nFCM); F) Multiplex bead-based assay for profiling EV surface marker* expression (MACSPlex EV kit IO, human); G) Application of machine learning algorithms to analyze EV surface marker patterns. *Figure created with Biorender.com.*

4.12. Statistical analyses

4.12.1 In vitro measurements

Statistical analyses were performed using GraphPad Prism 8 (GraphPad Software Inc.). Group-wise comparisons were primarily evaluated using the Kruskal-Wallis test, followed by Dunn's post hoc multiple comparisons test, with a significance threshold set at $p < 0.05$. Unpaired two-tailed t-tests were used to assess statistical significance for pairwise comparisons among the characteristics of enco-bini-resistant cell line clones. Data are presented as mean ± 95% confidence interval if the graph was not conducted to further statistical analyses or when no marker within a given measurement reached statistical significance. If at least one marker was significant, all data of that measurement are shown as mean ± SEM for consistency.

4.12.2. Clinical patient samples

Differences in size distribution derived from nanoparticle tracking analysis (NTA) were evaluated by comparing pairwise the 'malignant' ,'ADC' ,'epithelioid' 'NSCLC', 'cancer', 'cancer in pleura', and 'NSCLC in pleura' groups against the remaining patient groups within each classification scheme. Statistical significance was assessed using the Kolmogorov-Smirnov test, applying a threshold of $p < 0.05$, without adjustments for multiple comparisons.

To compare total protein concentrations, and EV surface marker expression levels between groups, the Kruskal-Wallis test was employed, followed by Dunn's multiple comparison test, with a significance level set at $p < 0.05$. Pairwise comparisons of the groups were statistically examined with the Mann-Whitney U test.

Classification accuracy was evaluated by calculating the hit-to-miss ratio, defined as the number of correct classifications (hits) relative to incorrect classifications (misses), based on the model assigning the highest probability to the correct patient group. For categorical comparisons between patient groups within each classification model and across classification strategies, statistical significance was determined using Fisher's exact test, with Bonferroni correction applied to account for multiple testing.

To assess variations in the machine learning algorithm's performance across different classification schemes, the Kruskal-Wallis test followed by Dunn's post hoc analysis was used, applying a significance threshold of $p < 0.05$.

Receiver Operating Characteristic (ROC) curves were generated to further evaluate the machine learning algorithm's performance, and the corresponding Area Under the Curve (AUC) values were calculated. These metrics provide a comprehensive assessment of the model's discriminative ability across various classification thresholds.

Data are presented as mean ± 95% confidence interval when no marker within a given measurement reached statistical significance. If at least one marker was significant, all data of that measurement are shown as mean ± SEM for consistency. Size-distribution data are consistently displayed as mean ± SEM to facilitate clearer visualization. Statistical significance was defined as $p < 0.05$.

5. Results

5.1. The role of extracellular vesicles in cancer progression and targeted therapy resistance

To investigate the role of EVs in cancer progression and drug resistance, five **cell line pairs** were selected, each consisting of genetically related lines derived from the same patient or subclonal variants. Within each pair, one line represented a less aggressive disease state – either established prior to BRAF inhibitor (BRAFi) therapy (Mel Pt-1 pre, Mel Pt-3 pre, Mel Pt-4 pre) or derived from a primary tumor (WM983A, A2058) – while the counterpart reflected a more advanced phenotype, such as cells isolated during BRAFi treatment (Mel Pt-1 post, Mel Pt-3 post, Mel Pt-4 post), from metastatic sites (WM983B), or highly tumorigenic subclones (M1). This design minimized inter-individual variability and ensured molecular compatibility between donor and recipient cells, reducing the risk of surface marker incompatibility that could hinder EV binding or uptake due to differences in cell surface composition across individuals.

Functional assays were performed by treating cells with either their own EVs or those derived from their respective pair. This approach allowed us to assess whether cell lines with different levels of aggressiveness release EVs with distinct properties and biological effects. In particular, we examined whether EVs from more aggressive (or BRAFi-resistant) cells could alter the phenotype of less aggressive (or BRAFi-sensitive) cells, and vice versa, thereby highlighting the potential role of EVs in modulating tumor behavior.

5.1.1 Extracellular vesicles promote cell migration over proliferation and sphere growth

5.1.1.1. Characterization of the isolated extracellular vesicles

Cells were cultured under serum-starved conditions for 72 hours to facilitate EV production. Following this incubation period, the conditioned media were collected, filtered, and subjected to differential ultracentrifugation for EV isolation. The **success of the isolation** was initially assessed using Dynamic Light Scattering (DLS). Which were considered successful if the main population size fell within the expected range for EVs derived from cell culture supernatants [2], and if the EV-depleted supernatant lacked particles larger than 10 nm (data not shown).

Subsequently, total particle count and size distribution of the EV isolates were determined using Nanoparticle Tracking Analysis (NTA). These measurements were performed on a representative sample from each isolation to further validate the efficacy of the isolation process. The mean particle size ranged from 125 to 179 nm (Figure 5.1A-B), and particle concentrations varied between 8.3×10^9 and 3.5×10^{10} particles/mL (Figure 5.1B), aligning with previously published data for EVs isolated from cell culture media [295], [296]. Lipid and protein content of the isolates

were compared within each pair of pair; however, no statistically significant differences were observed (Figure 5.1C-D). The expression of common EV surface markers on representative samples – including EpCAM, tetraspanins (CD9, CD63, CD81), and Annexin [37], [297], [298] – was confirmed using bead-based flow cytometry (Figure 5.1E). Among these, CD63 exhibited the lowest expression levels across samples (Figure 5.1E).

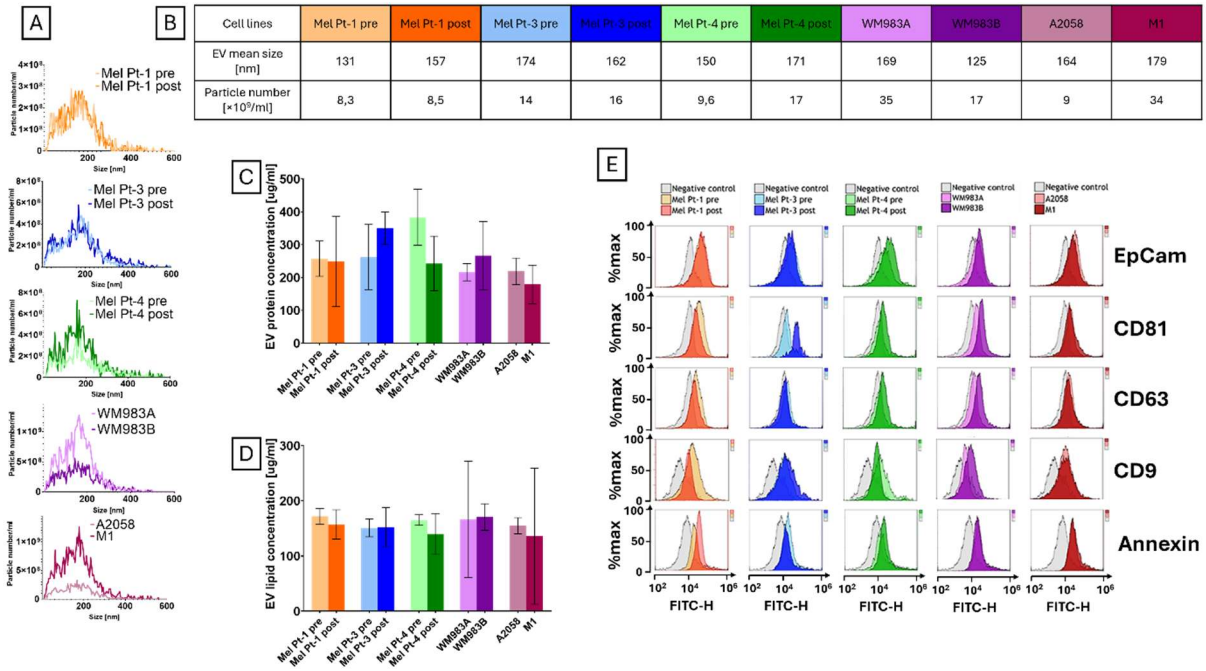

Cell lines	Mel Pt-1 pre	Mel Pt-1 post	Mel Pt-3 pre	Mel Pt-3 post	Mel Pt-4 pre	Mel Pt-4 post	WM983A	WM983B	A2058	M1
EV mean size [nm]	131	157	174	162	150	171	169	125	164	179
Particle number [×10⁹/ml]	8,3	8,5	14	16	9,6	17	35	17	9	34

Figure 5.1. Characterization of extracellular vesicles isolated from cell culture supernatants. *A) Particle size distribution profiles of EV isolates assessed by NTA; B) Mean particle size and concentration for each EV preparation; C) EV-associated protein content quantified using the Qubit protein assay (mean±95%* confidence interval*); D) Lipid content of EV isolates measured by SPV assay across the examined cell lines (mean±95%* confidence interval*); E) Surface marker profiling of EVs conducted via multiplex bead-based flow cytometry; Modified figure from Németh et al. 2024.*

5.1.1.2. EV treatment exhibit minimal impact on proliferation and sphere growth

Following the successful isolation and characterization of EVs, their impact on primary tumor progression was evaluated using functional assays focused on two-dimensional (2D) cell proliferation and 3D spheroid growth. For 2D cell proliferation measurements, cells were treated with their respective EVs for 72 hours, after which proliferation was assessed via SRB assay. Among all tested conditions (10 µg/ml of EVs, normalized to protein content), only the **Mel Pt-1 pre** EVs and **WM983B**-derived EVs led to a significant increase in the proliferation of their parental cells. In all other cases, EV exposure had no notable effect, maintaining baseline proliferative capacity.

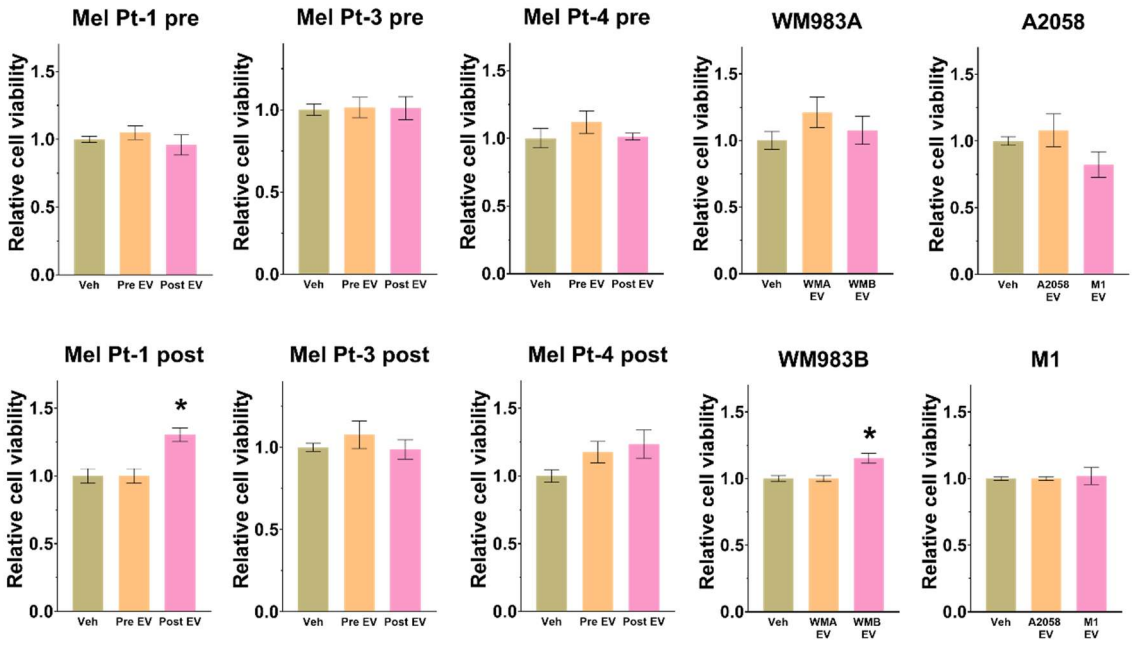

Figure 5.2. Effects of EV treatment on cell proliferation. *The 2D cell proliferation was assessed via SRB staining following 72 hours of EV exposure. Asterisks denote statistically significant differences compared to vehicle controls, as determined by the Kruskal-Wallis test followed by Dunn's post hoc analysis. Data represent the mean ± SEM from three independent experiments. Differences were considered significant at $p < 0.05$. Modified figure of Németh et al. 2024.*

To assess EV effects in a more physiologically relevant 3D context, spheroids were generated using U-bottom, poly-HEMA-coated plates supplemented with 0,04 mg/ml collagen. Once formed, spheroids were treated with 10 µg/ml of EVs (normalized to protein content), and growth was monitored over seven days. Quantitative analysis of spheroid development revealed **no increase in growth** across conditions. Furthermore, differences were not observed in response to EVs derived from either the more or less aggressive counterparts within each cell line pair (Figure 5.3).

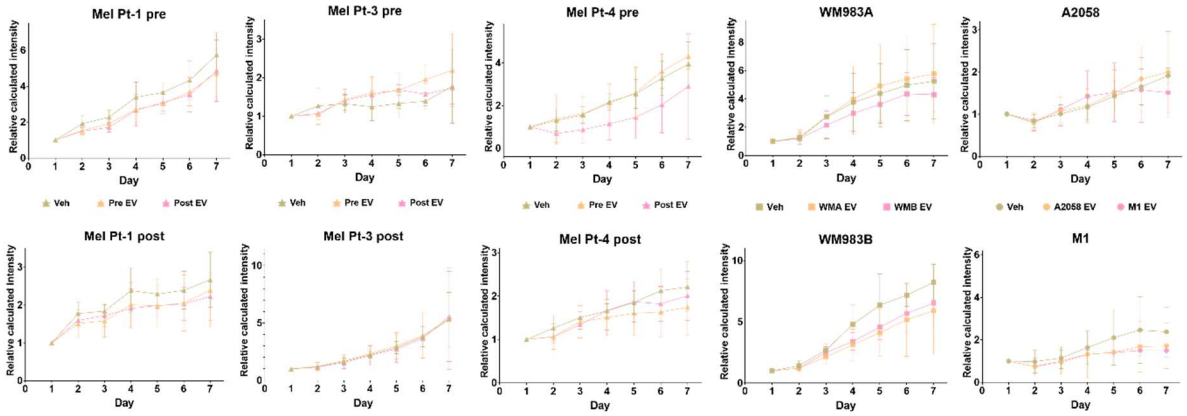

Figure 5.3. Impact of extracellular vesicle treatment on 3D spheroid development. *Spheroids were cultured for seven days and imaged daily. Growth was quantified based on multiple parameters, including diameter, area, integrated density, and median pixel intensity. The relative signal intensity is presented as the mean ± 95% confidence interval (N = 6). Modified figure of Németh et al.2024.*

5.1.1.3. EVs have more enhanced effect on cell migration

Subsequently, the role of EVs in 2D cell migration – a critical process in metastatic progression – was examined. To enable the assessment of individual cell motility and ensure uniform EV exposure, cells were seeded at low density (1000 cells/well), allowing multidirectional movement. Each cell line was treated with both its own EVs and those derived from its corresponding pair, using the same EV concentration applied in prior experiments. Migration was monitored over a 24-hour period using time-lapse video microscopy, capturing images at 10-minute intervals. Semiautomated single cell tracking was performed with CellTracker software [294] (Figure 5.4). Based on the x-y coordinates of the tracked cells, Mean Square Displacement (MSD) and Total Travelled Distance (TTD) were calculated and represented as a function of time in TableS1. To facilitate statistical comparison, ΔAUC values were determined from the time-dependent migration curves.

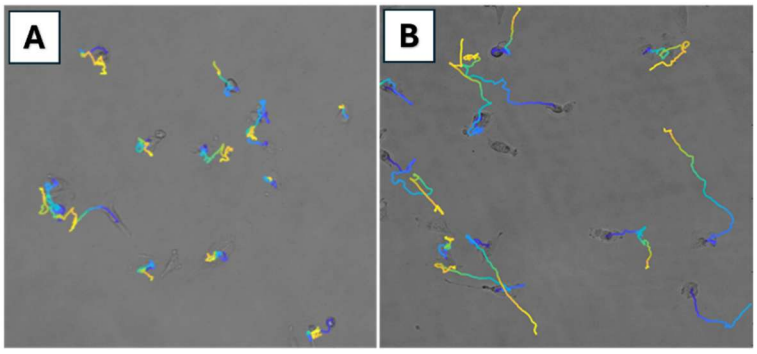

Figure 5.4. Representative trajectories from single cell tracking. *Individual cells were monitored over a 24-hour period using CellTracker [294], and each cell's migration path is visualized as a distinct coloured line. A) Vehicle-treated control; B) Mel Pt-4 post cells treated with EVs derived from their corresponding line. Modified figure from Németh et al. 2024.*

EV treatments generally led to an increase in migratory capacity, with the notable exception of the A2058 cell line (Figure 5.5E). In **Mel Pt-1 pre** cells, migration remained statistically unchanged following EV exposure, although a modest increase was noted upon treatment with their own EVs (Figure 5.5A). For **Mel Pt-1 post** cells, EVs from both sources induced a mild enhancement in cell migration, reflected in increased MSD and TTD values (Figure 5.5A). In the **Mel Pt-3 pre** line, a slight elevation in MSD was observed with self-derived EVs, and a statistically significant increase occurred upon treatment with EVs from the more aggressive counterpart. A similar, though non-significant, trend was evident for TTD (Figure 5.5B). **Mel Pt-3 post** cells also displayed minor increases in TTD with both EV types (Figure 5.5B). In **Mel Pt-4 pre** cells, TTD values indicated a subtle increase in motility following either EV treatment, while no considerable change was observed in MSD (Figure 5.5C). Conversely, **Mel Pt-4 post** cells exhibited a significant rise in MSD after exposure to EVs from their paired line and a mild, non-significant elevation after treatment

with autologous EVs. TTD followed a comparable trend without reaching statistical significance (Figure 5.5C). For **WM983A and WM983B** cells, both autologous and paired EVs enhanced migration consistently across both MSD and TTD parameters (Figure 5.5D). In contrast, **A2058** cells exhibited a decrease in migration upon exposure to their own EVs, with a significant reduction in TTD (Figure 5.5E). M1-derived EVs had minimal influence on MSD in both A2058 and **M1** cells, while TTD showed a tendency to decrease under these treatments (Figure 5.5E).

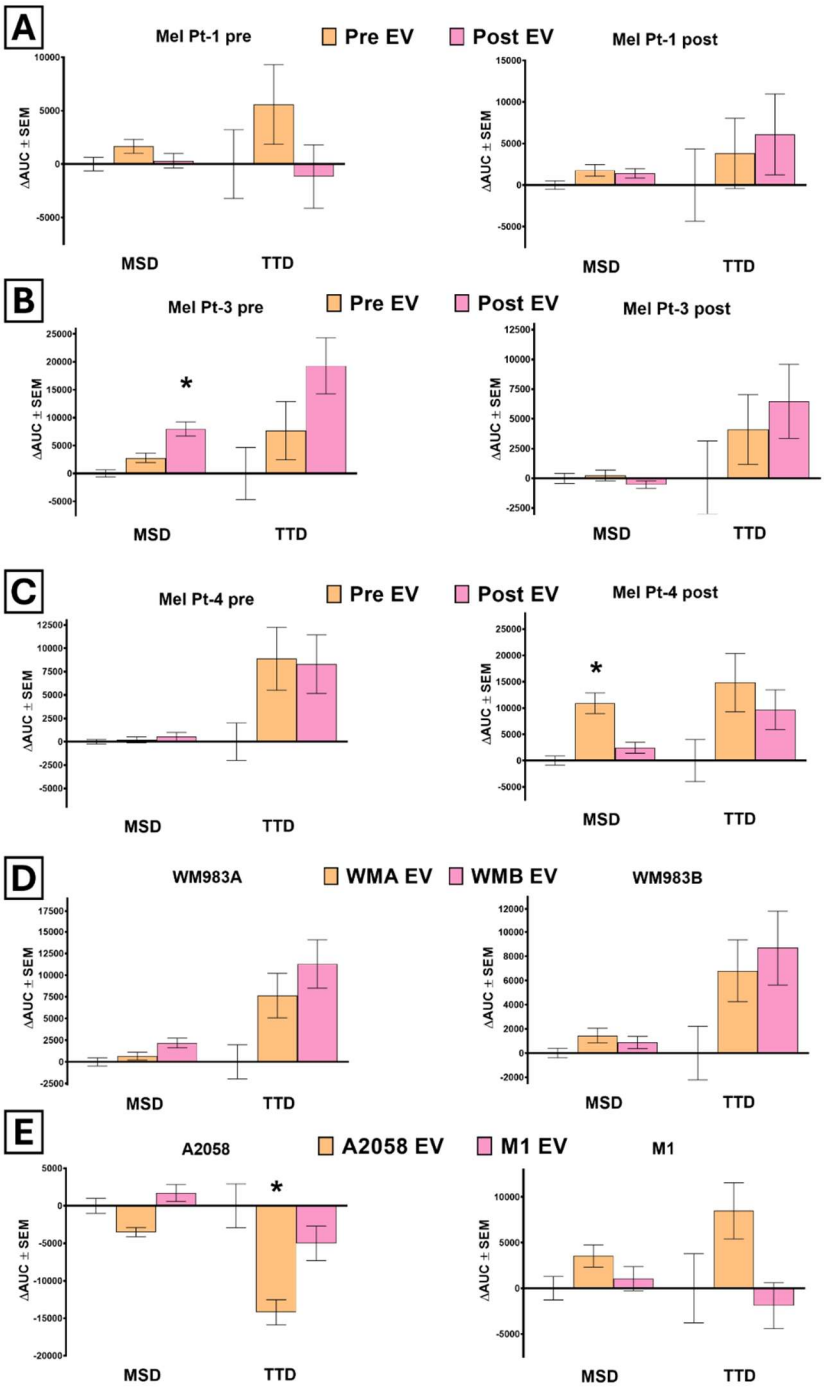

Figure 5.5 *(See legend on next page.)*

Figure 5.5. Effects of extracellular vesicles on melanoma cell migration. *Cells were treated with either their own EVs or those derived from their corresponding pair, and migration was monitored over a 24-hour period using semi-automated tracking via the CellTracker [294]. From the recorded x-y coordinates, mean squared displacement (MSD) and total track distance (TTD) were calculated. To facilitate statistical comparison, the time-dependent migration curves were summarized by calculating the ΔAUC values for MSD [μm²×min] and TTD [μm×min], which is presented in the figure. Panels show the results for: A) Mel Pt-1, B) Mel Pt-3, C) Mel Pt-4, D) WM983A and WM983B, and E) A2058 and M1 cells. Data are shown as mean ± SEM from three independent experiments. Asterisks indicate statistically significant differences compared to vehicle controls, determined using Kruskal-Wallis test followed by Dunn's multiple comparisons test ($p < 0.05$). Figure adapted from Németh et al. 2024.*

5.1.2. Extracellular vesicles promote cell migration despite BRAF inhibitor treatments

Following the observation that EVs exerted a more pronounced effect on 2D cell migration than on proliferation or spheroid growth, I next examined whether this migration-promoting influence persisted under BRAF inhibitor (BRAFi) treatment. Vemurafenib, a clinically utilized BRAFi, was selected for this analysis due to the prior exposure of Mel Pt cell lines to this compound. Moreover, all remaining cell lines (WM983A, WM983B, A2058, and M1) harbor BRAF V600E mutation, which is the primary target of vemurafenib.

To assess the impact of EVs on **vemurafenib** resistance, the drug **sensitivity** of each cell line was first determined (Figure 5.6). Among the five cell line pairs, Mel Pt-3, Mel Pt-4, and WM983A/WM983B exhibited marked differences in sensitivity. As anticipated, Mel Pt-3 pre and WM983A cells were more sensitive to vemurafenib compared to their respective counterparts. Interestingly, Mel Pt-4 pre cells displayed a more resistant phenotype relative to the post cell line. In the following sections, cell lines are referred to as resistant if their viability was less affected by a given drug concentration compared to their counterparts.

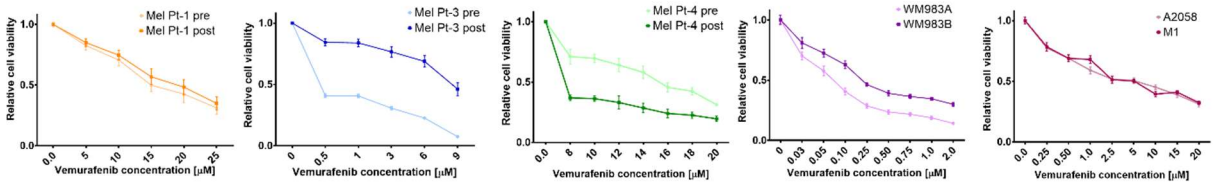

Figure 5.6. Melanoma cell line pairs vemurafenib sensitivity. *Cells were exposed to vemurafenib for 72 hours and cell proliferation assay (SRB assay) was used to access cell lines BRAFi sensitivity. Data is represented as mean ± 95% confidence interval from three independent experiments. Modified figure of Németh et al. 2024.*

Each cell line was treated with vemurafenib during the resistance investigating around their GI50 values: Mel Pt-1 and Mel Pt-4 pre and post at 10 μM, Mel Pt-3 pre at 0.75 μM and post at 7.5 μM, WM983A at 0.05 μM, WM983B at 0.25 μM, and A2058 and M1 at 2.5 μM.

In Figure 5.7. ΔAUC results from EV treatment only is also represented to visualize changes compared to those experiments too, while parameters in function of time presented in Table S2. Vemurafenib generally reduced cell migration, except for Mel Pt-3 post, WM983A and WM983B

cells TTD parameter. Significantly higher MSD was measured in the more sensitive cells (**Mel Pt-3 pre, Mel Pt-4 post and WM983A**) uppon treatment with vemurafenib and EVs from the more resistant cells as compared to vemurafenib treatment. Albeit the same effect in TTD was significant only in WM983A cells. In combination with EVs, vemurafenib demonstrated the ability to attenuate the modest migration-promoting effect of EVs in **Mel Pt-1 pre and post cells**. In case of **A2058** and **M1** cells, EVs were unable to significantly counteract the migration-inhibitory effect of vemurafenib, with the exception observed in TTD of A2058 cells when treated with vemurafenib in combination with M1-derived EVs. In the more resistant cells (**Mel Pt-3 post, Mel Pt-4 pre and WM983B**) no significant difference in MSD and TTD was detected when treated with vemurafenib alone or in combination with EVs.

5.1.3. Extracellular vesicle-mediated migration is altered under BRAF and MEK inhibitor co-treatment

Following the development of the first BRAF inhibitor, vemurafenib, a second-generation compound, **dabrafenib**, was introduced and is often administered in combination with the MEK inhibitor **trametinib**. To determine whether EV-mediated therapy resistance remains effective under these additional treatment regimens, I expanded my analysis to include MEK inhibitor monotherapy and BRAF/MEK inhibitor co-treatment.

As a first step, I assessed the **baseline sensitivity** of selected cell lines – those previously shown to differ in their response to vemurafenib. In general, cell lines representing less advanced tumor stages (Mel Pt-3 pre, Mel Pt-4 pre, and WM983A) were more responsive to dabrafenib or trametinib monotherapies (Sup Figure 1). The combined dabrafenib and trametinib treatments were applied at three different concentration (Figure 5.8A, Sup Figure 2A), and combination index (CI) values were calculated to evaluate potential synergistic effects (Figure 5.8B, Sup Figure 2B). In nearly all cases, the CI values were below 1, supporting the previously observed synergy between the two drugs [299]. A single exception was observed in WM983B cells at the highest dabrafenib dose, where the CI exceeded 1 (Sup Figure 2B).

To further explore whether EVs can influence resistance under these more complex treatment conditions, I selected the Mel Pt-3 cell line pair. These cells were ideal due to their markedly different responses to vemurafenib, dabrafenib, trametinib, and their combination (Figure 5.6 and Figure 5.8A), as well as their relatively high intrinsic migration capacity (Table S1).

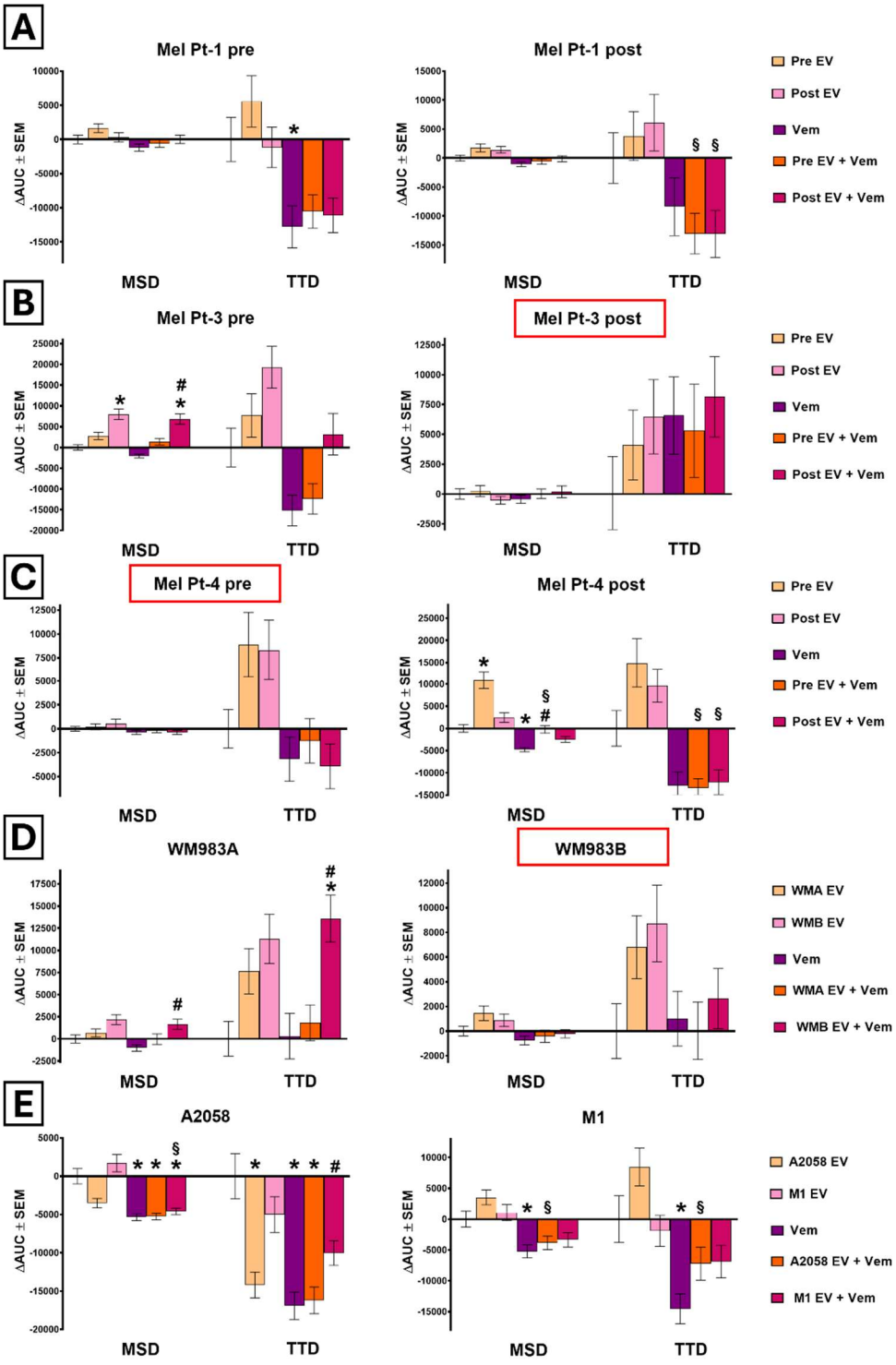

Figure 5.7. Impact of EV, vemurafenib (Vem) and combined (EV+Vem) treatment on single-cell migration. *Cells were tracked over a 24-hour period using semi-automated tracking via the CellTracker [294]. From the cells' x-y coordinates, mean squared displacement (MSD) and total travelled distance (TTD) were calculated. To facilitate statistical comparison, the time-dependent migration curves were summarized by calculating the ΔAUC values for MSD [μm²×min] and TTD [μm×min], which is presented in the figure. Panels show the results for: A) Mel Pt-1, B) Mel Pt-3, C) Mel Pt-4, D) WM983A and WM983B, and E) A2058 and M1 cells. Red rectangles indicate the more resistant cell lines. Data are shown as mean ± SEM from three independent experiments. Statistically significant differences were determined using Kruskal-Wallis test followed by Dunn's multiple comparisons, test p-value less than 0.05 considered as statistically significant (to vehicle: *, to Vem: #, to EV-only: §). Modified figure from Németh et al. 2024.*

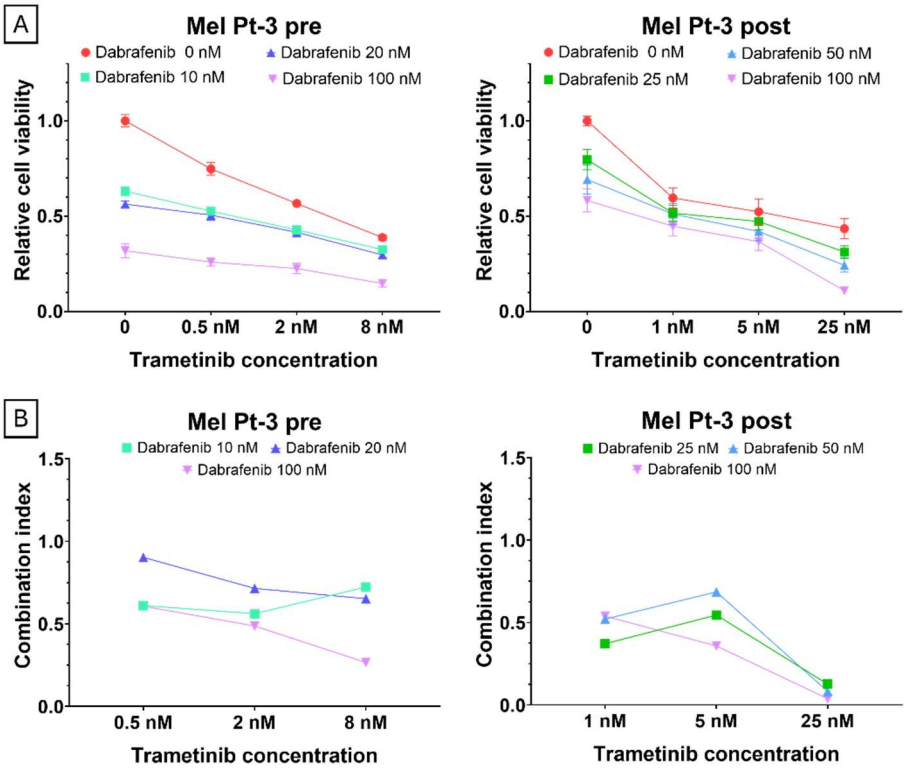

Figure 5.8. Mel Pt-3 cell line pair dabrafenib-trametinib combination treatment sensitivity. *A) Relative cell viability for the selected three concentrations of BRAFi and MEKi, which was determined using SRB cell viability assay. Data represented as mean± 95% confidence interval (N=3); B) Calculated combination indexes (CI) for each combination, CI<1 synergism, CI=1 additive effect, CI>1 antagonism. Adapted figure of Németh et al. 2024.*

Video microscopy-based migration analysis was conducted as previously described, and the corresponding ΔAUC values are shown in Figure 5.9. Time dependent MSD and TTD curves are provided in Table S3. In **Mel Pt-3 pre** cells, treatment with dabrafenib, trametinib, or their combination led to a reduction in both MSD and TTD values (Figure 5.9). However, a statistically significant decline was observed only in MSD during single-agent treatments (Figure 5.9A). In **Mel Pt-3 post** cells, MSD also decreased relative to the vehicle control, while TTD exhibited a slight increase, particularly in conditions involving a BRAF inhibitor – mirroring trends seen under vemurafenib treatment (Figure 5.9).

In experiments using **Mel Pt-3 pre** cells, EVs from both the pre and post cell lines were able to compensate dabrafenib-induced migration inhibition, significantly restoring MSD values (Figure 5.9). Notably, EVs from the resistant (post) cells exhibited a stronger compensatory effect. In contrast, trametinib appeared to attenuate EV-mediated rescue, as evidenced by significantly reduced MSD values in co-treated cells compared to those receiving EVs alone (Figure 5.9A). These effects were less equivocal when analyzing TTD (Figure 5.9B). In the case of **Mel Pt-3 post**

cells, migration changes were generally subtle, yet a modest enhancement in cell motility was observed when EVs were applied in combination (Figure 5.9).

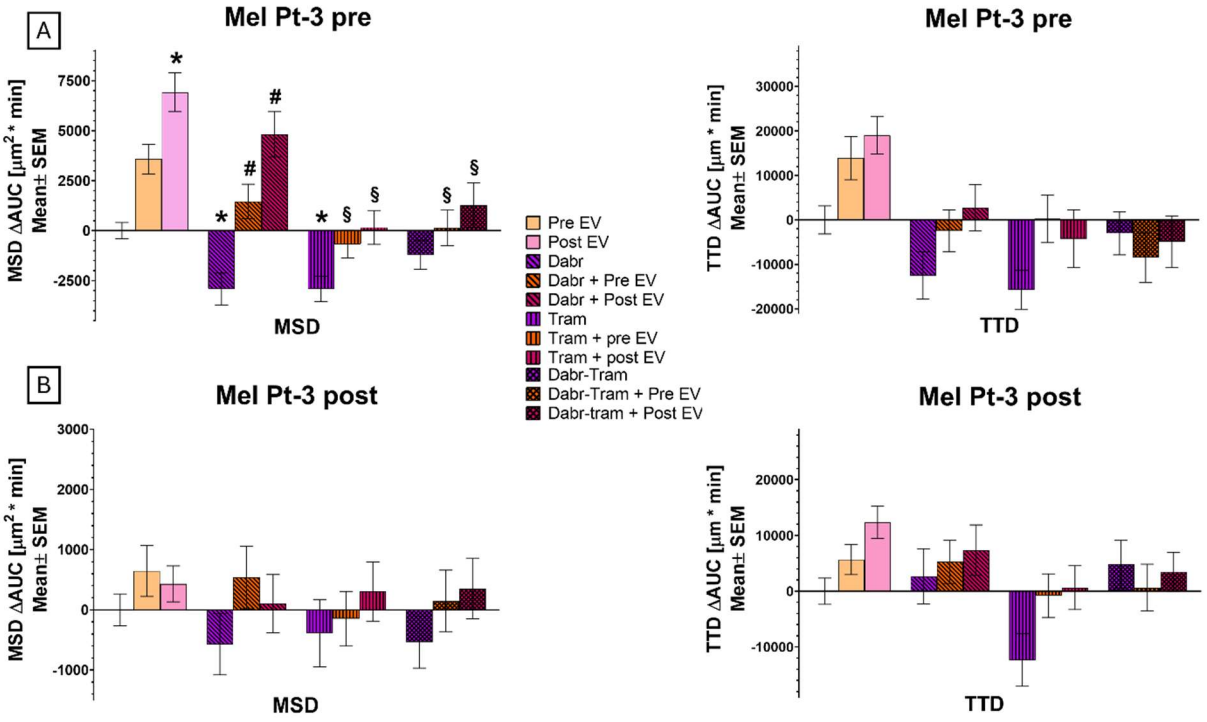

Figure 5.9. Impact of EVs, dabrafenib (Dab), trametinib (Tram), and their combination on single-cell migration *Cells were tracked over a 24-hour period using semi-automated tracking via the CellTracker [294]. From the cells' x-y coordinates, A) mean squared displacement (MSD) and B) total travelled distance (TTD) were calculated. To facilitate statistical comparison, the time-dependent migration curves were summarized by calculating the ΔAUC values, which is presented in the figure. Statistically significant differences were determined using Kruskal-Wallis test followed by Dunn's multiple comparisons, test p-value less than 0.05 considered as statistically significant (to vehicle: *, to Vem: #, to EV-only: §). Modified figure from Németh et al. 2024.*

A major **limitation of this model** is that the original patient had only been treated with a BRAF inhibitor, and the derived cell lines were not previously exposed to combined BRAFi-MEKi therapy. Consequently, after finding that EVs could counteract the effects of the inhibitor used in the patient but not the dual inhibition, I aimed to develop cell lines resistant specifically to the BRAFi-MEKi combination.

5.1.3.1. Cell characteristic changes following acquisition of BRAF/MEK inhibitor resistance

To generate BRAF-MEK inhibitor–resistant cell line clones, encorafenib (enco) and binimetinib (bini) were selected, as they represent the most clinically advanced and promising agents within this class of inhibitors (see Section 2.3.3.1). Following careful evaluation, Mel Pt-3 pre and Mel Pt-4 post cell lines were selected to develop clones resistant to enco and bini. The **selection criteria**

were based on their intrinsic migratory capacity and responsiveness to EV-induced modulation. Mel Pt-3 post was excluded from further analyses due to its low baseline motility and lack of significant response to EV treatment. The choice of inhibitors was guided by the current clinical preference for BRAFi-MEKi combinations.

To begin, the **drug sensitivity** of both cell lines to monotherapies and combined treatments was assessed (Sup Figure 3 and Figure 5.10A). Mel Pt-3 pre cells demonstrated higher sensitivity to both single agents and the combination regimen. Based on the baseline sensitivities, cells were subjected to a long-term, stepwise drug adaptation protocol, starting at 1 nM encorafenib and 1 nM binimetinib. Drug concentrations were incrementally increased when treated cells reached confluency within the same timeframe as their parental counterparts. Drug sensitivity was monitored periodically using the SRB assay (data not shown).

Despite initial attempts, Mel Pt-3 pre cells exhibited reduced proliferation before stable resistance could be achieved. In contrast, **successful generation of a resistant clone** was accomplished after 8 months in **Mel Pt-4 post** cells (at 205-205 nM). A shown in Figure 5.10 the resistant clone (darker colors) relative cell viability was higher in almost all applied concentrations. In addition, combination index (CI) values were calculated for each treatment condition, confirming synergistic effects (CI < 1) in all tested combinations, which is in line with earlier findings [300]. After the resistant clone was established multiple vials of them were cryopreserved at -80°C for future use. From this point forward, the parental line will be referred to as Mel Pt-4 post sens, and the resistant derivative as Mel Pt-4 post res.

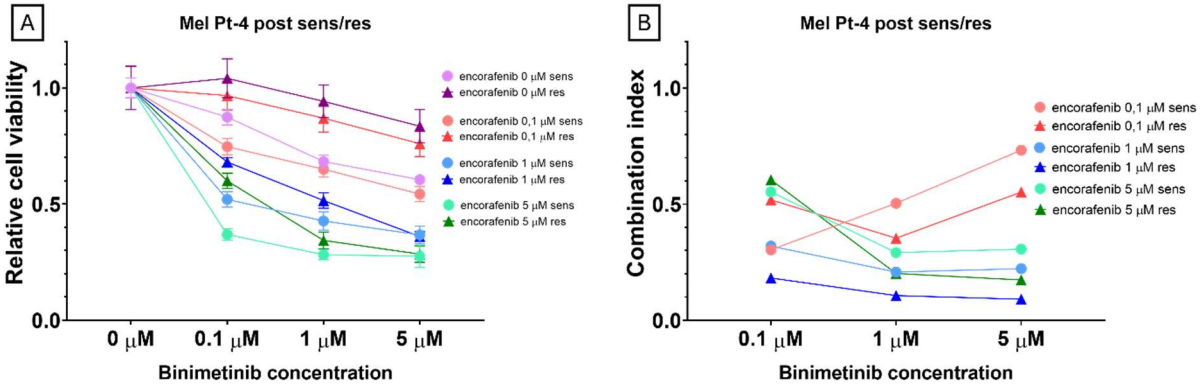

Figure 5.10. Comparison of the parental and enco-bini resistant cell clone cell viability. *A) Combination treatment of both cell lines, relative cell viability was measured by SRB assay, data represented as mean ± 95% confidence interval (N=3); B) Combination indexes (CI) for the applied treatments, CI<1 synergism, CI=1 additive effect, CI>1 antagonism.*

Drug exposure not only **altered** the cell lines' sensitivity to the combination treatment but also induced changes in **proliferation, migratory capacity, cellular morphology, and EV production** (Figure 5.11). The resistant cell line exhibited significantly reduced proliferation (Figure 5.11A) and

migration, as indicated by lower MSD values (Figure 5.11C), compared to its parental, treatment-sensitive counterpart. Morphologically, drug-adapted cells displayed a more elongated phenotype (representative images shown in Sup Figure 4), reflected by decreased circularity values, while cell size remained unchanged (Figure 5.11B). This elongation may be indicative of an epithelial-to-mesenchymal transition (EMT)-like shift [301]. EV secretion was also assessed (Figure 5.11D), showing a trend toward increased EV release in the resistant clones, with statistically significant differences observed in lipid content. However, the size distribution of the vesicles remained comparable between the sensitive and resistant cells.

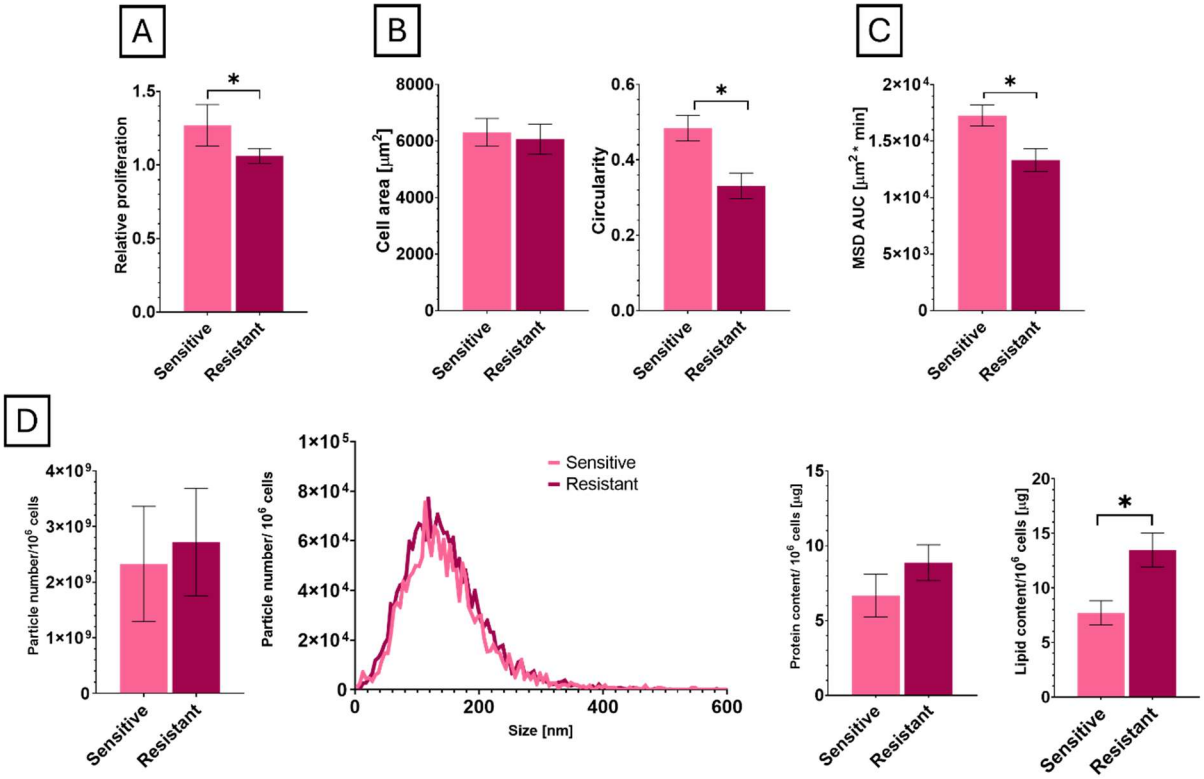

Figure 5.11. Characterization of parental and resistant melanoma cell line clones. *24-hour video microscopy recordings were performed to assess alterations in cell size, morphology, proliferation rate, and migratory capacity. A) Relative proliferation rates were calculated based on changes in cell number over 24 hours; B) Cell size and circularity was measured using ImageJ software to evaluate morphological changes; C) Individual cell trajectories were tracked semi-automatically using CellTracker, and mean square displacement (MSD) was calculated from the recorded xy coordinates; the area under the curve (AUC) values are presented; D) Characterization of isolated extracellular vesicles: particle concentration and size distribution were evaluated by NTA, protein content was determined by Qubit protein assay and lipid content by SPV assay. Data are presented as mean ± SEM (in case of size-distribution only mean). Asterisks indicate statistically significant differences, which was assessed using unpaired t-tests, with a significance threshold set at $p < 0.05$.*

5.1.3.2. Extracellular vesicle preconditioning protects cells from BRAF/MEK inhibitor-induced migration inhibition

After establishing the enco-bini-resistant clone, drug resistance was evaluated in the context of cell migration. To ensure the stability of the resistant phenotype, freshly thawed cryopreserved vials were used for each experiment. EVs were applied at the previously established concentration (10 µg/mL of EVs, normalized to protein content), and enco-bini was administered at 205 nM each, consistent with the final concentrations used during resistance induction. Migration assays were conducted as previously described, with modifications to the treatment regimen: EVs were applied either concurrently with encorafenib–binimetinib or as a 24-hour pretreatment before drug exposure. This design allowed assessment of whether EV-mediated resistance is primarily mediated by drug binding or internalization, as pretreatment EVs were removed prior to the addition of drug-containing medium, preventing direct drug encapsulation.

Given that earlier findings showed a more pronounced EV-mediated effect on the MSD parameter compared to TTD, only MSD-derived ΔAUC values were analyzed here (Figure 5.12; time-resolved MSD data are provided in Table S4). Interestingly, both EV-treatment alone slightly decreased MSD in both cell lines. In the sensitive cell line, all treatment conditions involving BRAF and MEK inhibition prominently impaired migration relative to vehicle control. Importantly, EV preconditioning attenuated the inhibitory impact of enco-bini treatment on cell motility. In the resistant cell line, migration was reduced by both EV and enco-bini treatments, though this reduction was less pronounced following EV preconditioning. Under these conditions, no significant difference was observed between the effects of EVs from sensitive or resistant sources. Overall, in this model system I was unable to confirm that EVs transfer dual therapy resistance.

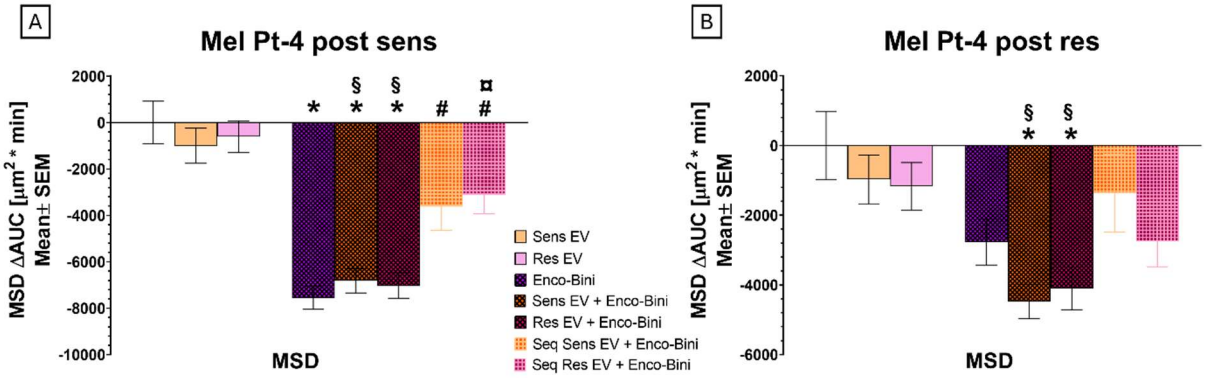

Figure 5.12. Extracellular vesicles, enco-bini and their combination effect on cell migration. *Cells were tracked over a 24-hour period using semi-automated tracking via the CellTracker [294]. From the cells' x-y coordinates, A) mean squared displacement (MSD) and B) total travelled distance (TTD) were calculated. To facilitate statistical comparison, the time-dependent migration curves were summarized by calculating the ΔAUC values, which is presented in the figure. A) Mel Pt-4 post sensitive under sens/res EV, enco-bini, sens/res EV + enco-bini (simultaneously) and Seq sens/res EV + enco-bini (EV sequentially); B) Mel Pt-4 post resisitant sens/res EV, enco-bini, sens/res EV + enco-bini (simultaneously) and Seq sens/res EV + enco-bini (EV sequentially). Statistically significant differences were determined using Kruskal-Wallis test followed by Dunn's multiple comparisons, test p-value less than 0.05 considered as statistically significant (to vehicle: *, to Enco-Bini: #, to EV-only: § to EV + Enco-Bini: ¤).*

5.2. Pleural fluid derived extracellular vesicles as potential biomarkers for thoracic malignancies

Having elucidated the contribution of EVs to tumor progression and targeted-therapy resistance, I next assessed their diagnostic potential. EVs circulate in virtually all body fluids, and pleural effusion – readily obtainable from patients with non-small-cell lung cancer (NSCLC), pleural mesothelioma (PM), and non-malignant pleuritis – was selected as the test matrix, as it is in direct contact with the tumor and contains soluble factors, cells, and EVs that reflect the tumor microenvironment [212], [213]. Firstly, a patient cohort was assembled (see detailed in Methods section 4.7). Pleural fluids were processed by size-exclusion chromatography and filtration to obtain EV-enriched fractions. NTA measurements showed **particle-size distributions** centred within the canonical EV range [289]. Interestingly, NSCLC patient-derived EVs showed slightly more elongated distribution curves: mean interquartile diameters were 105-255 nm for NSCLC, 105-165 nm for PM and 105-165 nm for pleuritis, however, these were not significant inter-group differences (Figure 5.13A). Total **protein content** of the isolates did not differ significantly across diagnoses (Figure 5.13B). In accordance with MISEV 2023 recommendations [2], single-particle characterisation was performed by nano-flow cytometry on representative samples. Surface expression of the tetraspanins CD9, CD63 and CD81 confirmed the vesicular nature of the isolates and verified marker presence at the **individual-EV level** (Figure 5.13C).

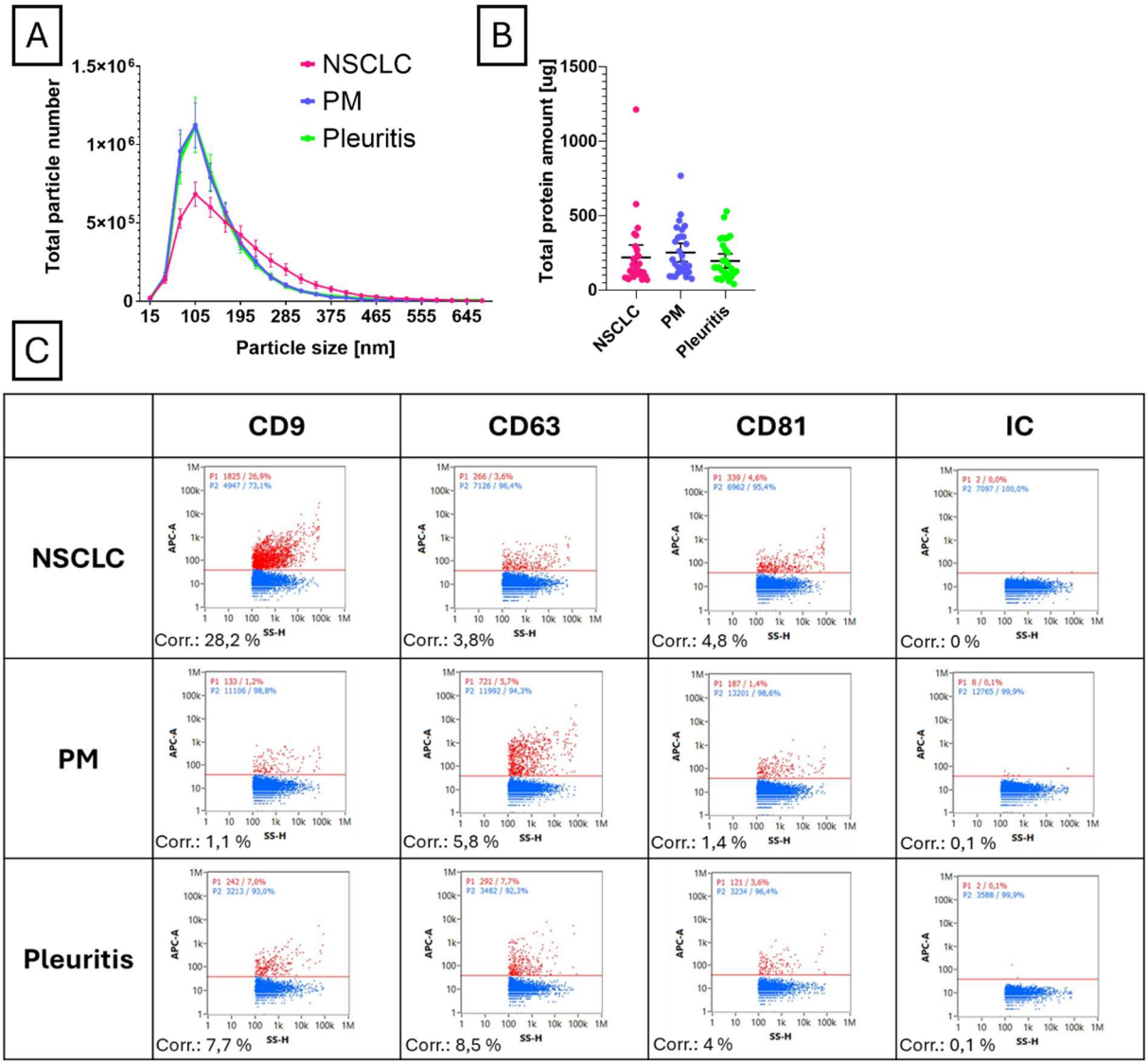

Figure 5.13. Characterization of the pleural effusion-derived EV fraction. *A) Mean ± SEM of particle size distribution curves, as determined by NTA; B) Total protein concentration of EV isolates quantified using the Qubit protein assay, presented as mean ± 95% confidence interval; C) Single-EV surface expression of CD9, CD63, and CD81 tetraspanins, along with isotype controls, measured by nFCM in representative samples (N = 3). The P1 gate defines the population of positive particles, with gating established using antibody-only controls and corrected values (Corr.) adjusted to subtract background signals measured in PBS controls.*

5.2.1. CD44, CD326 and MCSp differently expressed in NSCLC, PM and pleuritis patients

After confirming the presence of EVs, their surface marker expression profiles were analyzed using a **bead-based multiplex assay** on EVs isolated from each patients' pleural effusion sample. For these analyses the grouping was based on the patients' 'initial' diagnosis. A total of 37 surface markers and 2 isotype controls were assessed. Following background correction and normalization, 25 markers – including MCSp, ROR1, HLA-DRDPDQ, HLA-ABC, CD326, CD146, CD105, CD81, CD63, CD62P, CD49e, CD45, CD44, CD42a, CD41b, CD40, CD31, CD29, CD24, CD14, CD11c, CD9, CD8, CD4, and CD2 – showed higher expression than the isotype controls across all three patient groups (Figure 5.14). Of these, 14 markers (ROR1, HLA-DRDPDQ, CD326

– except in PM, CD105, CD81, CD63, CD49e – except in NSCLC, CD44, CD42a, CD40, CD29, CD24, CD14, and CD9) exhibited normalized mean APC intensities ≥15. The 25 **markers** detected on the EVs were **categorized** based on their biological function and cellular origin: EV markers (CD9, CD63, CD81), cancer-associated/stemness markers (CD24, CD326, ROR1, MCSp), immune-related markers (CD2, CD4, CD8, CD11c, CD14, CD40, CD45, HLA-ABC, HLA-DRDPQ), adhesion and migration markers (CD29, CD49e, CD44, CD105, CD146), platelet-associated markers (CD41b, CD42a, CD62P), and angiogenesis/endothelial markers (CD31, CD105) (Figure 5.15A). Overall, when grouped by biological function, the EV marker profiles appeared similar across the three patient cohorts, with no major group-level differences observed. In all three patient groups, canonical EV markers constituted the largest proportion of total EV surface signal (Figure 5.15B), suggesting a relatively low level of platelet contamination – unlike what I observed in plasma-derived EVs, which typically showed a higher platelet marker presence (Sup Figure 5). EVs from NSCLC patients exhibited a higher expression of cancer-associated/stemness markers compared to the other two groups, while slightly increased levels of adhesion and migration markers characterized pleuritis samples (Figure 5.15B).

Statistically significant **differences between the individual markers** of the patient groups are highlighted in Figure 5.14, where individual patient data for these markers are also visualized. Notably, **CD44** – a hyaluronan receptor – was significantly elevated in PM samples compared to NSCLC and pleuritis. Although CD14, CD29, CD40, and CD42a followed a similar trend, the differences did not reach statistical significance. **MCSp** (melanoma chondroitin sulfate proteoglycan) expression was significantly higher in PM compared to pleuritis. Conversely, the epithelial cell adhesion molecule **CD326** (EpCAM) was significantly elevated in NSCLC samples relative to the other conditions, and HLA-DRDPDQ was also increased in NSCLC patients. Other surface markers analyzed did not show substantial differences among the groups (Figure 5.14).

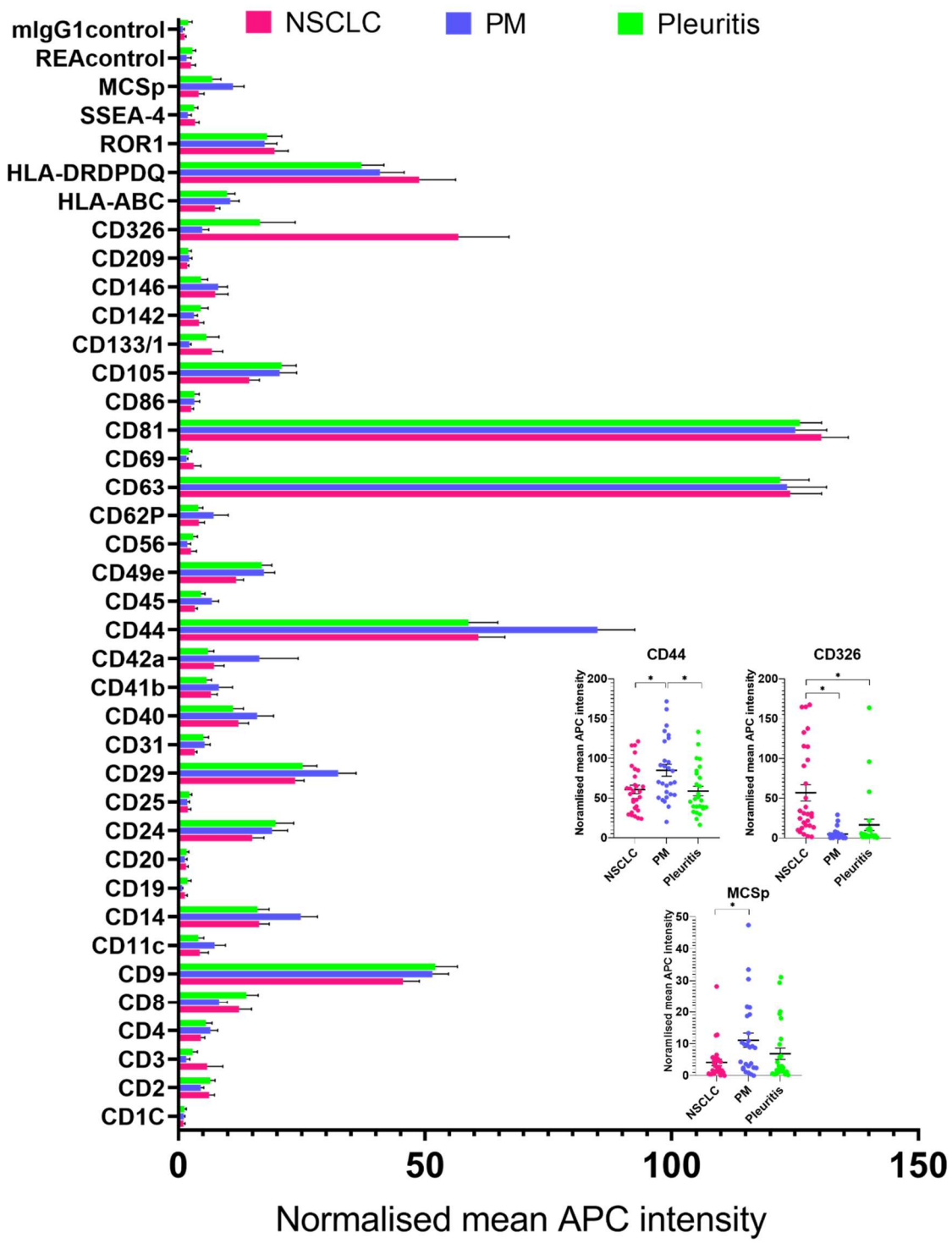

Figure 5.14. EV surface marker profiles differentiate pleural effusion samples from NSCLC, PM, and pleuritis patients. *Extracellular vesicles isolated from pleural effusion samples were analyzed for surface marker expression using a multiplex bead-based flow cytometry assay. Each sample was assessed in triplicate to ensure technical reproducibility. Raw fluorescence intensities were first corrected for background using PBS controls and then normalized to the average signal of the tetraspanins CD9, CD63, and CD81. Results are expressed as mean ± SEM. Surface markers showing statistically significant differences among the groups (CD44, CD326, MCSp) are highlighted, and individual patient data are displayed. Statistical analysis was performed using the Kruskal-Wallis test followed by Dunn's multiple comparisons; p-values below 0.05 were considered statistically significant.*

A

Biological functions	Surface markers
EV markers	CD9, CD63, CD81
Cancer-associated/Stemness marker	CD24, CD326, ROR1, MCSp
Immune-associated	CD2, CD4, CD8, CD11c, CD14, CD40, CD45, HLA-ABC, HLA-RDRDPQ
Adhesion and migration markers	CD29, CD49e, CD44, CD146
Platelet-associated	CD41b, CD42a, CD62p
Angiogenesis and endothelial markers	CD31, CD105

B

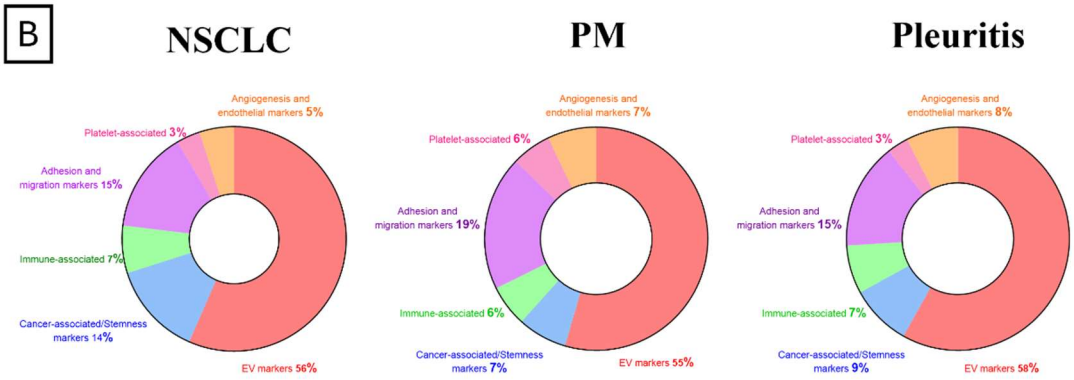

Figure 5.15. Functional classification and relative distribution of EV surface marker signals. A) The 25 analyzed surface markers were categorized into six groups according to their biological functions and cellular origin; B) Donut plots represent the proportional contribution of each group to the overall EV surface marker profile. Group-level signals were calculated as the normalized mean APC intensity of all markers within each functional category.

5.2.2. CD326 is elevated in malignant pleural effusions, while CD4 and CD44 are increased in epithelioid PM compared to non-epithelioid subtypes

The patient cohort was further stratified based on the **presence or absence of malignancy** in the pleural space. The two groups exhibited comparable particle size distributions and total protein concentrations (Figure 5.16.A). Among all investigated surface markers (Sup Figure 6), only **CD326** was significantly elevated in the malignant group compared to the non-malignant group (Figure 5.16D). Subgroup analysis of NSCLC and **PM** cases based on histological **subtypes** was also performed. No significant differences were observed between adenocarcinoma (ADC) and squamous cell carcinoma (SCC) patients in any of the examined EV-related parameters (Figure 5.16B, Sup Figure 7). However, within the PM cohort, patients with the epithelioid subtype exhibited significantly higher levels of **CD4 and CD44** compared to those with non-epithelioid PM (Figure 5.16E, Sup Figure 8).

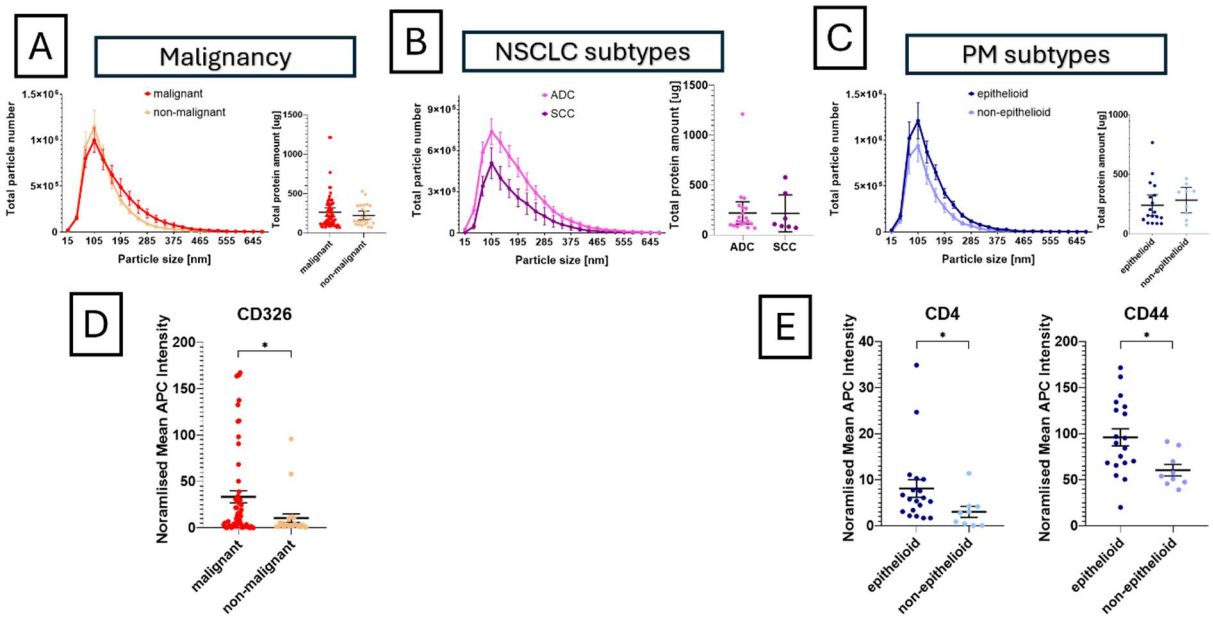

Figure 5.16. Characterization of EVs across malignant status and NSCLC/PM subtypes. *NTA was used to assess particle size distribution, presented as mean ± SEM. Total protein content was quantified using the Qubit protein assay and is shown as mean ± 95% confidence interval. A) Patient stratification based on the presence of malignancy in the pleural space (malignant vs. non-malignant); B) NSCLC subtypes: adenocarcinoma (ADC) and squamous cell carcinoma (SCC); C) PM subtypes: epithelioid and non-epithelioid. D) Surface markers showing statistically significant expression differences between malignant and non-malignant groups (mean ± SEM); E) Differential surface marker expression between epithelioid and non-epithelioid PM subtypes (mean ± SEM); Statistical analysis was performed using the Mann-Whitney U test, p-values below 0.05 were considered statistically significant.*

5.2.3. Machine-learning enhance the diagnostic potential of extracellular vesicles surface marker profiles in the 'intial' classification

Following the characterization of individual surface marker expression patterns across patient groups – as defined by the initial pathological diagnoses – a machine learning algorithm (which was developed by Ádám Rák) was employed to classify patients into their respective diagnostic categories (NSCLC, PM, and pleuritis). Figure 5.17 presents a heatmap illustrating the **classification outcomes** of our machine learning model, indicating whether each patient is categorized as having NSCLC, PM, or pleuritis. This visualization underscores the model's capacity to differentiate among these conditions based on the unique extracellular vesicle surface marker profiles derived from each patient's pleural effusion sample. Our machine learning model successfully identified approximately half of the NSCLC patients and the majority of those with PM, however, its accuracy in detecting patients with pleuritis was comparatively lower. **Hit-to-miss ratios** were calculated across the groups, a classification outcome was deemed a 'hit' if the algorithm assigned the highest probability to the correct patient group over all other groups (Figure 5.17). However, statistical analysis of the hit-to-miss ratios across these groups revealed no significant differences.

	Patient	Predicted		
		NSCLC	PM	Pleuritis
NSCLC	P1	0,98	0,02	0,00
	P11	0,98	0,00	0,02
	P3	0,98	0,02	0,00
	P22	0,96	0,01	0,03
	P26	0,94	0,04	0,02
	P7	0,91	0,03	0,06
	P9	0,90	0,00	0,10
	P25	0,90	0,06	0,04
	P29	0,81	0,00	0,19
	P4	0,76	0,00	0,24
	P17	0,72	0,00	0,28
	P12	0,66	0,01	0,33
	P24	0,65	0,00	0,35
	P14	0,64	0,31	0,05
	P28	0,51	0,05	0,43
	P10	0,39	0,00	0,61
	P2	0,34	0,65	0,00
	P8	0,34	0,59	0,07
	P6	0,32	0,00	0,68
	P16	0,28	0,00	0,71
	P19	0,24	0,47	0,29
	P18	0,23	0,01	0,77
	P20	0,20	0,74	0,06
	P23	0,13	0,23	0,65
	P27	0,07	0,01	0,92
	P21	0,07	0,00	0,93
	P13	0,04	0,16	0,80
	P5	0,01	0,00	0,99
	P15	0,00	0,29	0,71

	Patient	Predicted		
		NSCLC	PM	Pleuritis
PM	P44	0,00	0,99	0,00
	P47	0,01	0,99	0,00
	P35	0,01	0,99	0,00
	P42	0,02	0,98	0,00
	P49	0,01	0,98	0,01
	P39	0,00	0,97	0,03
	P38	0,00	0,96	0,04
	P36	0,02	0,94	0,05
	P48	0,04	0,93	0,04
	P46	0,01	0,92	0,07
	P57	0,02	0,90	0,08
	P43	0,09	0,86	0,05
	P41	0,01	0,79	0,19
	P52	0,21	0,76	0,03
	P55	0,09	0,73	0,18
	P50	0,01	0,60	0,39
	P54	0,00	0,58	0,42
	P37	0,35	0,57	0,07
	P45	0,27	0,42	0,30
	P56	0,02	0,27	0,70
	P53	0,46	0,21	0,33
	P32	0,08	0,04	0,88
	P34	0,50	0,03	0,47
	P33	0,02	0,03	0,95
	P40	0,00	0,02	0,98
	P30	0,48	0,01	0,51
	P31	0,01	0,00	0,99
	P51	0,84	0,00	0,16

	Patient	Predicted		
		NSCLC	PM	Pleuritis
Pleuritis	P82	0,03	0,01	0,96
	P78	0,03	0,02	0,95
	P70	0,13	0,00	0,87
	P59	0,15	0,01	0,84
	P65	0,18	0,01	0,81
	P77	0,06	0,19	0,75
	P81	0,28	0,00	0,72
	P72	0,37	0,01	0,62
	P74	0,29	0,18	0,54
	P80	0,01	0,51	0,48
	P58	0,54	0,00	0,46
	P73	0,06	0,52	0,42
	P75	0,57	0,03	0,40
	P79	0,11	0,57	0,32
	P69	0,42	0,38	0,21
	P61	0,00	0,82	0,17
	P76	0,87	0,00	0,13
	P64	0,05	0,87	0,08
	P71	0,03	0,89	0,08
	P66	0,74	0,20	0,06
	P63	0,96	0,00	0,04
	P67	0,00	0,98	0,02
	P62	0,73	0,25	0,01
	P60	0,98	0,01	0,01
	P68	1,00	0,00	0,00

Figure 5.17. Heatmap representation of machine learning-based diagnostic predictions. *The figure displays the classification probabilities assigned to each patient, indicating the likelihood of assignment to each diagnostic category: NSCLC, PM and pleuritis.*

5.2.4. Different surface marker expression changes in the alternatively classified patient groups

Given that certain patients were classified with a high probability into alternative groups, I re-evaluated the grouping strategy, incorporating patients' additional malignancies and the variabilities of the malignancies pleural involvement to refine classification accuracy. In addition to the initial classification, four alternative classification methods (see detailed in Methods section 4.7) were developed based on patients' clinical histories.

Among the various patient groups, no statistically significant differences were detected in the EV **size-distribution curves** (Sup Figure 9). However, within the 'tumor focused' classification, EVs from patients with cancer exhibited broader size ranges, with interquartile ranges (IQR) of 105-225 nm, whereas those from patients with PM or pleuritis showed narrower distributions (IQR: 75-165 nm) (Sup Figure 9A). Similarly, EVs derived from individuals with NSCLC or pleura involved cancer displayed increased size profiles (IQR: 105-255 nm) compared to other groups (IQR: 75-165 nm) (Sup Figure 9B-D). Total protein concentrations were comparable across all cohorts (Sup Figure 9A-D).

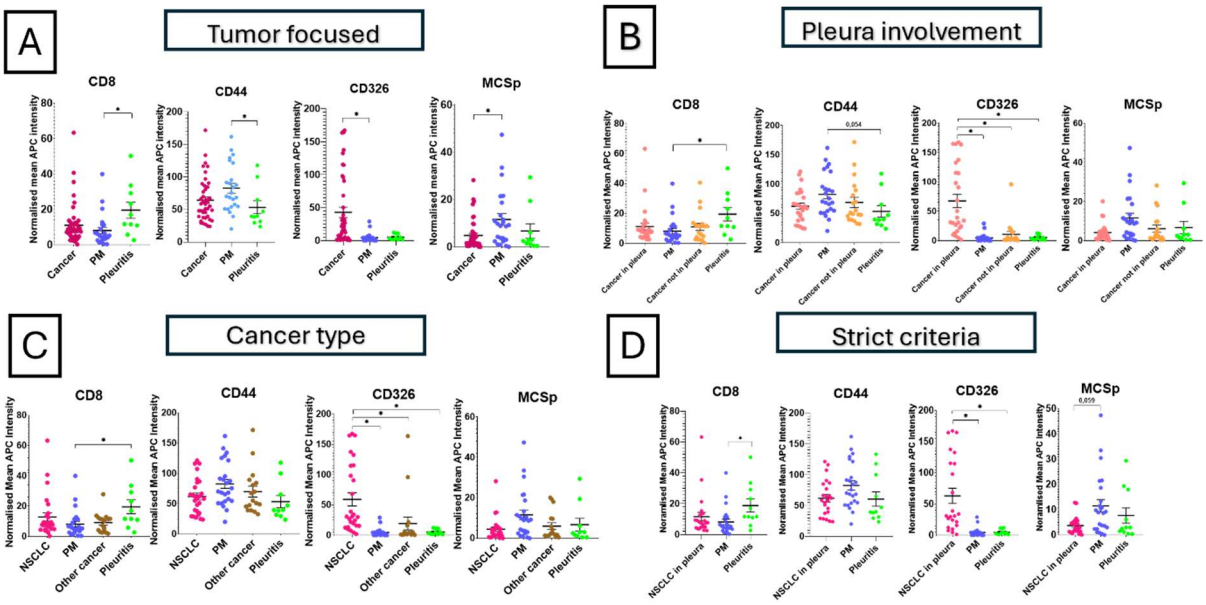

Figure 5.18. Differential surface marker expression on extracellular vesicles across alternative classification strategies*. Expression levels (mean ± SEM) of CD8, CD44, CD326, and MCSp were quantified using multiplex bead-based flow cytometry. Statistical analysis was performed using the Kruskal-Wallis test followed by Dunn's multiple comparisons; p-values below 0.05 were considered statistically significant. A) 'Tumor focused' classification; B) 'Pleura involvement' classification; C) 'Cancer type' classification; D) 'Strict criteria' classification .*

Subsequently, **surface marker expression** patterns were assessed across the alternative classification schemes (Sup Figure 10-13). When comparing these to the initial diagnostic grouping, some differences in expression trends were observed. **CD8** levels were consistently higher in pleuritis patients compared to those with PM across all alternative classification methods (Figure 5.18A-D). A significant difference in **CD44** expression emerged only within the 'tumor-focused' classification, distinguishing PM from pleuritis (Figure 5.18A), while a similar, though not statistically significant, trend was noted in the 'pleural involvement' classification (Figure 5.18B, p = 0.054). **CD326** expression was markedly elevated in groups classified as cancer, pleura-involved cancer, NSCLC, and pleura-involved NSCLC, relative to all other categories (Figure 5.18A-D). In contrast, **MCSp** expression was significantly increased only in the broader cancer group compared to PM patients without cancer (Figure 5.18A); this trend was also seen in the 'strict criteria' classification (Figure 5.18D), albeit without reaching statistical significance (p = 0.059).

5.2.5. Machine learning performance is highest under strict classification criteria

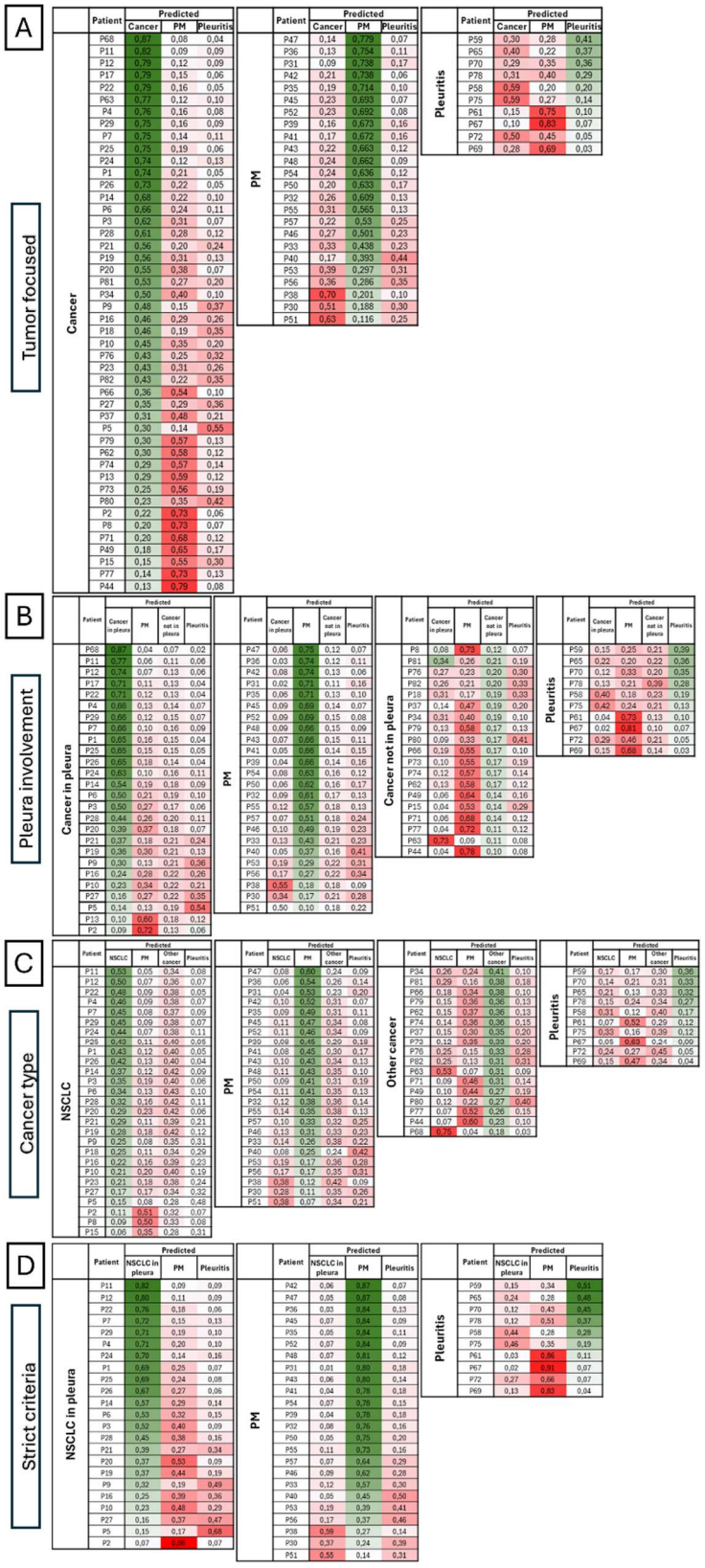

Figure 5.19. Heatmap representation of machine learning-based diagnostic predictions. *The figure displays the classification probabilities assigned to each patient, indicating the likelihood of assignment to each diagnostic category. A) 'Tumor focused' classification; B) 'Pleura involvement' classification; C) 'Cancer type' classification; D) 'Strict criteria' classification.*

After analyzing individual surface marker expressions, the machine learning algorithm was employed to assess the classification performance of each diagnostic grouping. Classification probabilities, reflecting the likelihood of each patient being assigned to a specific diagnostic category, are shown in Figure 5.19. All four heatmaps are displayed together to facilitate comparison across classification strategies.

To determine the diagnostic accuracy of each method, hit-to-miss ratios were calculated based on the heatmap data (Figure 5.19). In the 'tumor-focused' classification, cancer ($p = 0.0093$, corrected) and PM ($p = 0.0045$, corrected) cases were more reliably classified than pleuritis cases (Figure 5.19A). Similarly, in the 'pleura involvement' classification, patients with pleura-involved cancers ($p = 0.0306$, corrected) and PM ($p = 0.0366$, corrected) were more frequently identified correctly than those with pleuritis (Figure 5.19B). Within the 'strict criteria', PM was again classified more accurately than pleuritis ($p = 0.0246$, corrected, Figure 5.19D).

When comparing the overall effectiveness of the different classification methods, only the 'tumor-focused' strategy outperformed the 'cancer type' classification in terms of hit-to-miss ratio ($p = 0.0227$, adjusted) (Figure 5.19A-B).

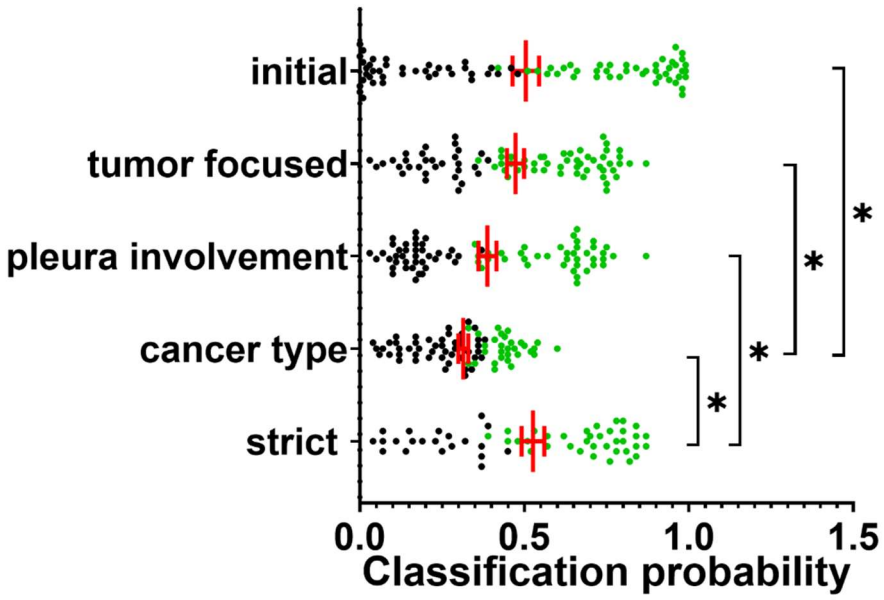

Figure 5.20. Evaluation of classification confidence across diagnostic strategies using machine learning. *The plot displays the average predicted probabilities (mean ± SEM) that the model assigned to each patient's correct diagnosis under the different classification schemes. Green dots indicate correctly classified cases, while black dots denote misclassifications. Statistical significance was determined using the Kruskal-Wallis test followed by Dunn's multiple comparison test, setting the significance level at 0.05.*

To further assess model performance, the predicted probabilities assigned to each patient's true diagnostic category were visualized as mean values with SEM (Figure 5.20). This representation allowed for the evaluation of classifier certainty across the different diagnostic strategies. Higher densities of predictions near the upper probability range reflect greater classifier confidence, whereas lower or more dispersed values suggest weaker classification strength. Among the strategies, the 'cancer type' classification showed the poorest performance, with lower probabilities assigned to the correct diagnoses when compared to the 'initial,' 'tumor-focused,' and 'strict criteria' groupings. In contrast, the 'strict criteria' classification surpassed the 'pleura involvement' method in terms of classifier confidence. Furthermore, the relatively low diagnostic confidence observed under the initial classification improved substantially under the 'strict criteria' approach.

To expand the comparison between the ‘initial’ and ‘strict criteria’ classification approaches, receiver operating characteristic (ROC) curves and corresponding AUC values were computed (Figure 5.21.). Narrowing the cohort by removing patients with unrelated malignancies, whose EV profiles could confound NSCLC- and PM-specific signals, resulted in improved classification accuracy. Specifically, AUC values increased from 0.75 to 0.81 for NSCLC and from 0.76 to 0.95 for PM (Figure 5.21). In contrast, due to the substantially smaller pleuritis subgroup, the stricter criteria did not lead to enhanced performance in this group.

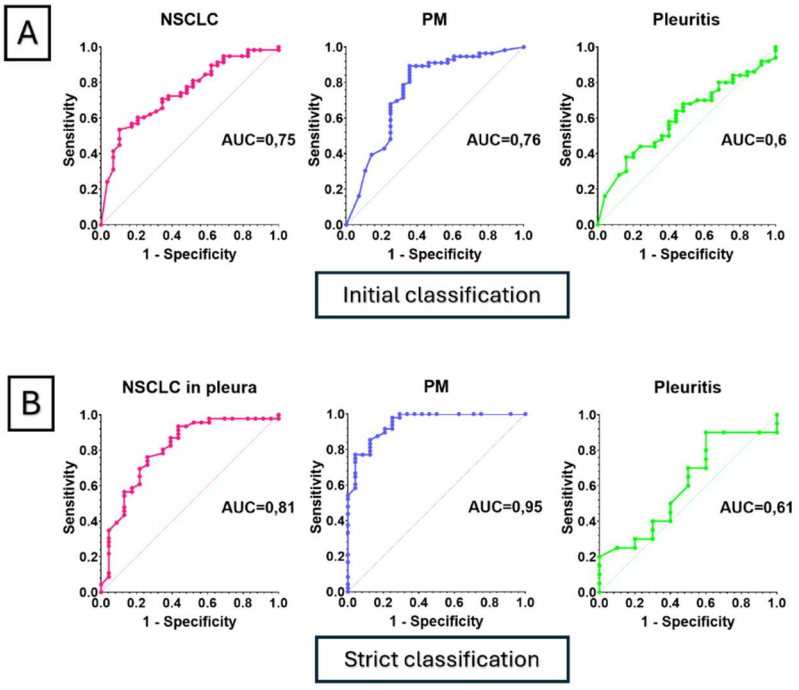

Figure 5.21. Diagnostic accuracy assessment of the ‘initial’ versus ‘strict criteria’ classification strategies*. A) ROC curves and AUC values for NSCLC, PM, and pleuritis patients using the ‘initial’ classification; B) ROC curves and AUC values for NSCLC confined in pleura, PM, and pleuritis patients under the ‘strict criteria’ classification.*

6. Discussion

During my PhD, working in the Translational Oncology Laboratory, I investigated the role of extracellular vesicles (EVs) across distinct aspects of cancer. Accordingly, the discussion is structured in two main sections: (i) EVs as mediators of cancer progression and drug resistance, and (ii) EVs as potential biomarkers in thoracic malignancies.

6.1. EVs as mediators of cancer progression and drug resistance

EVs are increasingly recognized as key facilitators of intercellular communication, exerting influence both in the tumor microenvironment and systemically [1]. In this study, I sought to investigate the potential role of EVs in modulating cell viability and migration. Since metastasis remains the leading cause of mortality in melanoma [111], clarifying how EVs influence migratory behavior, the early steps of metastasis formation has particular relevance.

This study examined the functional impact of EVs derived from melanoma cell lines representing various tumor stages and exhibiting differential sensitivity to BRAF (vemurafenib, dabrafenib) and MEK (trametinib) inhibitors. EVs were isolated from five syngeneic melanoma cell line pairs and applied both EV on both cells. Subsequent analyses focused on **EV characterization**, as well as their effects on cell proliferation, sphere growth and migration. The properties of the ultracentrifugation-isolated EVs were consistent with those reported for supernatant-derived vesicles in previous studies [2], [295], [296]. However, prominent differences were not observed between EVs originating from less or more aggressive cell lines.

After confirming the successful isolation of EVs, I observed that their influence on cell proliferation and sphere formation was limited, whereas their impact on **cell migration** was more substantial. In almost all tested cell lines, EV-exposure led to increased MSD and TTD values; however, a statistically significant enhancement was only detected in the MSD measurements for the Mel Pt-3 pre and Mel Pt-4 post lines. Interestingly, EVs derived from highly aggressive cells did not uniformly produce stronger migratory effects. Considering the pivotal role of cell motility in metastatic initiation, these findings suggest that EVs may contribute more directly to metastasis than to primary tumor expansion. This aligns with previous reports, such as those in oral squamous carcinoma models, where cancer-associated fibroblast-derived EVs preferentially stimulated cell migration over proliferation [302]. Similarly, in our study, while EVs from differently aggressive melanoma lines had minimal influence on proliferation, vesicles from the more invasive lines tended to enhance migratory behavior in recipient cells [303].

To the best of my knowledge, this is the first study to investigate **the role of EVs in single-cell migration**. Previous studies have predominantly assessed migration using transwell [303]-[308]

or wound healing assays [304], [309]-[313]. However, these traditional methods are relatively complex and often confound migration with other processes such as proliferation and invasion, making it difficult to isolate the specific effects on migratory behavior [314]. In contrast, single-cell tracking, as applied in this study, offers a more direct and refined method for assessing the influence of treatments on multi-directional migratory behavior [315]. This approach allows for the calculation of parameters such as MSD, which is particularly sensitive to changes in directionality. It is important to note that if a treatment primarily affects directionality rather than speed of migration, this may be more evident in MSD than in velocity measurements. Additionally, the directional constraints inherent to scratch assays – where cells predominantly migrate toward the induced gap – can obscure such effects, making it harder to detect changes in migration patterns that involve alterations in directionality.

Targeted inhibition of BRAF (e.g., with vemurafenib, dabrafenib or encorafenib) is a cornerstone in the treatment of BRAF-mutant melanoma. Although these therapies initially yield strong clinical responses, many patients eventually develop resistance, often accompanied by accelerated metastatic progression. Among the various mechanisms implicated in this acquired resistance, EVs have emerged as important mediators of intercellular communication that may facilitate therapy escape.

Given my earlier observations that EVs enhance cell migration, I hypothesized that they might also **modulate the efficacy of BRAF inhibition**. The results revealed that EVs can diminish the anti-migratory effects of BRAF inhibitors, suggesting a role in the development of resistance. Notably, EVs derived from more resistant melanoma cells were particularly more effective at overriding the inhibitory impact of treatment, indicating that EV content could be associated with the resistance profile of the donor cell. These findings are supported by prior studies demonstrating that EVs from PLX-4720-resistant melanoma cells can transfer resistance to otherwise sensitive cells through the delivery of PDGFRβ [167]. Similarly, vemurafenib-resistant cells were shown to secrete EVs carrying a truncated ALK isoform, which enhanced proliferation in recipient cells during treatment [168]. Moreover, BRAF inhibitor treatment modifies the miRNA content of melanoma cell-derived EVs, particularly increasing levels of miR-211-5p, a resistance-associated miRNA [166]. Also, BRAF splice variants have been detected in EVs from both resistant cell lines and plasma of relapsed patients, highlighting the clinical relevance of EV cargo profiling [316].

As BRAF inhibitors are frequently administered in combination with **MEK inhibitors** in clinical settings, therefore, I extended my investigation to assess whether this dual treatment could counteract the migration-enhancing effects of EVs. To date, possibly none of the studies have

investigated EV-mediated mechanisms in the context of combined BRAF and MEK inhibitor resistance, highlighting the novelty and importance of this approach.

When cells – originally derived from patients treated with vemurafenib – were exposed to trametinib (MEKi) alone or in combination with dabrafenib (BRAFi), EV treatment did not induce the same pro-migratory response observed under BRAF inhibitor monotherapy. However, an important limitation of this model is that these cell lines had only been exposed to BRAF inhibition and lacked prior exposure to MEK inhibitors, thus potentially limiting the relevance of the findings to actual dual-therapy resistance. To address this, I aimed to establish a more representative system by **generating cell lines** that had been subjected to prolonged exposure to both encorafenib (BRAFi) and binimetinib (MEKi), to model resistance to combination therapy. The resistant cell line exhibited not only altered drug sensitivity compared to its parental counterpart but also displayed several phenotypic changes. A reduction in both proliferation and migratory capacity was observed, accompanied by a more elongated cell shape – suggestive of epithelial-to-mesenchymal transition (EMT) [301]. Similar morphological alterations were reported by Patel et al. following prolonged exposure to encorafenib-binimetinib, although their resistant clones showed enhanced invasive behavior [301]. It is also generally recognized that drug-resistant cells tend to release higher amounts of extracellular vesicles than their sensitive counterparts [317] – a trend that was also evident in the resistant cell line developed in this study. In experiments using the established resistant cell line, extracellular vesicles were unable to counteract the effects of BRAF inhibitors when both were administered simultaneously. However, when cells were pre-exposed to EVs prior to drug treatment, the inhibitory impact of the therapy was noticeably reduced. These findings suggest that the influence of EVs is time-dependent and likely involves broader, EV-mediated signaling alterations rather than simply binding or encapsulating the drug molecules.

These findings reinforce earlier evidence that extracellular vesicles play a pivotal role in melanoma progression, with a more pronounced influence on metastatic dissemination than on primary tumor growth and further underline their involvement in resistance to BRAF-targeted therapies.

6.2 EVs as potential biomarkers in thoracic malignancies

After gaining insight into the roles of EVs in cancer progression, I sought to explore their potential as diagnostic tools by isolating them from patient-derived body fluids. Liquid biopsy approaches offer a minimally invasive alternative to traditional biopsies and are capable of capturing tumor heterogeneity more comprehensively. They also hold promise for enabling earlier detection and real-time monitoring of disease progression [191]. For this purpose, I established a **patient cohort** comprising individuals with non-small cell lung cancer (NSCLC), pleural mesothelioma (PM), and pleuritis. Given that **pleural effusion** is a common clinical manifestation in these diseases – and is routinely collected in substantial volumes to alleviate symptoms – this fluid was selected for EV analysis [206]. EVs were successfully isolated from pleural effusions using size-exclusion chromatography and concentrated through ultrafiltration. NTA was employed to determine particle size distribution, which yielded results consistent with prior literature [318], [319]. Although no statistically significant differences were found across patient groups, NSCLC samples tended to exhibit a broader size distribution, hinting at greater vesicle heterogeneity. A similar phenomenon was observed in ascites-derived EVs from ovarian carcinoma patients, where greater particle sizes were noted compared to those from individuals with benign ovarian conditions [320].

The **surface marker profile** of isolated EVs was characterized using a multiplex bead-based assay. The detection of a wide array of markers indicated a mixed cellular origin of EVs in pleural fluid, underscoring active communication within this microenvironment. Marker grouping based on biological function did not reveal pronounced differences among diagnostic categories. Notably, platelet-derived EV levels were relatively low in these isolates, contrasting with plasma-derived EVs, where platelet-associated markers are typically dominant.

In the initial pathology-based classification, **CD44** levels were elevated in PM samples compared to NSCLC and pleuritis. CD44, a hyaluronic acid receptor implicated in cell proliferation and invasion [321], [322], has long been studied in PM [323], [324]. For instance, Porcel et al. [325] demonstrated that soluble CD44 in pleural fluid could help distinguish PM from other malignancies. Additionally, earlier findings indicate subtype-specific expression of CD44, with epithelioid PM exhibiting higher levels than non-epithelioid variants [321] – a pattern also evident in our cohort. These results support the biomarker potential of CD44 for both diagnosis and subtype differentiation in PM. Furthermore, the immune-related **CD4** levels were elevated in EVs from epithelioid PM, consistent with previous reports that this subtype exhibits increased peritumoral $CD4^+$ T cell infiltration [326]. This may reflect a more active immune environment, which could help explain the generally better overall survival associated with epithelioid PM

compared to non-epithelioid subtypes.[327]. Additionally, higher **MCSp** (melanoma chondroitin sulfate proteoglycan) expression in PM samples aligns with earlier studies linking this marker to mesothelioma [328]-[330]. In contrast, **CD326** (EpCAM), a well-established epithelial tumor marker [331]-[335], was predominantly expressed in NSCLC-derived EVs, reflecting the epithelial origin of these tumors.

Machine learning-assisted analysis of EV profiles could effectively distinguish between cancerous and non-cancerous conditions in earlier studies [336]. Therefore, to better interpret complex EV marker data and improve diagnostic performance, I applied machine learning algorithm, which was developed by Ádám Rák to identify marker patterns predictive of disease status. In the initial classification most of the patients were classified correctly, however certain patients were categorized into other groups with high probability. Upon reviewing clinical data, I found that these missclassified patients have secondary malignancies or differences in pleural involvement. As a result, four alternative classification schemes were introduced: three incorporated nearly all patients while accounting for their broader clinical profiles ("tumor-focused," "pleura involvement," and "cancer type"), and one employed strict criteria, excluding ambiguous cases to avoid potential bias. Across these classifications, CD326 remained elevated in all cancer patients, in cancers involving the pleura and in NSCLC cases. CD44 and MCSp differences were most notable in the 'tumor-focused' classification. Importantly, CD8 levels were consistently higher in pleuritis across all alternative classifications. This marker, commonly associated with cytotoxic T cells, has previously been found enriched in benign conditions compared to malignant pleural diseases [289], supporting its potential role in distinguishing inflammatory from neoplastic processes. When applying the algorithm to these refined classifications, the algorithm revealed differential diagnostic potential. Specifically, in the 'strict criteria' grouping – focusing on primary NSCLC with pleural involvement and PM – ROC AUC values reached 0.81 for NSCLC and 0.95 for PM, suggesting robust discriminative capacity.

In conclusion, these findings underscore the utility of EV-based liquid biopsies in pleural effusions as a promising avenue for differentiating between malignant and benign conditions. While individual EV markers like CD44, CD326, and CD8 show diagnostic relevance, the integration of machine learning is key for handling the complexity of EV data. The classification frameworks explored here highlight the importance of flexible and detailed patient stratification strategies in translational biomarker research. Future studies involving larger, clinically diverse cohorts will be essential to validate these early findings and refine diagnostic models for broader clinical application.

7. Thesis points

I. Melanoma cell-derived extracellular vesicles (EVs) promote cell migration more effectively than proliferation or sphere formation.

Syngeneic melanoma cell line pairs were used in the study, and EVs were successfully produced and isolated from all lines. The protein and lipid content of the EV isolates did not show major differences across cell lines with varying malignancy. EV treatment altered proliferation in some cases, they maintained sphere formation at baseline level, while their overall effect on migration was more pronounced, with a broader trend of enhanced motility observed across cell lines. A notable strength of this work is the analysis of EV-mediated migration at the single-cell level, which has not been previously addressed.

II. EVs originating from drug-resistant melanoma cell lines contribute to resistance transmission.

a. EV-mediated promotion of migration persists under BRAF inhibitor treatment

The baseline sensitivity of cell lines to vemurafenib and dabrafenib was assessed, and drug concentrations resulting in ~50% inhibition were selected for further analysis. EVs derived from more resistant cell lines were able to counteract the migration-inhibitory effects of BRAF inhibitors, indicating that EVs can maintain pro-migratory signals under targeted therapy. Furthermore, resistant cells-derived EVs carry distinct information compared to the ones from the sensitive cells and this leads to resistance transfer.

b. Dual BRAF-MEK inhibition remains largely unaffected by EVs from resistant cells

Sensitivity to dual BRAF-MEK inhibition was evaluated, and combination index calculations confirmed a synergistic interaction between the inhibitors. The inhibitory effects of either MEK inhibition alone or combined BRAF-MEK inhibition remained effective when EVs were administered simultaneously. However, slight modulation of inhibition was observed when cells were preconditioned with EVs, suggesting a time-dependent and subtle influence in this setting.

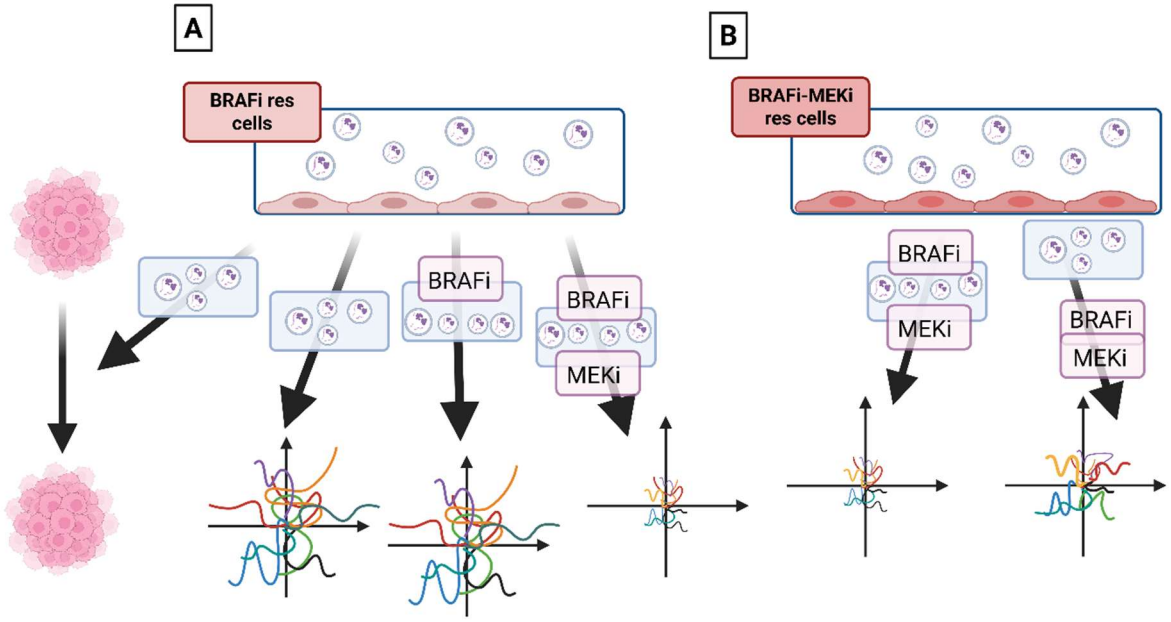

Figure 7.1 Overview of EV-mediated effects in the context of melanoma progression and targeted therapy resistance. *A) EVs promote cell migration rather than proliferation and sphere growth. Resistant cells-derived EVs retain their ability to promote cell migration under BRAF inhibitor treatment (vemurafenib, dabrafenib), but show limited effect when BRAF and MEK inhibitors are combined (dabrafenib + trametinib). B) In the established BRAFi-MEKi resistant cell lines, only EV preconditioning partially counteracted the migration-inhibitory effects of combined encorafenib-binimetinib therapy.*

III. Pleural effusion-derived EVs from NSCLC, pleural mesothelioma (PM), and pleuritis patients exhibit distinct surface marker profiles.

a. CD4, CD8, CD44, CD326, and MCSp can differentiate between disease groups.

EVs were successfully isolated from pleural effusion samples, with no significant differences observed in particle size distribution or protein content across the patient groups. Surface marker expression was assessed using a multiplex bead-based assay, revealing that the EV marker profile in pleural effusions differs markedly from plasma-derived EVs, and reflect active EV-based communication in the tumor microenvironment. CD44 and MCSp emerged as markers associated with PM, CD8 was linked to pleuritis, and CD326 was indicative of NSCLC and malignancy. Additionally, CD4 and CD44 were capable of distinguishing between PM subtypes.

b. Machine learning analysis of the EV surface markers able to highlight classification inconsistencies primarily linked to patients with secondary malignancies; excluding these cases led to the highest accuracy.

Machine-learning algorithm was used to classify patients based on their surface maker expression pattern and most of the patients were classified correctly. Furthermore, the

algorithm was able to point out some errors in our classification scheme. Therefore, several alternative classifications were created based on the patients clinical history: 'initial' (based on cytological diagnosis), 'tumor-focused' (based on the presence of any tumor in the body), 'pleural involvement' (based on whether the pleura was affected), 'cancer type' (categorizing NSCLC, PM, and other cancers separately), and 'strict criteria' (excluding patients with secondary malignancies). Among these, the strict criteria approach yielded the most accurate classification performance for distinguishing between NSCLC and PM patients.

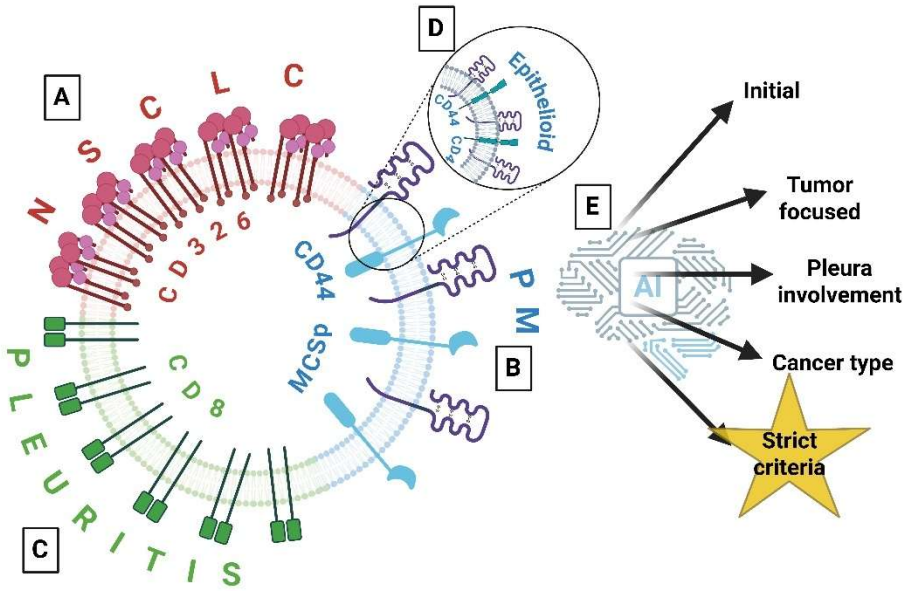

***Figure 7.2. Summary of pleural effusion-derived EV surface markers and their diagnostic potential**. A) CD326 (EpCAM) is highly expressed in EVs from NSCLC patients; B) CD44 and MCSp is elevated in PM; C) CD8 a pleuritis-associated marker; D) CD4 and CD44 is overexpressed in epithelioid PM compared to non-epithelioid; E) Among several classification strategies, the 'strict criteria' approach yielded the most accurate group separation in machine learning analysis*

8. List of publications

Journal publications:

Ekström K, Riaz N, Larsson K, Németh A, Crescitelli R, Linderholm B, Olofsson Bagge R. Plasma extracellular vesicles reflect response and prognosis in patients with breast cancer undergoing neoadjuvant treatment. Breast Cancer Res (2026). doi:10.1186/s13058-025-02209-0

Németh A, Bányai GL, Dobos NK, Kós T, Gaál A, Varga Z, Buzás EI, Khamari D, Dank M, Takács I, Szász AM, Garay T. Extracellular vesicles promote migration despite BRAF inhibitor treatment in malignant melanoma cells. Cell Commun Signal. 2024 May 22;22(1):282. doi: 10.1186/s12964-024-01660-4. PMID: 38778340; PMCID: PMC11110207. – Best Hungarian EV paper of 2024 (Awarded at the 2024 HSEV conference)

Marchelek EM, Nemeth A, Mohak S, Varga K, Lukacsi S, Fabian Z. Dendritic Cell Therapy in Immuno-Oncology: A Potentially Key Component of Anti-Cancer Immunotherapies. Cancers. 2026; 18(1):123. doi:10.3390/cancers18010123

Németh A, Bányai GL, Andrészek M, Dobos NK, Köllőd C, Garay T. Comparison of in vitro migration assays evaluating nintedanib's migration inhibitory effects on melanoma cells. Sci Rep. 2025 Nov 28;15(1):42599. doi: 10.1038/s41598-025-26571-3. PMID: 41315550; PMCID: PMC126633

Kocsis D, Sztankovics D, Józsa L, Németh A, Garay T, Naszlady MB, Lengyel M, Vecsernyés M, Antal I, Sebestyén A, Erdő F. In Vitro Functional and Structural Evaluation of Low-Complexity Artificial Human Epidermis for 3D Tissue Engineering. Bioengineering (Basel). 2025 Feb 24;12(3):230. doi: 10.3390/bioengineering12030230. PMID: 40150694; PMCID: PMC11939566.

Welsh JA, Goberdhan DCI, O'Driscoll L, Buzas EI, Blenkiron C, Bussolati B, Cai H, Di Vizio D, Driedonks TAP, Erdbrügger U, Falcon-Perez JM, Fu QL, Hill AF, Lenassi M, Lim SK, Mahoney MG, Mohanty S, Möller A, Nieuwland R, Ochiya T, Sahoo S, Torrecilhas AC, Zheng L, Zijlstra A, Abuelreich S, Bagabas R, Bergese P, Bridges EM, Brucale M, Burger D, Carney RP, Cocucci E, Crescitelli R, Hanser E, Harris AL, Haughey NJ, Hendrix A, Ivanov AR, Jovanovic-Talisman T, Kruh-Garcia NA, Ku'ulei-Lyn Faustino V, Kyburz D, Lässer C, Lennon KM, Lötvall J, Maddox AL, Martens-Uzunova ES, Mizenko RR, Newman LA, Ridolfi A, Rohde E, Rojalin T, Rowland A, Saftics A, Sandau US, Saugstad JA, Shekari F, Swift S, Ter-Ovanesyan D, Tosar JP, Useckaite Z, Valle F, Varga Z, van der Pol E, van Herwijnen MJC, Wauben MHM, Wehman AM, Williams S, Zendrini A, Zimmerman AJ; MISEV Consortium; Théry C, Witwer KW. Minimal information for studies of extracellular vesicles (MISEV2023): From basic to advanced approaches. J Extracell Vesicles. 2024 Feb;13(2):e12404. doi: 10.1002/jev2.12404. Erratum in: J Extracell Vesicles. 2024 May;13(5):e12451. doi: 10.1002/jev2.12451. PMID: 38326288; PMCID: PMC10850029.

Wisniewski É, Czárán D, Kovács F, Bahurek E, Németh A, Sasvári P, Szanda G, Pettkó-Szandtner A, Klement E, Ligeti E, Csépányi-Kömi R. A novel BRET-Based GAP assay reveals phosphorylation-dependent regulation of the RAC-specific GTPase activating protein ARHGAP25. FASEB J. 2022 Nov;36(11):e22584. doi: 10.1096/fj.202200689R. PMID: 36190314.

Baranyi M, Rittler D, Molnár E, Shirasawa S, Jalsovszky I, Varga IK, Hegedűs L, Németh A, Dank M, Aigner C, Tóvári J, Tímár J, Hegedűs B, Garay T. Next Generation Lipophilic Bisphosphonate Shows Antitumor Effect in Colorectal Cancer In Vitro and In Vivo. Pathol Oncol Res. 2020 Jul;26(3):1957-1969. doi: 10.1007/s12253-019-00789-9. Epub 2020 Jan 4. PMID: 31902117.

Submitted journal publications:

Németh A, Ekström K, Crescitelli R, Bagge RO, Bányai GL, Rák Á, Cserey Gy, Bölükbas S, Visnovitz T, Hegedűs B, Garay, T Machine learning-enhanced analysis of extracellular vesicle profiles in pleural effusions for cancer diagnosis – submitted to MedComm journal

Németh A., Simon A, Bányai GL , Lenzinger D, Garay T Acquired resistance to MAPK inhibition and the contribution of extracellular vesicles – submitted to Cancer Reports

Conference talk:

Németh A, Bányai GL, Dobos NK, Kós T, Gaál A, Varga Z, Buzás EI, Khamari D, Dank M, Takács I, Szász AM, Garay T; Extracellular vesicles promote migration despite BRAF inhibitor treatment; *2nd MOVE symposium 2024 Belgrade*

Conference publications:

Németh A, Ekström K, Crescitelli R, Bagge RO, Bányai GL, Rák Á, Cserey Gy, Bölükbas S, Visnovitz T, Hegedűs B, Garay, T; Diagnostic potential of pleural fluid-derived extracellular vesicles in differentiating pleural-associated diseases using machine learning; *ISEV2025 Vienna*

Bányai GL, Merényi A, Szabó A, Németh A, Gaál A, Pongor Cs, Garay T; Utilizing microfluidic techniques to differentiate cancer patient samples based on extracellular vesicle profiles; *ISEV2025 Vienna*

Németh A; Extracellular vesicles promote migration despite BRAF inhibitor treatment; *Phd Proceedings Annual Issues of the Doctoral School Faculty of Information Technology and Bionics 2024*

Németh A; The role of extracellular vesicles in melanoma progression; *Phd Proceedings Annual Issues of the Doctoral School Faculty of Information Technology and Bionics 2023*

Németh A, Kós T, Bányai GL, Gaál A, Varga Z, Dank M, Takács I, Szász AM, Garay T; Effects of extracellular vesicles on vemurafenib sensitivity in syngeneic melanoma cell lines; *ISEV22 Lyon*

Németh A, Kós T, Bányai GL, Gaál A, Varga Z, Dank M, Takács I, Szász AM, Garay T; Can extracellular vesicles transmit vemurafenib resistance in melanoma cells in vitro?; *EACR 2022 Sevilla*

Németh A; Isolation methods and storage stability of extracellular vesicles; *Phd Proceedings Annual Issues of the Doctoral School Faculty of Information Technology and Bionics 2022*

Conference posters:

Németh A, Simon A, Bányai GL, Garay T; Extracellular vesicles pretreatment enhances melanoma cell migration despite dual MAPK pathway inhibition; *PhD Scientific Days 2025 Budapest*

Németh A, Lässer C, Bagge RO, Ekström K; Evaluating Nano-Flow Cytometry for Detecting HER2-Positive Extracellular Vesicles in Breast Cancer Patients; *1st Swedish Extracellular Vesicles Network Meeting Stockholm*

Kvasznicza J, Németh A, Bányai GL, Szőcs L, Garay T Cyclodextrin's Role in Modifying Cancer Cell Extracellular Vesicles; *UKEV2024 Newcastle*

Németh A, Ekström K, Rák Á, Cserey Gy, Hegedűs B, Bölükbas S, Visnovitz T, Garay T; Distinguishing NSCLC, MPM, and pleuritis patients using extracellular vesicles isolated from pleural fluids; *EACR Liquid Biopsies 2024 Lyon*

Németh A, Ekström K, Rák Á, Cserey Gy, Hegedűs B, Bölükbas S, Visnovitz T, Garay T; Surface marker detection of extracellular vesicles isolated from pleural fluids of NSCLC, MPM and pleuritis patients; *HSEV2024 Budapest*

Németh A, Bányai GL, Dobos NK, Kós T, Gaál A, Varga Z, Buzás EI, Khamari D, Dank M, Takács I, Szász AM, Garay T; Extracellular vesicles promote migration despite BRAF inhibitor treatment; *HSEV2024 Budapest*

Kvasznicza J, Magyar R, Bányai GL, Szőcs L, Németh A, Garay T; Cyclodextrins affect extracellular vesicle production in melanoma in vitro; HSEV2024 Budapest

Choi J, Görög D, Gaál A, Khamari D, Buzás EI, Németh A, Garay T, Bányai GL; Investigating the effect of extracellular vesicles on proliferation and migration on syngeneic colorectal cancer cell lines; *Small New word 2.0 2023 Graz*

Németh A, Linderholm B, Bagge RO, Ekström K; Is it possible to detect HER2-positive extracellular vesicles in human plasma?; *Small New word 2.0 2023 Graz*

Németh A, Bányai GL, Dobos NK, Kós T, Gaál A, Varga Z, Szász AM, Garay T; Extracellular vesicles can promote migration and transfer vemurafenib resistance among melanoma cells; Small New word 2.0 2023 Graz

Dobos NK, Németh A, Kvasznicza J, Magyar R, Görög D, Dank M, Takács I, Szász AM, Garay T; Are the observed effects on cell proliferation EV-specific or are other cell culture supernatants important players too? *Small New word 2.0 2023 Graz*

Kvasznicza J, Magyar R, Bányai GL, Rohan Zs, Szőcs L, Németh A; Cyclodextrins affect extracellular vesicle production in melanoma in vitro, *Small New word 2.0 2023 Graz*

Németh A, Bányai GL, Dobos NK, Kós T, Gaál A, Varga Z, Buzás EI, Khamari D, Dank M, Takács I, Szász AM, Garay T; Extracellular vesicles in vemurafenib resistance in melanoma cells; *Semmelweis Symposium 2022 Budapest*

Czárán D, Horváth Á, Sasvári P, Németh A, Helyes Zs, Csépányi-Kömi R; Mitigated Symptoms of rheumatoid arthritis in ARHGAP25-deficient mice and involvement of neutrophils in this progress; *The Neutrophil 2021 online*

Czárán D, Horváth Á, Sasvári P, Németh A, Wisniewski É, Helyes Zs; Reduced symptoms of arthritis in ARHGAP25 knockout mice and the possible mechanisms behind it; DOSZ2021

9. Acknowledgments

First and foremost, I would like to express my deepest gratitude to my supervisor, **Dr. Tamás M. Garay**, for his continuous guidance, support, and encouragement throughout my doctoral journey. His mentorship has been a cornerstone of my development as a scientist.

I am sincerely thankful to my dear friend and fellow PhD student, **Gréta Lilla Bányai**, for standing by my side during long lab days and helping me navigate the complexities of migration data analysis and extracellular vesicle isolation.

To all the students who lent me their hands and hearts along the way, thank you. I am especially grateful to **Nikolett Kitti Dobos** and **Alexandra Simon** for their dedication and valuable assistance throughout the project.

I wish to extend my appreciation to the wonderful team at the **Sahlgrenska Center for Cancer Research** in Gothenburg, where I had the privilege to spend my Erasmus internship. Thank you for welcoming me with such warmth. In particular, I would like to thank **Karin Ekström**, my mentor during my time there, for her kindness, patience, and insightful guidance to experiments with clinical samples and the MACSPlex experiments.

Special thanks to **Anikó Gaál** and the **Biological Nano-Chemistry Research Group** at the Research Centre for Natural Sciences for their generous support with EV isolation and characterization, as well as to the **ELKH-SE Translational Extracellular Vesicle Research Group** for their help with the NTA measurements.

I am also deeply grateful to **Balázs Hegedűs** and the **Department of Thoracic Surgery** at University Medicine Essen – Ruhrlandklinik for providing the invaluable clinical samples that made part of this work possible.

Heartfelt thanks to **Ádám Rák** and **György Cserey** for their contribution to the machine learning algorithm used in evaluating the diagnostic potential of extracellular vesicles. Your work brought an exciting new layer of depth and innovation to this research.

Last but certainly not least, I thank my **family and friends**, for their endless patience, unwavering belief in me, and for reminding me to laugh, breathe, and never give up. Your love has been the quiet force behind every line written and every experiment completed.

References

[1] M. Yáñez-Mó *et al.*, "Biological properties of extracellular vesicles and their physiological functions," 2015, *Co-Action Publishing*. doi: 10.3402/jev.v4.27066.

[2] J. A. Welsh *et al.*, "Minimal information for studies of extracellular vesicles (MISEV2023): From basic to advanced approaches," *J Extracell Vesicles*, vol. 13, no. 2, Feb. 2024, doi: 10.1002/jev2.12404.

[3] X. Miao *et al.*, "Tailoring of apoptotic bodies for diagnostic and therapeutic applications:advances, challenges, and prospects," Dec. 01, 2024, *BioMed Central Ltd*. doi: 10.1186/s12967-024-05451-w.

[4] Y. Jiang *et al.*, "Migrasomes, a new mode of intercellular communication," Dec. 01, 2023, *BioMed Central Ltd*. doi: 10.1186/s12964-023-01121-4.

[5] Y. J. Liu and C. Wang, "A review of the regulatory mechanisms of extracellular vesicles-mediated intercellular communication," Dec. 01, 2023, *BioMed Central Ltd*. doi: 10.1186/s12964-023-01103-6.

[6] K. J. Svensson *et al.*, "Exosome uptake depends on ERK1/2-heat shock protein 27 signaling and lipid raft-mediated endocytosis negatively regulated by caveolin-1," *Journal of Biological Chemistry*, vol. 288, no. 24, pp. 17713–17724, Jun. 2013, doi: 10.1074/jbc.M112.445403.

[7] H. Zhang *et al.*, "Exosome-delivered EGFR regulates liver microenvironment to promote gastric cancer liver metastasis," *Nat Commun*, vol. 8, Apr. 2017, doi: 10.1038/ncomms15016.

[8] Y. Guo, M. Ashrafizadeh, M. M. Tambuwala, J. Ren, G. Orive, and G. Yu, "P-glycoprotein (P-gp)-driven cancer drug resistance: biological profile, non-coding RNAs, drugs and nanomodulators," *Drug Discov Today*, p. 104161, Nov. 2024, doi: 10.1016/j.drudis.2024.104161.

[9] E. Yang *et al.*, "PTRF/Cavin-1 enhances chemo-resistance and promotes temozolomide efflux through extracellular vesicles in glioblastoma," *Theranostics*, vol. 12, no. 9, pp. 4330–4347, 2022, doi: 10.7150/THNO.71763.

[10] Y. P. Loh, L. Xiao, and J. J. Park, "Trafficking of hormones and trophic factors to secretory and extracellular vesicles: a historical perspective and new hypothesis," 2023, *OAE Publishing Inc.* doi: 10.20517/evcna.2023.34.

[11] H. Â le Á ne Vincent-Schneider *et al.*, "Exosomes bearing HLA-DR1 molecules need dendritic cells to efficiently stimulate specific T cells," 2002.

[12] S. A. Walsh and T. A. Davis, "Key early proinflammatory signaling molecules encapsulated within circulating exosomes following traumatic injury," *Journal of Inflammation (United Kingdom)*, vol. 19, no. 1, Dec. 2022, doi: 10.1186/s12950-022-00303-0.

[13] G. Chen *et al.*, "Exosomal PD-L1 contributes to immunosuppression and is associated with anti-PD-1 response," *Nature*, vol. 560, no. 7718, pp. 382–386, Aug. 2018, doi: 10.1038/s41586-018-0392-8.

[14] C. L. Chiang *et al.*, "Dual targeted extracellular vesicles regulate oncogenic genes in advanced pancreatic cancer," *Nat Commun*, vol. 14, no. 1, Dec. 2023, doi: 10.1038/s41467-023-42402-3.

[15] M. Pucci *et al.*, "Extracellular Vesicles As miRNA Nano-Shuttles: Dual Role in Tumor Progression," Apr. 01, 2018, *Springer-Verlag France*. doi: 10.1007/s11523-018-0551-8.

[16] R. Romano *et al.*, “Extracellular vesicles and pancreatic cancer: Insights on the roles of mirna, lncrna, and protein cargos in cancer progression,” Jun. 01, 2021, *MDPI*. doi: 10.3390/cells10061361.

[17] R. T. Miceli *et al.*, “Extracellular vesicles, RNA sequencing, and bioinformatic analyses: Challenges, solutions, and recommendations,” Dec. 01, 2024, *John Wiley and Sons Inc*. doi: 10.1002/jev2.70005.

[18] J. Elzanowska, C. Semira, and B. Costa-Silva, “DNA in extracellular vesicles: biological and clinical aspects,” Jun. 01, 2021, *John Wiley and Sons Ltd*. doi: 10.1002/1878-0261.12777.

[19] M. Puhka *et al.*, “Metabolomic profiling of extracellular vesicles and alternative normalization methods reveal enriched metabolites and strategies to study prostate cancer-related changes,” *Theranostics*, vol. 7, no. 16, pp. 3824–3841, 2017, doi: 10.7150/thno.19890.

[20] G. Van Niel, G. D’Angelo, and G. Raposo, “Shedding light on the cell biology of extracellular vesicles,” Apr. 01, 2018, *Nature Publishing Group*. doi: 10.1038/nrm.2017.125.

[21] K. Miyado *et al.*, “The fusing ability of sperm is bestowed by CD9-containing vesicles released from eggs in mice,” 2008. [Online]. Available: www.pnas.org/cgi/content/full/

[22] E. Bianchi, B. Doe, D. Goulding, and G. J. Wright, “Juno is the egg Izumo receptor and is essential for mammalian fertilization,” *Nature*, vol. 508, no. 7497, pp. 483–487, 2014, doi: 10.1038/nature13203.

[23] K.-U. Wagner *et al.*, “Tsg101 Is Essential for Cell Growth, Proliferation, and Cell Survival of Embryonic and Adult Tissues,” *Mol Cell Biol*, vol. 23, no. 1, pp. 150–162, Jan. 2003, doi: 10.1128/mcb.23.1.150-162.2003.

[24] C. Korkut *et al.*, “Trans-Synaptic Transmission of Vesicular Wnt Signals through Evi/Wntless,” *Cell*, vol. 139, no. 2, pp. 393–404, Oct. 2009, doi: 10.1016/j.cell.2009.07.051.

[25] G. Tlaposo *et al.*, “B Lymphocytes Secrete Antigen-presenting Vesicles,” 1996.

[26] A. Ortiz, “Extracellular vesicles in cancer progression,” *Semin Cancer Biol*, vol. 76, pp. 139–142, Nov. 2021, doi: 10.1016/j.semcancer.2021.05.032.

[27] S. Sigdel, S. Swenson, and J. Wang, “Extracellular Vesicles in Neurodegenerative Diseases: An Update,” Sep. 01, 2023, *Multidisciplinary Digital Publishing Institute (MDPI)*. doi: 10.3390/ijms241713161.

[28] C. Kovácsházi *et al.*, “Effect of hypercholesterolemia on circulating and cardiomyocyte-derived extracellular vesicles,” *Sci Rep*, vol. 14, no. 1, Dec. 2024, doi: 10.1038/s41598-024-62689-6.

[29] H. Sheng *et al.*, “Insulinoma-Released Exosomes or Microparticles Are Immunostimulatory and Can Activate Autoreactive T Cells Spontaneously Developed in Nonobese Diabetic Mice,” *The Journal of Immunology*, vol. 187, no. 4, pp. 1591–1600, Aug. 2011, doi: 10.4049/jimmunol.1100231.

[30] J. Tian, G. Casella, Y. Zhang, A. Rostami, and X. Li, “Potential roles of extracellular vesicles in the pathophysiology, diagnosis, and treatment of autoimmune diseases,” *Int J Biol Sci*, vol. 16, no. 4, pp. 620–632, 2020, doi: 10.7150/ijbs.39629.

[31] D. G. Meckes, K. H. Y. Shair, A. R. Marquitz, C. P. Kung, R. H. Edwards, and N. Raab-Traub, "Human tumor virus utilizes exosomes for intercellular communication," *Proc Natl Acad Sci U S A*, vol. 107, no. 47, pp. 20370–20375, Nov. 2010, doi: 10.1073/pnas.1014194107.

[32] H. Peinado *et al.*, "Pre-metastatic niches: Organ-specific homes for metastases," May 01, 2017, *Nature Publishing Group*. doi: 10.1038/nrc.2017.6.

[33] N. Karimi, R. Dalirfardouei, T. Dias, J. Lötvall, and C. Lässer, "Tetraspanins distinguish separate extracellular vesicle subpopulations in human serum and plasma – Contributions of platelet extracellular vesicles in plasma samples," *J Extracell Vesicles*, vol. 11, no. 5, May 2022, doi: 10.1002/jev2.12213.

[34] X. Yao *et al.*, "Comparison of proteomic landscape of extracellular vesicles in pleural effusions isolated by three strategies," *Front Bioeng Biotechnol*, vol. 11, 2023, doi: 10.3389/fbioe.2023.1108952.

[35] G. Senesi *et al.*, "Extracellular vesicles from II trimester human amniotic fluid as paracrine conveyors counteracting oxidative stress," *Redox Biol*, vol. 75, p. 103241, Sep. 2024, doi: 10.1016/j.redox.2024.103241.

[36] A. Emelyanov *et al.*, "Cryo-electron microscopy of extracellular vesicles from cerebrospinal fluid," *PLoS One*, vol. 15, no. 1, Jan. 2020, doi: 10.1371/journal.pone.0227949.

[37] K. Ekström, R. Crescitelli, H. I. Pétursson, J. Johansson, C. Lässer, and R. O. Bagge, "Characterization of surface markers on extracellular vesicles isolated from lymphatic exudate from patients with breast cancer," *BMC Cancer*, vol. 22, no. 1, Dec. 2022, doi: 10.1186/s12885-021-08870-w.

[38] L. Reseco, A. Molina-Crespo, M. Atienza, E. Gonzalez, J. M. Falcon-Perez, and J. L. Cantero, "Characterization of Extracellular Vesicles from Human Saliva: Effects of Age and Isolation Techniques," *Cells*, vol. 13, no. 1, Jan. 2024, doi: 10.3390/cells13010095.

[39] U. Erdbrügger *et al.*, "Urinary extracellular vesicles: A position paper by the Urine Task Force of the International Society for Extracellular Vesicles," *J Extracell Vesicles*, vol. 10, no. 7, May 2021, doi: 10.1002/jev2.12093.

[40] J. D. Galley and G. E. Besner, "The therapeutic potential of breast milk-derived extracellular vesicles," Mar. 01, 2020, *MDPI AG*. doi: 10.3390/nu12030745.

[41] S. Y. Chong *et al.*, "Extracellular vesicles in cardiovascular diseases: Alternative biomarker sources, therapeutic agents, and drug delivery carriers," Jul. 01, 2019, *MDPI AG*. doi: 10.3390/ijms20133272.

[42] F. Momen-Heravi, S. J. Getting, and S. A. Moschos, "Extracellular vesicles and their nucleic acids for biomarker discovery," Dec. 01, 2018, *Elsevier Inc.* doi: 10.1016/j.pharmthera.2018.08.002.

[43] T. Janković and M. Janković, "Extracellular vesicles and glycans: new avenue for biomarker research," *Biochem Med (Zagreb)*, vol. 34, no. 2, Jun. 2024, doi: 10.11613/BM.2024.020503.

[44] Janet. Iwasa, W. F. . Marshall, and Gerald. Karp, *Karp's cell and molecular biology*. Wiley, 2020.

[45] B. Alberts *et al.*, "THE CELL Molecular Biology of Sixth Edition."

[46] L. B. Alexandrov *et al.*, "Signatures of mutational processes in human cancer," *Nature*, vol. 500, no. 7463, pp. 415–421, 2013, doi: 10.1038/nature12477.

[47] M. Olivier *et al.*, “Modelling mutational landscapes of human cancers in vitro,” *Sci Rep*, vol. 4, Mar. 2014, doi: 10.1038/srep04482.

[48] W. Hill, C. E. Weeden, and C. Swanton, “Tumor Promoters and Opportunities for Molecular Cancer Prevention,” Jul. 01, 2024, *American Association for Cancer Research Inc.* doi: 10.1158/2159-8290.CD-24-0128.

[49] N. M. Niehoff *et al.*, “Airborne mammary carcinogens and breast cancer risk in the Sister Study,” *Environ Int*, vol. 130, Sep. 2019, doi: 10.1016/j.envint.2019.06.007.

[50] N. Kumar, M. Lamba, A. K. Pachar, S. Yadav, and A. Acharya, “Microplastics – A Growing Concern as Carcinogens in Cancer Etiology: Emphasis on Biochemical and Molecular Mechanisms,” Dec. 01, 2024, *Springer*. doi: 10.1007/s12013-024-01436-0.

[51] E. Sage and N. Shikazono, “Radiation-induced clustered DNA lesions: Repair and mutagenesis,” Jun. 01, 2017, *Elsevier Inc.* doi: 10.1016/j.freeradbiomed.2016.12.008.

[52] C. Busby, “Ionizing radiation and cancer: The failure of the risk model,” Jan. 01, 2022, *Elsevier Ltd*. doi: 10.1016/j.ctarc.2022.100565.

[53] M. Watson, D. M. Holman, and M. Maguire-Eisen, “Ultraviolet Radiation Exposure and Its Impact on Skin Cancer Risk,” Aug. 01, 2016, *W.B. Saunders*. doi: 10.1016/j.soncn.2016.05.005.

[54] D. E. Brash, “UV signature mutations,” 2015, *Blackwell Publishing Inc.* doi: 10.1111/php.12377.

[55] R. Ijsselsteijn, J. G. Jansen, and N. de Wind, “DNA mismatch repair-dependent DNA damage responses and cancer,” Sep. 01, 2020, *Elsevier B.V.* doi: 10.1016/j.dnarep.2020.102923.

[56] V. Tiwari and D. M. Wilson, “DNA Damage and Associated DNA Repair Defects in Disease and Premature Aging,” Aug. 01, 2019, *Cell Press*. doi: 10.1016/j.ajhg.2019.06.005.

[57] J. Wu, H. Liu, T. Hu, and S. Wang, “Gene expression trend changes in breast cancer populations over two decades: insights from The Cancer Genome Atlas database,” *Hereditas*, vol. 159, no. 1, Dec. 2022, doi: 10.1186/s41065-022-00230-3.

[58] Radinsky R and R. A. Culp, “Clonal dominance of select subsets of viral Kirsten ras(+)-transformed 3T3 cells during tumor progression.,” *Int J Cancer*, 1991.

[59] A. Marusyk, D. P. Tabassum, P. M. Altrock, V. Almendro, F. Michor, and K. Polyak, “Non-cell-autonomous driving of tumour growth supports sub-clonal heterogeneity,” *Nature*, vol. 514, no. 7520, pp. 54–58, Oct. 2014, doi: 10.1038/nature13556.

[60] C. D. Roskelley and M. J. Bissell, “The dominance of the microenvironment in breast and ovarian cancer,” *Semin Cancer Biol*, vol. 12, no. 2, pp. 97–104, 2002, doi: 10.1006/scbi.2001.0417.

[61] Z. Tan *et al.*, “Mapping Breast Cancer Microenvironment Through Single-Cell Omics,” Apr. 20, 2022, *Frontiers Media S.A.* doi: 10.3389/fimmu.2022.868813.

[62] L. Harrington, R. Bristow, I. Tannock, R. Hill, and D. Cescon, “Basic Science of Oncology, Sixth Edition,” *McGraw-Hill Education*, 2021.

[63] T. N. Seyfried and L. C. Huysentruyt, “On the Origin of Cancer Metastasis,” 2013.

[64] Y. Suhail *et al.*, “Systems Biology of Cancer Metastasis,” Aug. 28, 2019, *Cell Press*. doi: 10.1016/j.cels.2019.07.003.

[65] R. Fontana, A. Mestre-Farrera, and J. Yang, “Update on Epithelial-Mesenchymal Plasticity in Cancer Progression,” Jan. 24, 2024, *Annual Reviews Inc.* doi: 10.1146/annurev-pathmechdis-051222-122423.

[66] P. Friedl and K. Wolf, “Tumour-cell invasion and migration: Diversity and escape mechanisms,” May 2003. doi: 10.1038/nrc1075.

[67] S. SenGupta, C. A. Parent, and J. E. Bear, “The principles of directed cell migration,” Aug. 01, 2021, *Nature Research*. doi: 10.1038/s41580-021-00366-6.

[68] J. J. Bravo-Cordero, L. Hodgson, and J. Condeelis, “Directed cell invasion and migration during metastasis,” Apr. 2012. doi: 10.1016/j.ceb.2011.12.004.

[69] H. Ji *et al.*, “Lymph node metastasis in cancer progression: molecular mechanisms, clinical significance and therapeutic interventions,” Dec. 01, 2023, *Springer Nature*. doi: 10.1038/s41392-023-01576-4.

[70] T. Pereira-Veiga, S. Schneegans, K. Pantel, and H. Wikman, “Circulating tumor cell-blood cell crosstalk: Biology and clinical relevance,” Aug. 30, 2022, *Elsevier B.V.* doi: 10.1016/j.celrep.2022.111298.

[71] S. Paget, “DISTRIBUTION OF SECONDARY GROWTHS IN CANCER OF THE BREAST,” 1889.

[72] M. Akhtar, A. Haider, S. Rashid, A. Dakhilalla, M. H. Al-Nabet, and S. Paget, “Paget’s ‘Seed and Soil’ Theory of Cancer Metastasis: An Idea Whose Time has Come SEED AND THE SOIL THEORY,” 2019. [Online]. Available: www.anatomicpathology.com|69

[73] Y. Gao, I. Bado, H. Wang, W. Zhang, J. M. Rosen, and X. H. F. Zhang, “Metastasis Organotropism: Redefining the Congenial Soil,” May 06, 2019, *Cell Press*. doi: 10.1016/j.devcel.2019.04.012.

[74] W. Liu *et al.*, “A brain-enriched lncRNA shields cancer cells from immune-mediated killing for metastatic colonization in the brain,” 2022, doi: 10.1073/pnas.

[75] V. Krishnan *et al.*, “Using MKK4’s metastasis suppressor function to identify and dissect cancer cell-microenvironment interactions during metastatic colonization,” *Cancer and Metastasis Reviews*, vol. 31, no. 3–4, pp. 605–613, Dec. 2012, doi: 10.1007/s10555-012-9371-y.

[76] C. A. Klein, “Cancer progression and the invisible phase of metastatic colonization,” Nov. 01, 2020, *Nature Research*. doi: 10.1038/s41568-020-00300-6.

[77] M. P. Bebelman, E. Janssen, D. M. Pegtel, and C. Crudden, “The forces driving cancer extracellular vesicle secretion,” Jan. 01, 2021, *Elsevier Inc.* doi: 10.1016/j.neo.2020.11.011.

[78] A. Becker, B. K. Thakur, J. M. Weiss, H. S. Kim, H. Peinado, and D. Lyden, “Extracellular Vesicles in Cancer: Cell-to-Cell Mediators of Metastasis,” Dec. 12, 2016, *Cell Press*. doi: 10.1016/j.ccell.2016.10.009.

[79] J. Cai *et al.*, “Extracellular vesicle-mediated transfer of donor genomic DNA to recipient cells is a novel mechanism for genetic influence between cells,” *J Mol Cell Biol*, vol. 5, no. 4, pp. 227–238, Aug. 2013, doi: 10.1093/jmcb/mjt011.

[80] G. Valcz *et al.*, “Small extracellular vesicle DNA-mediated horizontal gene transfer as a driving force for tumor evolution: Facts and riddles,” Aug. 08, 2022, *Frontiers Media S.A.* doi: 10.3389/fonc.2022.945376.

[81] B. H. Sung, T. Ketova, D. Hoshino, A. Zijlstra, and A. M. Weaver, "Directional cell movement through tissues is controlled by exosome secretion," *Nat Commun*, vol. 6, May 2015, doi: 10.1038/ncomms8164.

[82] C. McAtee *et al.*, "Secreted exosomes induce filopodia formation," Oct. 18, 2024. doi: 10.7554/eLife.101673.1.

[83] D. Hoshino *et al.*, "Exosome secretion is enhanced by invadopodia and drives invasive behavior," *Cell Rep*, vol. 5, no. 5, pp. 1159–1168, Dec. 2013, doi: 10.1016/j.celrep.2013.10.050.

[84] S. Maacha *et al.*, "Extracellular vesicles-mediated intercellular communication: Roles in the tumor microenvironment and anti-cancer drug resistance," Mar. 30, 2019, *BioMed Central Ltd*. doi: 10.1186/s12943-019-0965-7.

[85] J. Webber, R. Steadman, M. D. Mason, Z. Tabi, and A. Clayton, "Cancer exosomes trigger fibroblast to myofibroblast differentiation," *Cancer Res*, vol. 70, no. 23, pp. 9621–9630, Dec. 2010, doi: 10.1158/0008-5472.CAN-10-1722.

[86] S. Dror *et al.*, "Melanoma miRNA trafficking controls tumour primary niche formation," *Nat Cell Biol*, vol. 18, no. 9, pp. 1006–1017, Sep. 2016, doi: 10.1038/ncb3399.

[87] S. Rana, K. Malinowska, and M. Zöller, "Exosomal tumor microRNA modulates premetastatic organ cells," *Neoplasia (United States)*, vol. 15, no. 3, pp. 281–295, 2013, doi: 10.1593/neo.122010.

[88] V. Luga *et al.*, "Exosomes mediate stromal mobilization of autocrine Wnt-PCP signaling in breast cancer cell migration," *Cell*, vol. 151, no. 7, pp. 1542–1556, Dec. 2012, doi: 10.1016/j.cell.2012.11.024.

[89] O. De Wever, M. Van Bockstal, M. Mareel, A. Hendrix, and M. Bracke, "Carcinoma-associated fibroblasts provide operational flexibility in metastasis," 2014, *Academic Press*. doi: 10.1016/j.semcancer.2013.12.009.

[90] Y. Naito, Y. Yoshioka, Y. Yamamoto, and T. Ochiya, "How cancer cells dictate their microenvironment: present roles of extracellular vesicles," Feb. 01, 2017, *Birkhauser Verlag AG*. doi: 10.1007/s00018-016-2346-3.

[91] M. Schmidtmann and C. D'Souza-Schorey, "Extracellular Vesicles: Biological Packages That Modulate Tumor Cell Invasion," Dec. 01, 2023, *Multidisciplinary Digital Publishing Institute (MDPI)*. doi: 10.3390/cancers15235617.

[92] K. Al-Nedawi, B. Meehan, R. S. Kerbel, A. C. Allison, and J. Rak, "Endothelial expression of autocrine VEGF upon the uptake of tumor-derived microvesicles containing oncogenic EGFR." [Online]. Available: www.pnas.org/cgi/content/full/

[93] P. Kucharzewska *et al.*, "Exosomes reflect the hypoxic status of glioma cells and mediate hypoxia-dependent activation of vascular cells during tumor development," *Proc Natl Acad Sci U S A*, vol. 110, no. 18, pp. 7312–7317, Apr. 2013, doi: 10.1073/pnas.1220998110.

[94] Z. Huang and Y. Feng, "Exosomes derived from hypoxic colorectal cancer cells promote angiogenesis through Wnt4-Induced β-catenin signaling in endothelial cells," *Oncol Res*, vol. 25, no. 5, pp. 651–661, 2017, doi: 10.3727/096504016X14752792816791.

[95] Y. Shan *et al.*, “Hypoxia-Induced Matrix Metalloproteinase-13 Expression in Exosomes from Nasopharyngeal Carcinoma Enhances Metastases,” *Cell Death Dis*, vol. 9, no. 3, Mar. 2018, doi: 10.1038/s41419-018-0425-0.

[96] B. H. Sung *et al.*, “A live cell reporter of exosome secretion and uptake reveals pathfinding behavior of migrating cells,” *Nat Commun*, vol. 11, no. 1, Dec. 2020, doi: 10.1038/s41467-020-15747-2.

[97] J. Rak, “Microparticles in cancer,” 2010. doi: 10.1055/s-0030-1267043.

[98] R. E. Tilley, T. Holscher, R. Belani, J. Nieva, and N. Mackman, “Tissue factor activity is increased in a combined platelet and microparticle sample from cancer patients,” *Thromb Res*, vol. 122, no. 5, pp. 604–609, 2008, doi: 10.1016/j.thromres.2007.12.023.

[99] C. Marar, B. Starich, and D. Wirtz, “Extracellular vesicles in immunomodulation and tumor progression,” May 01, 2021, *Nature Research*. doi: 10.1038/s41590-021-00899-0.

[100] M. N. Theodoraki, S. S. Yerneni, T. K. Hoffmann, W. E. Gooding, and T. L. Whiteside, “Clinical significance of PD-L1 þ exosomes in plasma of head and neck cancer patients,” *Clinical Cancer Research*, vol. 24, no. 4, pp. 896–905, Feb. 2018, doi: 10.1158/1078-0432.CCR-17-2664.

[101] M. Czystowska-Kuzmicz *et al.*, “Small extracellular vesicles containing arginase-1 suppress T-cell responses and promote tumor growth in ovarian carcinoma,” *Nat Commun*, vol. 10, no. 1, Dec. 2019, doi: 10.1038/s41467-019-10979-3.

[102] L. Mincheva-Nilsson and V. Baranov, “Cancer exosomes and NKG2D receptor-ligand interactions: Impairing NKG2D-mediated cytotoxicity and anti-tumour immune surveillance,” 2014, *Academic Press*. doi: 10.1016/j.semcancer.2014.02.010.

[103] M. Wang, Y. Cai, Y. Peng, B. Xu, W. Hui, and Y. Jiang, “Exosomal LGALS9 in the cerebrospinal fluid of glioblastoma patients suppressed dendritic cell antigen presentation and cytotoxic T-cell immunity,” *Cell Death Dis*, vol. 11, no. 10, Oct. 2020, doi: 10.1038/s41419-020-03042-3.

[104] A. Hoshino and Lyden David, “Tumour exosome integrins determine organotropic metastasis,” 2015, *Brill Academic Publishers*. doi: 10.6084/m9.figshare.

[105] B. Costa-Silva *et al.*, “Pancreatic cancer exosomes initiate pre-metastatic niche formation in the liver,” *Nat Cell Biol*, vol. 17, no. 6, pp. 816–826, Jun. 2015, doi: 10.1038/ncb3169.

[106] N. Tominaga *et al.*, “Brain metastatic cancer cells release microRNA-181c-containing extracellular vesicles capable of destructing blood-brain barrier,” *Nat Commun*, vol. 6, Apr. 2015, doi: 10.1038/ncomms7716.

[107] M. Y. Fong *et al.*, “Breast-cancer-secreted miR-122 reprograms glucose metabolism in premetastatic niche to promote metastasis,” *Nat Cell Biol*, vol. 17, no. 2, pp. 183–194, Feb. 2015, doi: 10.1038/ncb3094.

[108] C. Pagliuca, L. Di Leo, and D. De Zio, “New Insights into the Phenotype Switching of Melanoma,” Dec. 01, 2022, *MDPI*. doi: 10.3390/cancers14246118.

[109] N. Turner, O. Ware, and M. Bosenberg, “Genetics of metastasis: melanoma and other cancers,” *Clin Exp Metastasis*, vol. 35, no. 5–6, pp. 379–391, Aug. 2018, doi: 10.1007/s10585-018-9893-y.

[110] L. A. Nurla and A. M. Forsea, “melanoma epidemiology in europe: what is new?,” Apr. 01, 2024, *Edizioni Minerva Medica*. doi: 10.23736/S2784-8671.24.07811-3.

[111] S. M. Hossain and M. R. Eccles, “Phenotype Switching and the Melanoma Microenvironment; Impact on Immunotherapy and Drug Resistance,” *Int J Mol Sci*, vol. 24, no. 2, p. 1601, Jan. 2023, doi: 10.3390/ijms24021601.

[112] S. Gandini *et al.*, “Meta-analysis of risk factors for cutaneous melanoma: II. Sun exposure,” *Eur J Cancer*, vol. 41, no. 1, pp. 45–60, Jan. 2005, doi: 10.1016/j.ejca.2004.10.016.

[113] H. Tsao and K. Niendorf, “Genetic testing in hereditary melanoma,” *J Am Acad Dermatol*, vol. 51, no. 5, pp. 803–808, 2004, doi: 10.1016/j.jaad.2004.04.045.

[114] S. Gandini *et al.*, “Meta-analysis of risk factors for cutaneous melanoma: I. Common and atypical naevi,” *Eur J Cancer*, vol. 41, no. 1, pp. 28–44, 2005, doi: 10.1016/j.ejca.2004.10.015.

[115] N. G. Marghoob, K. Liopyris, and N. Jaimes, “Dermoscopy: A review of the structures that facilitate melanoma detection,” Jun. 01, 2019, *American Osteopathic Association*. doi: 10.7556/jaoa.2019.067.

[116] J. E. Gershenwald and R. A. Scolyer, “Melanoma Staging: American Joint Committee on Cancer (AJCC) 8th Edition and Beyond,” Aug. 01, 2018, *Springer New York LLC*. doi: 10.1245/s10434-018-6513-7.

[117] A. Tasdogan *et al.*, “Cutaneous melanoma,” Apr. 03, 2025. doi: 10.1038/s41572-025-00603-8.

[118] Y. Guo, W. Pan, S. Liu, Z. Shen, Y. Xu, and L. Hu, “ERK/MAPK signalling pathway and tumorigenesis (Review),” *Exp Ther Med*, Jan. 2020, doi: 10.3892/etm.2020.8454.

[119] G. S. Inamdar, S. R. V. Madhunapantula, and G. P. Robertson, “Targeting the MAPK pathway in melanoma: Why some approaches succeed and other fail,” Sep. 2010. doi: 10.1016/j.bcp.2010.04.029.

[120] E. Hodis *et al.*, “A landscape of driver mutations in melanoma,” *Cell*, vol. 150, no. 2, pp. 251–263, Jul. 2012, doi: 10.1016/j.cell.2012.06.024.

[121] P. Savoia, P. Fava, F. Casoni, and O. Cremona, “Targeting the ERK signaling pathway in melanoma,” Mar. 02, 2019, *MDPI AG*. doi: 10.3390/ijms20061483.

[122] E. F. Giunta *et al.*, “Epigenetic regulation in melanoma: Facts and hopes,” Aug. 01, 2021, *MDPI*. doi: 10.3390/cells10082048.

[123] D. Pedri, P. Karras, E. Landeloos, J. C. Marine, and F. Rambow, “Epithelial-to-mesenchymal-like transition events in melanoma,” Mar. 01, 2022, *John Wiley and Sons Inc*. doi: 10.1111/febs.16021.

[124] V. O. Volpe, D. M. Klufas, U. Hegde, and J. M. Grant-Kels, “The new paradigm of systemic therapies for metastatic melanoma,” Aug. 01, 2017, *Mosby Inc.* doi: 10.1016/j.jaad.2017.04.1126.

[125] A. B. Warner *et al.*, “Long-Term Outcomes and Responses to Retreatment in Patients With Melanoma Treated With PD-1 Blockade,” 2020, doi: 10.1200/JCO.19.

[126] R. K. Vaddepally, P. Kharel, R. Pandey, R. Garje, and A. B. Chandra, “Review of indications of FDA-approved immune checkpoint inhibitors per NCCN guidelines with the level of evidence,” Mar. 01, 2020, *MDPI AG*. doi: 10.3390/cancers12030738.

[127] C. Robert *et al.*, “Anti-programmed-death-receptor-1 treatment with pembrolizumab in ipilimumab-refractory advanced melanoma: A randomised dose-comparison cohort of a phase 1 trial,” *The Lancet*, vol. 384, no. 9948, pp. 1109–1117, Sep. 2014, doi: 10.1016/S0140-6736(14)60958-2.

[128] M. A. Postow *et al.*, “Nivolumab and Ipilimumab versus Ipilimumab in Untreated Melanoma,” *New England Journal of Medicine*, vol. 372, no. 21, pp. 2006–2017, May 2015, doi: 10.1056/nejmoa1414428.

[129] P. F. Ferrucci, L. Pala, F. Conforti, and E. Cocorocchio, “Talimogene laherparepvec (T-vec): An intralesional cancer immunotherapy for advanced melanoma,” Mar. 02, 2021, *MDPI AG*. doi: 10.3390/cancers13061383.

[130] R. H. I. Andtbacka *et al.*, “Final analyses of OPTiM: A randomized phase III trial of talimogene laherparepvec versus granulocyte-macrophage colony-stimulating factor in unresectable stage III-IV melanoma,” *J Immunother Cancer*, vol. 7, no. 1, Jun. 2019, doi: 10.1186/s40425-019-0623-z.

[131] T. Jiang, C. Zhou, and S. Ren, “Role of IL-2 in cancer immunotherapy,” Jun. 02, 2016, *Taylor and Francis Inc.* doi: 10.1080/2162402X.2016.1163462.

[132] H. Ogawa *et al.*, “T Cells Dominate the Local Immune Response Induced by Intralesional IL-2 in Combination with Imiquimod and Retinoid for In-Transit Metastatic Melanoma,” *Journal of Investigative Dermatology*, vol. 138, no. 6, pp. 1442–1445, Jun. 2018, doi: 10.1016/j.jid.2017.12.027.

[133] F. Scarfì *et al.*, “The role of topical imiquimod in melanoma cutaneous metastases: A critical review of the literature,” *Dermatol Ther*, 2020.

[134] Z. Pourmanouchehri *et al.*, “Controlled release of 5-fluorouracil to melanoma cells using a hydrogel/micelle composites based on deoxycholic acid and carboxymethyl chitosan,” *Int J Biol Macromol*, vol. 206, pp. 159–166, May 2022, doi: 10.1016/j.ijbiomac.2022.02.096.

[135] H. Davies, G. R. Bignell, C. Cox, R. Wooster, M. R. Stratton, and P. A. Futreal, “Mutations of the BRAF gene in human cancer,” *Nature*, pp. 949–954, 2002.

[136] G. A. McArthur *et al.*, “Safety and efficacy of vemurafenib in BRAFV600E and BRAFV600K mutation-positive melanoma (BRIM-3): Extended follow-up of a phase 3, randomised, open-label study,” *Lancet Oncol*, vol. 15, no. 3, pp. 323–332, 2014, doi: 10.1016/S1470-2045(14)70012-9.

[137] P. B. Chapman *et al.*, “Improved Survival with Vemurafenib in Melanoma with BRAF V600E Mutation,” *New England Journal of Medicine*, vol. 364, no. 26, pp. 2507–2516, Jun. 2011, doi: 10.1056/nejmoa1103782.

[138] A. Hauschild *et al.*, “Dabrafenib in BRAF-mutated metastatic melanoma: A multicentre, open-label, phase 3 randomised controlled trial,” *The Lancet*, vol. 380, no. 9839, pp. 358–365, 2012, doi: 10.1016/S0140-6736(12)60868-X.

[139] S. A. Haueis *et al.*, "Does the distribution pattern of brain metastases during BRAF inhibitor therapy reflect phenotype switching?," *Melanoma Res*, vol. 27, no. 3, pp. 231–237, 2017, doi: 10.1097/CMR.0000000000000338.

[140] K. Imafuku, K. Yoshino, K. Yamaguchi, S. Tsuboi, K. Ohara, and H. Hata, "Sudden Onset of Brain Metastasis despite the Use of Vemurafenib for Another Metastatic Lesion in Malignant Melanoma Patients," *Case Rep Oncol*, vol. 10, no. 1, pp. 290–295, Jan. 2017, doi: 10.1159/000461576.

[141] S. M. Shaffer *et al.*, "Rare cell variability and drug-induced reprogramming as a mode of cancer drug resistance," *Nature*, vol. 546, no. 7658, pp. 431–435, Jun. 2017, doi: 10.1038/nature22794.

[142] A. R. Jazirehi, R. Nazarian, A. X. Torres-Collado, and J. S. Economou, "Aberrant apoptotic machinery confers melanoma dual resistance to BRAF V600E inhibitor and immune effector cells: immunosensitization by a histone deacetylase inhibitor," 2014. [Online]. Available: www.ajcei.us/

[143] V. Yadav *et al.*, "The CDK4/6 inhibitor LY2835219 overcomes vemurafenib resistance resulting from MAPK reactivation and cyclin D1 upregulation," *Mol Cancer Ther*, vol. 13, no. 10, pp. 2253–2263, Aug. 2014, doi: 10.1158/1535-7163.MCT-14-0257.

[144] Z. Ji *et al.*, "MITF modulates therapeutic resistance through EGFR signaling," *Journal of Investigative Dermatology*, vol. 135, no. 7, pp. 1863–1872, Jul. 2015, doi: 10.1038/jid.2015.105.

[145] F. Su *et al.*, "Resistance to selective BRAF inhibition can be mediated by modest upstream pathway activation," *Cancer Res*, vol. 72, no. 4, pp. 969–978, Feb. 2012, doi: 10.1158/0008-5472.CAN-11-1875.

[146] F. M. Kaplan, C. H. Kugel, N. Dadpey, Y. Shao, E. V. Abel, and A. E. Aplin, "SHOC2 and CRAF mediate ERK1/2 reactivation in mutant NRAS-mediated resistance to RAF inhibitor," *Journal of Biological Chemistry*, vol. 287, no. 50, pp. 41797–41807, Dec. 2012, doi: 10.1074/jbc.M112.390906.

[147] J. Choi *et al.*, "Identification of PLX4032-resistance mechanisms and implications for novel RAF inhibitors," *Pigment Cell Melanoma Res*, vol. 27, no. 2, pp. 253–262, Mar. 2014, doi: 10.1111/pcmr.12197.

[148] J. N. Anastas *et al.*, "WNT5A enhances resistance of melanoma cells to targeted BRAF inhibitors," *Journal of Clinical Investigation*, vol. 124, no. 7, pp. 2877–2890, Jul. 2014, doi: 10.1172/JCI70156.

[149] S. A. Luebker and S. A. Koepsell, "Diverse mechanisms of BRAF inhibitor resistance in melanoma identified in clinical and preclinical studies," 2019, *Frontiers Media S.A.* doi: 10.3389/fonc.2019.00268.

[150] W. Hu *et al.*, "AEBP1 upregulation confers acquired resistance to BRAF (V600E) inhibition in melanoma," *Cell Death Dis*, vol. 4, no. 11, Nov. 2013, doi: 10.1038/cddis.2013.441.

[151] L. Fattore *et al.*, "MicroRNAs in melanoma development and resistance to target therapy," 2017. [Online]. Available: www.impactjournals.com/oncotarget

[152] S. Liu *et al.*, "miR-200c/Bmi1 axis and epithelial-mesenchymal transition contribute to acquired resistance to BRAF inhibitor treatment," *Pigment Cell Melanoma Res*, vol. 28, no. 4, pp. 431–441, Jul. 2015, doi: 10.1111/pcmr.12379.

[153] L. Fattore *et al.*, "miR-579-3p controls melanoma progression and resistance to target therapy," *Proc Natl Acad Sci U S A*, vol. 113, no. 34, pp. E5005–E5013, Aug. 2016, doi: 10.1073/pnas.1607753113.

[154] P. A. Ascierto *et al.*, "Cobimetinib combined with vemurafenib in advanced BRAFV600-mutant melanoma (coBRIM): updated efficacy results from a randomised, double-blind, phase 3 trial," *Lancet Oncol*, vol. 17, no. 9, pp. 1248–1260, Sep. 2016, doi: 10.1016/S1470-2045(16)30122-X.

[155] A. Ribas *et al.*, "Combination of vemurafenib and cobimetinib in patients with advanced BRAFV600-mutated melanoma: A phase 1b study," *Lancet Oncol*, vol. 15, no. 9, pp. 954–965, 2014, doi: 10.1016/S1470-2045(14)70301-8.

[156] C. Robert *et al.*, "Improved Overall Survival in Melanoma with Combined Dabrafenib and Trametinib," *New England Journal of Medicine*, vol. 372, no. 1, pp. 30–39, Jan. 2015, doi: 10.1056/nejmoa1412690.

[157] G. V. Long *et al.*, "Dabrafenib and trametinib versus dabrafenib and placebo for Val600 BRAF-mutant melanoma: A multicentre, double-blind, phase 3 randomised controlled trial," *The Lancet*, vol. 386, no. 9992, pp. 444–451, Aug. 2015, doi: 10.1016/S0140-6736(15)60898-4.

[158] J. J. Luke, K. T. Flaherty, A. Ribas, and G. V. Long, "Targeted agents and immunotherapies: Optimizing outcomes in melanoma," Aug. 01, 2017, *Nature Publishing Group*. doi: 10.1038/nrclinonc.2017.43.

[159] D. Schadendorf *et al.*, "COLUMBUS 7-year update: A randomized, open-label, phase III trial of encorafenib plus binimetinib versus vemurafenib or encorafenib in patients with BRAF V600E/K-mutant melanoma," *Eur J Cancer*, vol. 204, Jun. 2024, doi: 10.1016/j.ejca.2024.114073.

[160] Y. Kiniwa and R. Okuyama, "Recent advances in molecular targeted therapy for unresectable and metastatic BRAF-mutated melanoma," *Jpn J Clin Oncol*, 2021.

[161] C. Teixido, P. Castillo, C. Martinez-Vila, A. Arance, and L. Alos, "Molecular markers and targets in melanoma," Sep. 01, 2021, *MDPI*. doi: 10.3390/cells10092320.

[162] A. Schulz *et al.*, "Head-to-Head Comparison of BRAF/MEK Inhibitor Combinations Proposes Superiority of Encorafenib Plus Trametinib in Melanoma," *Cancers (Basel)*, vol. 14, no. 19, Oct. 2022, doi: 10.3390/cancers14194930.

[163] A. Rossi, M. Roberto, M. Panebianco, A. Botticelli, F. Mazzuca, and P. Marchetti, "Drug resistance of BRAF-mutant melanoma: Review of up-to-date mechanisms of action and promising targeted agents," *Eur J Pharmacol*, vol. 862, no. August, p. 172621, 2019, doi: 10.1016/j.ejphar.2019.172621.

[164] I. Proietti *et al.*, "Mechanisms of acquired BRAF inhibitor resistance in melanoma: A systematic review," *Cancers (Basel)*, vol. 12, no. 10, pp. 1–29, 2020, doi: 10.3390/cancers12102801.

[165] A. Musi and L. Bongiovanni, "Extracellular Vesicles in Cancer Drug Resistance: Implications on Melanoma Therapy," Feb. 01, 2023, *MDPI*. doi: 10.3390/cancers15041074.

[166] T. R. Lunavat *et al.*, "BRAFV600 inhibition alters the microRNA cargo in the vesicular secretome of malignant melanoma cells," *Proc Natl Acad Sci U S A*, vol. 114, no. 29, pp. E5930–E5939, Jul. 2017, doi: 10.1073/pnas.1705206114.

[167] L. J. Vella, A. Behren, B. Coleman, D. W. Greening, A. F. Hill, and J. Cebon, “Intercellular Resistance to BRAF Inhibition Can Be Mediated by Extracellular Vesicle–Associated PDGFRβ,” *Neoplasia (United States)*, vol. 19, no. 11, pp. 932–940, 2017, doi: 10.1016/j.neo.2017.07.002.

[168] G. Cesi *et al.*, “A new ALK isoform transported by extracellular vesicles confers drug resistance to melanoma cells,” *Mol Cancer*, vol. 17, no. 1, pp. 1–14, 2018, doi: 10.1186/s12943-018-0886-x.

[169] H. I. Pass, G. V. Scagliotti, and D. Ball, “IASLC Thoracic Oncology, 2nd Edition,” *Elsevier*, 2018.

[170] R. W. Light and G. Y. Lee, “Textbook of Pleural Diseases 3rd edition,” *CRC Press, Taylor & Francis Group*, 2016.

[171] B. Smolarz, H. Łukasiewicz, D. Samulak, E. Piekarska, R. Kołaciński, and H. Romanowicz, “Lung Cancer-Epidemiology, Pathogenesis, Treatment and Molecular Aspect (Review of Literature).,” *Int J Mol Sci*, vol. 26, no. 5, Feb. 2025, doi: 10.3390/ijms26052049.

[172] H. Sung *et al.*, “Global Cancer Statistics 2020: GLOBOCAN Estimates of Incidence and Mortality Worldwide for 36 Cancers in 185 Countries,” *CA Cancer J Clin*, vol. 71, no. 3, pp. 209–249, May 2021, doi: 10.3322/caac.21660.

[173] R. Doll and A. B. Hill, “SMOKING AND CARCINOMA OF THE LUNG PRELIMINARY REPORT,” 1950.

[174] S. Couraud, G. Zalcman, B. Milleron, F. Morin, and P. J. Souquet, “Lung cancer in never smokers - A review,” *Eur J Cancer*, vol. 48, no. 9, pp. 1299–1311, Jun. 2012, doi: 10.1016/j.ejca.2012.03.007.

[175] W. D. Travis *et al.*, “The 2015 World Health Organization Classification of Lung Tumors: Impact of Genetic, Clinical and Radiologic Advances since the 2004 Classification,” Sep. 26, 2015, *Elsevier Inc*. doi: 10.1097/JTO.0000000000000630.

[176] R. S. Herbst, D. Morgensztern, and C. Boshoff, “The biology and management of non-small cell lung cancer,” Jan. 24, 2018, *Nature Publishing Group*. doi: 10.1038/nature25183.

[177] G. Bethune, D. Bethune, N. Ridgway, and Z. Xu, “Epidermal growth factor receptor (EGFR) in lung cancer: an overview and update,” *J Thorac Dis*, 2010.

[178] F. Skoulidis *et al.*, “Co-occurring genomic alterations define major subsets of KRAS-mutant lung adenocarcinoma with distinct biology, immune profiles, and therapeutic vulnerabilities,” *Cancer Discov*, vol. 5, no. 8, pp. 861–878, Aug. 2015, doi: 10.1158/2159-8290.CD-14-1236.

[179] M. Soda, Y. L. Choi, M. Enomoto, Y. Sugiyama, and H. Mano, “Identification of the transforming EML4–ALK fusion gene in non-small-cell lung cancer,” *Nature*, 2007.

[180] K. Bergethon *et al.*, “ROS1 rearrangements define a unique molecular class of lung cancers,” *Journal of Clinical Oncology*, vol. 30, no. 8, pp. 863–870, Mar. 2012, doi: 10.1200/JCO.2011.35.6345.

[181] T. Kohno *et al.*, “KIF5B-RET fusions in lung adenocarcinoma,” *Nat Med*, vol. 18, no. 3, pp. 375–377, Mar. 2012, doi: 10.1038/nm.2644.

[182] A. Mogi and H. Kuwano, “TP53 mutations in nonsmall cell lung cancer,” 2011. doi: 10.1155/2011/583929.

[183] F. Skoulidis *et al.*, "STK11/LKB1 mutations and PD-1 inhibitor resistance in KRAS-mutant lung adenocarcinoma," *Cancer Discov*, vol. 8, no. 7, pp. 822–835, Jul. 2018, doi: 10.1158/2159-8290.CD-18-0099.

[184] A. Mehta, S. Dobersch, A. J. Romero-Olmedo, and G. Barreto, "Epigenetics in lung cancer diagnosis and therapy," *Cancer and Metastasis Reviews*, vol. 34, no. 2, pp. 229–241, Jun. 2015, doi: 10.1007/s10555-015-9563-3.

[185] R. S. Herbst *et al.*, "Predictive correlates of response to the anti-PD-L1 antibody MPDL3280A in cancer patients," *Nature*, vol. 515, no. 7528, pp. 563–567, Nov. 2014, doi: 10.1038/nature14011.

[186] D. Planchard *et al.*, "Metastatic non-small cell lung cancer: ESMO Clinical Practice Guidelines for diagnosis, treatment and follow-up †," 2018.

[187] F. R. Hirsch, K. Suda, J. Wiens, and P. A. Bunn, "New and emerging targeted treatments in advanced non-small-cell lung cancer," Sep. 03, 2016, *Lancet Publishing Group*. doi: 10.1016/S0140-6736(16)31473-8.

[188] D. S. Ettinger *et al.*, "NCCN Guidelines® Insights: Non-Small Cell Lung Cancer, Version 2.2023," *J Natl Compr Canc Netw*, vol. 21, no. 4, pp. 340–350, Apr. 2023, doi: 10.6004/jnccn.2023.0020.

[189] N. Duma, R. Santana-Davila, and J. R. Molina, "Non–Small Cell Lung Cancer: Epidemiology, Screening, Diagnosis, and Treatment," Aug. 01, 2019, *Elsevier Ltd*. doi: 10.1016/j.mayocp.2019.01.013.

[190] N. I. Lindeman *et al.*, "Updated molecular testing guideline for the selection of lung cancer patients for treatment with targeted tyrosine kinase inhibitors guideline from the college of American pathologists, the international association for the study of lung cancer, and the association for molecular pathology," in *Archives of Pathology and Laboratory Medicine*, College of American Pathologists, Mar. 2018, pp. 321–346. doi: 10.5858/arpa.2017-0388-CP.

[191] E. Bertoli *et al.*, "Liquid Biopsy in NSCLC: An Investigation with Multiple Clinical Implications," Jul. 01, 2023, *Multidisciplinary Digital Publishing Institute (MDPI)*. doi: 10.3390/ijms241310803.

[192] G. Mezei, E. T. Chang, F. S. Mowat, and S. H. Moolgavkar, "Epidemiology of mesothelioma of the pericardium and tunica vaginalis testis," May 01, 2017, *Elsevier Inc.* doi: 10.1016/j.annepidem.2017.04.001.

[193] Z. Wang *et al.*, "Predicting Overall Survival for Patients with Malignant Mesothelioma Following Radiotherapy via Interpretable Machine Learning," *Cancers (Basel)*, vol. 15, no. 15, Aug. 2023, doi: 10.3390/cancers15153916.

[194] M. Carbone *et al.*, "Malignant mesothelioma: Facts, Myths, and Hypotheses," Jan. 2012. doi: 10.1002/jcp.22724.

[195] M. Janosikova, M. Nakladalova, and L. Stepanek, "Current causes of mesothelioma: how has the asbestos ban changed the perspective?," 2023, *Palacky University Olomouc*. doi: 10.5507/bp.2023.008.

[196] F. Galateau-Salle, A. Churg, V. Roggli, and W. D. Travis, "The 2015 world health organization classification of tumors of the pleura: Advances since the 2004 Classification," 2016, *Lippincott Williams and Wilkins*. doi: 10.1016/j.jtho.2015.11.005.

[197] S. Lettieri *et al.*, "The evolving landscape of the molecular epidemiology of malignant pleural mesothelioma," Mar. 01, 2021, *MDPI*. doi: 10.3390/jcm10051034.

[198] K. F. Harvey, X. Zhang, and D. M. Thomas, "The Hippo pathway and human cancer," Apr. 2013. doi: 10.1038/nrc3458.

[199] K. C. McLoughlin, A. S. Kaufman, and D. S. Schrump, "Targeting the epigenome in malignant pleural mesothelioma," Jun. 01, 2017, *AME Publishing Company*. doi: 10.21037/tlcr.2017.06.06.

[200] N. Kumagai-Takei *et al.*, "Effect of asbestos exposure on differentiation and function of cytotoxic T lymphocytes," Oct. 08, 2020, *BioMed Central Ltd*. doi: 10.1186/s12199-020-00900-6.

[201] F. E. Mott, "Mesothelioma: A Review," 2012.

[202] A. Scherpereel *et al.*, "Guidelines of the European Respiratory Society and the European Society of Thoracic Surgeons for the management of malignant pleural mesothelioma," Mar. 2010. doi: 10.1183/09031936.00063109.

[203] C. Boutin and F. Rey, "Thoracoscopy in pleural malignant mesothelioma: A prospective study of 188 consecutive patients. Part 1: Diagnosis," *Cancer*, vol. 72, no. 2, pp. 389–393, 1993, doi: 10.1002/1097-0142(19930715)72:2<389::AID-CNCR2820720213>3.0.CO;2-V.

[204] C. E. Comin, L. Novelli, A. Cavazza, M. Rotellini, F. Cianchi, and L. Messerini, "Expression of thrombomodulin, calretinin, cytokeratin 5/6, D2-40 and WT-1 in a series of primary carcinomas of the lung: an immunohistochemical study in comparison with epithelioid pleural mesothelioma," 2014

[205] R. Parra-Medina, J. P. Castañeda-González, V. Chaves-Cabezas, J. P. Alzate, and J. J. Chaves, "Diagnostic performance of immunohistochemistry markers for malignant pleural mesothelioma diagnosis and subtypes. A systematic review and meta-analysis," *Pathol Res Pract*, vol. 257, May 2024, doi: 10.1016/j.prp.2024.155276.

[206] R. W. Light, "Pleural Diseases 6th Edition," *Lippincott Williams & Wilkins*, 2013.

[207] B. V Reamy, P. M. Williams, and M. R. Odom, "Pleuritic Chest Pain: Sorting Through the Differential Diagnosis," 2017. [Online]. Available: www.aafp.org/afp.

[208] C. M. Lo Cascio, V. Kaul, S. Dhooria, A. Agrawal, and U. Chaddha, "Diagnosis of tuberculous pleural effusions: A review," Nov. 01, 2021, *W.B. Saunders Ltd*. doi: 10.1016/j.rmed.2021.106607.

[209] J. M. Porcel, "Advances in the diagnosis of tuberculous pleuritis," Aug. 01, 2016, *AME Publishing Company*. doi: 10.21037/atm.2016.07.23.

[210] I. Cavallari, L. Urso, E. Sharova, G. Pasello, and V. Ciminale, "Liquid biopsy in malignant pleural mesothelioma: State of the art, pitfalls, and perspectives," 2019, *Frontiers Media S.A.* doi: 10.3389/fonc.2019.00740.

[211] I. Psallidas, I. Kalomenidis, J. M. Porcel, B. W. Robinson, and G. T. Stathopoulos, "Malignant pleural effusion: From bench to bedside," *European Respiratory Review*, vol. 25, no. 140, pp. 189–198, Jun. 2016, doi: 10.1183/16000617.0019-2016.

[212] N. Principe *et al.*, "Malignant Pleural Effusions—A Window Into Local Anti-Tumor T Cell Immunity?," Apr. 27, 2021, *Frontiers Media S.A.* doi: 10.3389/fonc.2021.672747.

[213] R. Thomas, H. M. Cheah, J. Creaney, B. A. Turlach, and Y. C. G. Lee, “Longitudinal Measurement of Pleural Fluid Biochemistry and Cytokines in Malignant Pleural Effusions,” *Chest*, 2016, doi: 10.1016/j.chest.2016.01.001.

[214] D. Lin *et al.*, “Circulating tumor cells: biology and clinical significance,” Dec. 01, 2021, *Springer Nature*. doi: 10.1038/s41392-021-00817-8.

[215] K. C. Andree, G. van Dalum, and L. W. M. M. Terstappen, “Challenges in circulating tumor cell detection by the CellSearch system,” Mar. 01, 2016, *Elsevier B.V.* doi: 10.1016/j.molonc.2015.12.002.

[216] K. Yoneda *et al.*, “Detection of circulating tumor cells with a novel microfluidic system in malignant pleural mesothelioma,” *Cancer Sci*, vol. 110, no. 2, pp. 726–733, Feb. 2019, doi: 10.1111/cas.13895.

[217] M. Ilie *et al.*, “‘Sentinel’ circulating tumor cells allow early diagnosis of lung cancer in patients with Chronic obstructive pulmonary disease,” *PLoS One*, vol. 9, no. 10, Oct. 2014, doi: 10.1371/journal.pone.0111597.

[218] M. Lim *et al.*, “A lab-on-a-disc platform enables serial monitoring of individual CTCs associated with tumor progression during EGFR-targeted therapy for patients with NSCLC,” *Theranostics*, vol. 10, no. 12, pp. 5181–5194, 2020, doi: 10.7150/thno.44693.

[219] D. E. S. Lustgarten *et al.*, “Use of circulating tumor cell technology (CELLSEARCH) for the diagnosis of malignant pleural effusions,” *Ann Am Thorac Soc*, vol. 10, no. 6, pp. 582–589, Dec. 2013, doi: 10.1513/AnnalsATS.201303-068OC.

[220] K. Gostomczyk *et al.*, “Flow cytometry in the detection of circulating tumor cells in neoplastic effusions,” *Clinica Chimica Acta*, vol. 552, Jan. 2024, doi: 10.1016/j.cca.2023.117651.

[221] A. Szpechcinski *et al.*, “Cell-free DNA levels in plasma of patients with non-small-cell lung cancer and inflammatory lung disease,” *Br J Cancer*, vol. 113, no. 3, pp. 476–483, Jul. 2015, doi: 10.1038/bjc.2015.225.

[222] K. A. Yoon, S. Park, H. L. Sang, H. K. Jin, and S. L. Jin, “Comparison of circulating plasma DNA levels between lung cancer patients and healthy controls,” *Journal of Molecular Diagnostics*, vol. 11, no. 3, pp. 182–185, 2009, doi: 10.2353/jmoldx.2009.080098.

[223] A. M. Newman *et al.*, “An ultrasensitive method for quantitating circulating tumor DNA with broad patient coverage,” *Nat Med*, vol. 20, no. 5, pp. 548–554, Apr. 2014, doi: 10.1038/nm.3519.

[224] L. E. Raez *et al.*, “Liquid Biopsy Versus Tissue Biopsy to Determine Front Line Therapy in Metastatic Non-Small Cell Lung Cancer (NSCLC),” *Clin Lung Cancer*, vol. 24, no. 2, pp. 120–129, Mar. 2023, doi: 10.1016/j.cllc.2022.11.007.

[225] P. C. Mack *et al.*, “Spectrum of driver mutations and clinical impact of circulating tumor DNA analysis in non–small cell lung cancer: Analysis of over 8000 cases,” *Cancer*, vol. 126, no. 14, pp. 3219–3228, Jul. 2020, doi: 10.1002/cncr.32876.

[226] H. Y. Wang *et al.*, “Enhanced detection of actionable mutations in NSCLC through pleural effusion cell-free DNA sequencing: A prospective study,” *Eur J Cancer*, vol. 217, Feb. 2025, doi: 10.1016/j.ejca.2025.115224.

[227] H. Kimura *et al.*, "EGFR mutation status in tumour-derived DNA from pleural effusion fluid is a practical basis for predicting the response to gefitinib," *Br J Cancer*, vol. 95, no. 10, pp. 1390–1395, Nov. 2006, doi: 10.1038/sj.bjc.6603428.

[228] X. Chen *et al.*, "Multigene PCR using both cfDNA and cfRNA in the supernatant of pleural effusion achieves accurate and rapid detection of mutations and fusions of driver genes in patients with advanced NSCLC," *Cancer Med*, vol. 10, no. 7, pp. 2286–2292, Apr. 2021, doi: 10.1002/cam4.3769.

[229] C. Pang *et al.*, "Pleural effusion as a substitute for tumor tissue in detecting EGFR/ALK mutations in non-small cell lung cancer: A systematic review and meta-analysis," May 01, 2019, *Lippincott Williams and Wilkins*. doi: 10.1097/MD.0000000000015450.

[230] K. Parikh *et al.*, "Individualized cell-free DNA monitoring with chromosomal junctions for mesothelioma," *JTO Clin Res Rep*, p. 100692, Dec. 2024, doi: 10.1016/j.jtocrr.2024.100692.

[231] G. Moretti *et al.*, "Liquid biopsies from pleural effusions and plasma from patients with malignant pleural mesothelioma: A feasibility study," *Cancers (Basel)*, vol. 13, no. 10, May 2021, doi: 10.3390/cancers13102445.

[232] R. Silvestri *et al.*, "Comparative analysis of genetic variants in pleural fluids and solid tissue biopsies of pleural mesothelioma patients: Implications for molecular heterogeneity assessment," *Heliyon*, vol. 10, no. 11, Jun. 2024, doi: 10.1016/j.heliyon.2024.e32152.

[233] K. B. Sriram *et al.*, "Pleural fluid cell-free DNA integrity index to identify cytologically negative malignant pleural effusions including mesotheliomas," *BMC Cancer*, vol. 12, Sep. 2012, doi: 10.1186/1471-2407-12-428.

[234] E. A. Klein *et al.*, "Clinical validation of a targeted methylation-based multi-cancer early detection test using an independent validation set," *Annals of Oncology*, vol. 32, no. 9, pp. 1167–1177, Sep. 2021, doi: 10.1016/j.annonc.2021.05.806.

[235] S. Guarrera *et al.*, "Peripheral Blood DNA Methylation as Potential Biomarker of Malignant Pleural Mesothelioma in Asbestos-Exposed Subjects," *Journal of Thoracic Oncology*, vol. 14, no. 3, pp. 527–539, Mar. 2019, doi: 10.1016/j.jtho.2018.10.163.

[236] K. A. Birnie *et al.*, "MicroRNA Signatures in Malignant Pleural Mesothelioma Effusions," *Dis Markers*, vol. 2019, 2019, doi: 10.1155/2019/8628612.

[237] B. Bixby *et al.*, "Cell-free DNA methylation analysis as a marker of malignancy in pleural fluid," *Sci Rep*, vol. 14, no. 1, Dec. 2024, doi: 10.1038/s41598-024-53132-x.

[238] N. Zhang *et al.*, "DNA Methylation Analysis of the SHOX2 and RASSF1A Panel Using Cell-Free DNA in the Diagnosis of Malignant Pleural Effusion," *J Oncol*, vol. 2023, 2023, doi: 10.1155/2023/5888844.

[239] J. C. M. Wan *et al.*, "Liquid biopsies come of age: Towards implementation of circulating tumour DNA," Apr. 01, 2017, *Nature Publishing Group*. doi: 10.1038/nrc.2017.7.

[240] G. Sozzi *et al.*, "Clinical utility of a plasma-based miRNA signature classifier within computed tomography lung cancer screening: A correlative MILD trial study," *Journal of Clinical Oncology*, vol. 32, no. 8, pp. 768–773, Mar. 2014, doi: 10.1200/JCO.2013.50.4357.

[241] Y. Yang *et al.*, "The clinical use of circulating microRNAs as non-invasive diagnostic biomarkers for lung cancers," 2017. [Online]. Available: www.impactjournals.com/oncotarget

[242] L. Santarelli *et al.*, "Association of MiR-126 with soluble mesothelin-related peptides, a marker for malignant mesothelioma," *PLoS One*, vol. 6, no. 4, 2011, doi: 10.1371/journal.pone.0018232.

[243] L. Santarelli *et al.*, "Combined circulating epigenetic markers to improve mesothelin performance in the diagnosis of malignant mesothelioma," *Lung Cancer*, 2015, doi: 10.1016/j.lungcan.2015.09.021.

[244] D. G. Weber *et al.*, "Circulating miR-132-3p as a candidate diagnostic biomarker for malignant mesothelioma," *Dis Markers*, vol. 2017, 2017, doi: 10.1155/2017/9280170.

[245] M. B. Kirschner *et al.*, "Increased circulating miR-625-3p: A potential biomarker for patients with malignant pleural mesothelioma," *Journal of Thoracic Oncology*, vol. 7, no. 7, pp. 1184–1191, 2012, doi: 10.1097/JTO.0b013e3182572e83.

[246] D. G. Weber *et al.*, "Combination of MIR-103a-3p and mesothelin improves the biomarker performance of malignant mesothelioma diagnosis," *PLoS One*, vol. 9, no. 12, Dec. 2014, doi: 10.1371/journal.pone.0114483.

[247] A. Faversani *et al.*, "An EBC/Plasma miRNA Signature Discriminates Lung Adenocarcinomas From Pleural Mesothelioma and Healthy Controls," *Front Oncol*, vol. 11, Jun. 2021, doi: 10.3389/fonc.2021.643280.

[248] Y. M. Shin *et al.*, "Diagnostic Value of Circulating Extracellular miR-134, miR-185, and miR-22 Levels in Lung Adenocarcinoma-Associated Malignant Pleural Effusion," *Cancer Res Treat*, vol. 46, no. 2, pp. 178–185, 2014, doi: 10.4143/crt.2014.46.2.178.

[249] H. S. Han *et al.*, "Downregulation of cell-free miR-198 as a diagnostic biomarker for lung adenocarcinoma-associated malignant pleural effusion," *Int J Cancer*, vol. 133, no. 3, pp. 645–652, Aug. 2013, doi: 10.1002/ijc.28054.

[250] R. Cappellesso *et al.*, "Young investigator challenge: MicroRNA-21/MicroRNA-126 profiling as a novel tool for the diagnosis of malignant mesothelioma in pleural effusion cytology," *Cancer Cytopathol*, vol. 124, no. 1, pp. 28–36, Jan. 2016, doi: 10.1002/cncy.21646.

[251] G. Ak *et al.*, "MicroRNA and mRNA features of malignant pleural mesothelioma and benign asbestos-related pleural effusion," *Biomed Res Int*, vol. 2015, 2015, doi: 10.1155/2015/635748.

[252] D. G. Weber *et al.*, "Circulating long non-coding RNA GAS5 (growth arrest-specific transcript 5) as a complement marker for the detection of malignant mesothelioma using liquid biopsies," *Biomark Res*, vol. 8, no. 1, May 2020, doi: 10.1186/s40364-020-00194-4.

[253] W. W. Wang, X. L. Zhou, Y. J. Song, C. H. Yu, W. G. Zhu, and Y. S. Tong, "Combination of long noncoding RNA MALAT 1 and carcinoembryonic antigen for the diagnosis of malignant pleural effusion caused by lung cancer," *Onco Targets Ther*, vol. 11, pp. 2333–2344, Apr. 2018, doi: 10.2147/OTT.S157551.

[254] Y. Wen, Y. Wang, Z. Xing, Z. Liu, and Z. Hou, "Microarray expression profile and analysis of circular RNA regulatory network in malignant pleural effusion," *Cell Cycle*, vol. 17, no. 24, pp. 2819–2832, Dec. 2018, doi: 10.1080/15384101.2018.1558860.

[255] S. C. Hsu *et al.*, "mRNA markers associated with malignant pleural effusion," *Sci Rep*, vol. 13, no. 1, Dec. 2023, doi: 10.1038/s41598-023-32872-2.

[256] K. Brennan *et al.*, "A comparison of methods for the isolation and separation of extracellular vesicles from protein and lipid particles in human serum," *Sci Rep*, vol. 10, no. 1, Dec. 2020, doi: 10.1038/s41598-020-57497-7.

[257] A. K. Krug *et al.*, "Improved EGFR mutation detection using combined exosomal RNA and circulating tumor DNA in NSCLC patient plasma," *Annals of Oncology*, vol. 29, no. 3, pp. 700–706, Mar. 2018, doi: 10.1093/annonc/mdx765.

[258] E. Castellanos-Rizaldos *et al.*, "Exosome-based detection of EGFR T790M in plasma from non–small cell lung cancer patients," *Clinical Cancer Research*, vol. 24, no. 12, pp. 2944–2950, Jun. 2018, doi: 10.1158/1078-0432.CCR-17-3369.

[259] J. Y. Hur *et al.*, "Extracellular vesicle-derived DNA for performing EGFR genotyping of NSCLC patients," *Mol Cancer*, vol. 17, no. 1, Jan. 2018, doi: 10.1186/s12943-018-0772-6.

[260] C. Lou *et al.*, "The mtDNA fragments within exosomes might be novel diagnostic biomarkers of non-small cell lung cancer," *Pathol Res Pract*, vol. 249, Sep. 2023, doi: 10.1016/j.prp.2023.154718.

[261] G. Rabinowits, C. Gerçel-Taylor, J. M. Day, D. D. Taylor, and G. H. Kloecker, "Exosomal microRNA: A diagnostic marker for lung cancer," *Clin Lung Cancer*, vol. 10, no. 1, pp. 42–46, 2009, doi: 10.3816/CLC.2009.n.006.

[262] J. Silva *et al.*, "Vesicle-related microRNAs in plasma of nonsmall cell lung cancer patients and correlation with survival," *European Respiratory Journal*, vol. 37, no. 3, pp. 617–623, Mar. 2011, doi: 10.1183/09031936.00029610.

[263] F. Grimolizzi *et al.*, "Exosomal miR-126 as a circulating biomarker in non-small-cell lung cancer regulating cancer progression," *Sci Rep*, vol. 7, no. 1, Dec. 2017, doi: 10.1038/s41598-017-15475-6.

[264] X. Jin *et al.*, "Evaluation of tumor-derived exosomal miRNA as potential diagnostic biomarkers for early-stage non-small cell lung cancer using next-generation sequencing," *Clinical Cancer Research*, vol. 23, no. 17, pp. 5311–5319, Sep. 2017, doi: 10.1158/1078-0432.CCR-17-0577.

[265] V. Poroyko *et al.*, "Exosomal miRNAs species in the blood of small cell and non-small cell lung cancer patients," 2018. [Online]. Available: www.oncotarget.com

[266] Y. Wu, J. Wei, W. Zhang, M. Xie, X. Wang, and J. Xu, "Serum exosomal miR-1290 is a potential biomarker for lung adenocarcinoma," *Onco Targets Ther*, vol. 13, pp. 7809–7818, 2020, doi: 10.2147/OTT.S263934.

[267] L. Min *et al.*, "Exosomal LncRNA RP5-977B1 as a novel minimally invasive biomarker for diagnosis and prognosis in non-small cell lung cancer," *Int J Clin Oncol*, vol. 27, no. 6, pp. 1013–1024, Jun. 2022, doi: 10.1007/s10147-022-02129-5.

[268] X. Zhang, H. Guo, Y. Bao, H. Yu, D. Xie, and X. Wang, "Exosomal long non-coding RNA dlx6-as1 as a potential diagnostic biomarker for non-small cell lung cancer," *Oncol Lett*, vol. 18, no. 5, pp. 5197–5204, 2019, doi: 10.3892/ol.2019.10892.

[269] T. Yamashita *et al.*, “Epidermal growth factor receptor localized to exosome membranes as a possible biomarker for lung cancer diagnosis,” *Pharmazie*, vol. 68, no. 12, pp. 969–973, Dec. 2013, doi: 10.1691/ph.2013.3599.

[270] W. Li *et al.*, “Machine Learning-Assisted Dual-Marker Detection in Serum Small Extracellular Vesicles for the Diagnosis and Prognosis Prediction of Non-Small Cell Lung Cancer,” *Nanomaterials*, vol. 12, no. 5, p. 809, Feb. 2022, doi: 10.3390/nano12050809.

[271] K. Ueda, N. Ishikawa, A. Tatsuguchi, N. Saichi, R. Fujii, and H. Nakagawa, “Antibody-coupled monolithic silica microtips for highthroughput molecular profiling of circulating exosomes,” *Sci Rep*, vol. 4, Aug. 2014, doi: 10.1038/srep06232.

[272] H. Jeong *et al.*, “Gcc2 as a new early diagnostic biomarker for non-small cell lung cancer,” *Cancers (Basel)*, vol. 13, no. 21, Nov. 2021, doi: 10.3390/cancers13215482.

[273] A. C. Soupir *et al.*, “Detectable Lipidomes and Metabolomes by Different Plasma Exosome Isolation Methods in Healthy Controls and Patients with Advanced Prostate and Lung Cancer,” *Int J Mol Sci*, vol. 24, no. 3, Feb. 2023, doi: 10.3390/ijms24031830.

[274] S. Kim *et al.*, “Plasma Exosome Analysis for Protein Mutation Identification Using a Combination of Raman Spectroscopy and Deep Learning,” *ACS Sens*, 2023, doi: 10.1021/acssensors.3c00681.

[275] H. Shin *et al.*, “Early-Stage Lung Cancer Diagnosis by Deep Learning-Based Spectroscopic Analysis of Circulating Exosomes,” *ACS Nano*, vol. 14, no. 5, pp. 5435–5444, May 2020, doi: 10.1021/acsnano.9b09119.

[276] D. Lu, Z. Shangguan, Z. Su, C. Lin, Z. Huang, and H. Xie, “Artificial intelligence-based plasma exosome label-free SERS profiling strategy for early lung cancer detection,” *Anal Bioanal Chem*, vol. 416, no. 23, pp. 5089–5096, Sep. 2024, doi: 10.1007/s00216-024-05445-z.

[277] H. Shin *et al.*, “Single test-based diagnosis of multiple cancer types using Exosome-SERS-AI for early stage cancers,” *Nat Commun*, vol. 14, no. 1, Dec. 2023, doi: 10.1038/s41467-023-37403-1.

[278] L. Yuan *et al.*, “Plasma extracellular vesicle phenotyping for the differentiation of early-stage lung cancer and benign lung diseases,” *Nanoscale Horiz*, vol. 8, no. 6, pp. 746–758, Mar. 2023, doi: 10.3390/cancers13215482.

[279] S. Rahimian, H. Najafi, B. Afzali, and M. Doroudian, “Extracellular Vesicles and Exosomes: Novel Insights and Perspectives on Lung Cancer from Early Detection to Targeted Treatment,” Jan. 01, 2024, *Multidisciplinary Digital Publishing Institute (MDPI)*. doi: 10.3390/biomedicines12010123.

[280] J. S. Lee *et al.*, “Liquid biopsy using the supernatant of a pleural effusion for EGFR genotyping in pulmonary adenocarcinoma patients: A comparison between cell-free DNA and extracellular vesicle-derived DNA,” *BMC Cancer*, vol. 18, no. 1, Dec. 2018, doi: 10.1186/s12885-018-5138-3.

[281] P. Hydbring *et al.*, “Exosomal RNA-profiling of pleural effusions identifies adenocarcinoma patients through elevated miR-200 and LCN2 expression,” *Lung Cancer*, vol. 124, pp. 45–52, Oct. 2018, doi: 10.1016/j.lungcan.2018.07.018.

[282] Y. Wang *et al.*, “Identification of differential expressed PE exosomal miRNA in lung adenocarcinoma, tuberculosis, and other benign lesions,” *Medicine (United States)*, vol. 96, no. 44, Nov. 2017, doi: 10.1097/MD.0000000000008361.

[283] H. Tamiya *et al.*, “Exosomal MicroRNA expression profiling in patients with lung adenocarcinoma-associated malignant pleural effusion,” *Anticancer Res*, vol. 38, no. 12, pp. 6707–6714, Dec. 2018, doi: 10.21873/anticanres.13039.

[284] E. Casalone *et al.*, “Serum Extracellular Vesicle-Derived microRNAs as Potential Biomarkers for Pleural Mesothelioma in a European Prospective Study,” *Cancers (Basel)*, vol. 15, no. 1, Jan. 2023, doi: 10.3390/cancers15010125.

[285] T. Cavalleri *et al.*, “Plasmatic extracellular vesicle microRNAs in malignant pleural mesothelioma and Asbestos-Exposed subjects suggest a 2-miRNA signature as potential biomarker of disease,” *PLoS One*, vol. 12, no. 5, May 2017, doi: 10.1371/journal.pone.0176680.

[286] L. Ferrari *et al.*, “Identification of a new potential plasmatic biomarker panel for the diagnosis of malignant pleural mesothelioma,” *Medicina del Lavoro*, vol. 113, no. 6, Dec. 2022, doi: 10.23749/mdl.v113i6.13522.

[287] A. Hoshino *et al.*, “Extracellular Vesicle and Particle Biomarkers Define Multiple Human Cancers,” *Cell*, vol. 182, no. 4, pp. 1044-1061.e18, Aug. 2020, doi: 10.1016/j.cell.2020.07.009.

[288] T. M. Chee, C. J. Zahra, K. M. Fong, I. A. Yang, and R. V. Bowman, “Potential utility of miRNAs derived from pleural fluid extracellular vesicles to differentiate between benign and malignant pleural effusions,” *Transl Lung Cancer Res*, vol. 14, no. 1, pp. 124–138, Jan. 2025, doi: 10.21037/tlcr-24-945.

[289] J. Javadi *et al.*, “Diagnostic and prognostic utility of the extracellular vesicles subpopulations present in pleural effusion,” *Biomolecules*, vol. 11, no. 11, Nov. 2021, doi: 10.3390/biom11111606.

[290] F. Lai, C. C. Jiang, M. L. Farrelly, X. D. Zhang, and P. Hersey, “Evidence for upregulation of Bim and the splicing factor SRp55 in melanoma cells from patients treated with selective BRAF inhibitors,” *Melanoma Res*, vol. 22, no. 3, pp. 244–251, Jun. 2012, doi: 10.1097/CMR.0b013e328353eff2.

[291] J. Timár, I. Kovalszky, S. Paku, K. Lapis, and L. Kopper, “Two human melanoma xenografls with different metastatic capacity and glycosaminoglycan pattern,” 1989.

[292] T. Visnovitz *et al.*, “An improved 96 well plate format lipid quantification assay for standardisation of experiments with extracellular vesicles,” *J Extracell Vesicles*, vol. 8, no. 1, Jan. 2019, doi: 10.1080/20013078.2019.1565263.

[293] T. C. Chou, “Drug combination studies and their synergy quantification using the chou-talalay method,” Jan. 15, 2010. doi: 10.1158/0008-5472.CAN-09-1947.

[294] F. Piccinini, A. Kiss, and P. Horvath, “CellTracker (not only) for dummies,” *Bioinformatics*, vol. 32, no. 6, pp. 955–957, Mar. 2016, doi: 10.1093/bioinformatics/btv686.

[295] S. Allelein *et al.*, “Potential and challenges of specifically isolating extracellular vesicles from heterogeneous populations,” *Sci Rep*, vol. 11, no. 1, Dec. 2021, doi: 10.1038/s41598-021-91129-y.

[296] D. K. Jeppesen *et al.*, “Comparative analysis of discrete exosome fractions obtained by differential centrifugation,” *J Extracell Vesicles*, vol. 3, no. 1, 2014, doi: 10.3402/jev.v3.25011.

[297] E. Lattmann and M. P. Levesque, “The Role of Extracellular Vesicles in Melanoma Progression,” Jul. 01, 2022, *MDPI*. doi: 10.3390/cancers14133086.

[298] M. C. Larson, J. E. Woodliff, C. A. Hillery, T. J. Kearl, and M. Zhao, “Phosphatidylethanolamine is externalized at the surface of microparticles,” *Biochim Biophys Acta Mol Cell Biol Lipids*, vol. 1821, no. 12, pp. 1501–1507, Dec. 2012, doi: 10.1016/j.bbalip.2012.08.017.

[299] A. Del Curatolo *et al.*, “Therapeutic potential of combined BRAF/MEK blockade in BRAF-wild type preclinical tumor models,” *Journal of Experimental and Clinical Cancer Research*, vol. 37, no. 1, Jul. 2018, doi: 10.1186/s13046-018-0820-5.

[300] H. Niessner *et al.*, “Exploring the In Vitro and In Vivo Therapeutic Potential of BRAF and MEK Inhibitor Combination in NRAS-Mutated Melanoma,” *Cancers (Basel)*, vol. 15, no. 23, Dec. 2023, doi: 10.3390/cancers15235521.

[301] V. Patel, I. Szász, V. Koroknai, T. Kiss, and M. Balázs, “Molecular alterations associated with acquired drug resistance during combined treatment with encorafenib and binimetinib in melanoma cell lines,” *Cancers (Basel)*, vol. 13, no. 23, Dec. 2021, doi: 10.3390/cancers13236058.

[302] M. R. Dourado *et al.*, “Extracellular vesicles derived from cancer-associated fibroblasts induce the migration and invasion of oral squamous cell carcinoma,” *J Extracell Vesicles*, vol. 8, no. 1, Jan. 2019, doi: 10.1080/20013078.2019.1578525.

[303] I. Lazar *et al.*, “Proteome characterization of melanoma exosomes reveals a specific signature for metastatic cell lines,” *Pigment Cell Melanoma Res*, vol. 28, no. 4, pp. 464–475, Jul. 2015, doi: 10.1111/pcmr.12380.

[304] J. Mazurkiewicz *et al.*, “Melanoma cells with diverse invasive potential differentially induce the activation of normal human fibroblasts,” *Cell Communication and Signaling*, vol. 20, no. 1, Dec. 2022, doi: 10.1186/s12964-022-00871-x.

[305] F. Mannavola, M. Tucci, C. Felici, A. Passarelli, S. D’Oronzo, and F. Silvestris, “Tumor-derived exosomes promote the in vitro osteotropism of melanoma cells by activating the SDF-1/CXCR4/CXCR7 axis,” *J Transl Med*, vol. 17, no. 1, pp. 1–15, 2019, doi: 10.1186/s12967-019-1982-4.

[306] S. Sakha, T. Muramatsu, K. Ueda, and J. Inazawa, “Exosomal microRNA miR-1246 induces cell motility and invasion through the regulation of DENND2D in oral squamous cell carcinoma,” *Sci Rep*, vol. 6, Dec. 2016, doi: 10.1038/srep38750.

[307] L. P. Sun *et al.*, “Cancer-associated fibroblast-derived exosomal miR-382-5p promotes the migration and invasion of oral squamous cell carcinoma,” *Oncol Rep*, vol. 42, no. 4, pp. 1319–1328, 2019, doi: 10.3892/or.2019.7255.

[308] H. Gu *et al.*, “Exosomes derived from human mesenchymal stem cells promote gastric cancer cell growth and migration via the activation of the Akt pathway,” *Mol Med Rep*, vol. 14, no. 4, pp. 3452–3458, Oct. 2016, doi: 10.3892/mmr.2016.5625.

[309] S. P. Clerici, M. Peppelenbosch, G. Fuhler, S. R. Consonni, and C. V. Ferreira-Halder, “Colorectal Cancer Cell-Derived Small Extracellular Vesicles Educate Human Fibroblasts to Stimulate Migratory Capacity,” *Front Cell Dev Biol*, vol. 9, Jul. 2021, doi: 10.3389/fcell.2021.696373.

[310] X. Wang *et al.*, "Fetal dermal mesenchymal stem cell-derived exosomes accelerate cutaneous wound healing by activating Notch signaling," *Stem Cells Int*, vol. 2019, 2019, doi: 10.1155/2019/2402916.

[311] M. L. Bychkov *et al.*, "Extracellular Vesicles Derived from Acidified Metastatic Melanoma Cells Stimulate Growth, Migration, and Stemness of Normal Keratinocytes," *Biomedicines*, vol. 10, no. 3, Mar. 2022, doi: 10.3390/biomedicines10030660.

[312] B. Yang *et al.*, "High-metastatic cancer cells derived exosomal miR92a-3p promotes epithelial-mesenchymal transition and metastasis of low-metastatic cancer cells by regulating PTEN/Akt pathway in hepatocellular carcinoma," *Oncogene*, vol. 39, no. 42, pp. 6529–6543, Oct. 2020, doi: 10.1038/s41388-020-01450-5.

[313] E. Endzeliņs *et al.*, "Extracellular vesicles derived from hypoxic colorectal cancer cells confer metastatic phenotype to non-metastatic cancer cells," *Anticancer Res*, vol. 38, no. 9, pp. 5139–5147, Sep. 2018, doi: 10.21873/anticanres.12836.

[314] J. Pijuan *et al.*, "In vitro cell migration, invasion, and adhesion assays: From cell imaging to data analysis," *Front Cell Dev Biol*, vol. 7, no. JUN, 2019, doi: 10.3389/fcell.2019.00107.

[315] P. Masuzzo, M. Van Troys, C. Ampe, and L. Martens, "Taking Aim at Moving Targets in Computational Cell Migration," Feb. 01, 2016, *Elsevier Ltd*. doi: 10.1016/j.tcb.2015.09.003.

[316] M. E. Clark *et al.*, "Detection of BRAF splicing variants in plasma-derived cell-free nucleic acids and extracellular vesicles of melanoma patients failing targeted therapy therapies," 2020. [Online]. Available: www.oncotarget.com

[317] J. Zuo *et al.*, "Extracellular vesicles in cancer drug resistance: Mechanistic insights and therapeutic implications," Dec. 01, 2024, *John Wiley and Sons Inc*. doi: 10.1002/mog2.94.

[318] P. Luo *et al.*, "Metabolic characteristics of large and small extracellular vesicles from pleural effusion reveal biomarker candidates for the diagnosis of tuberculosis and malignancy," *J Extracell Vesicles*, vol. 9, no. 1, Jan. 2020, doi: 10.1080/20013078.2020.1790158.

[319] T. M. Chee *et al.*, "Optimal isolation of extracellular vesicles from pleural fluid and profiling of their microRNA cargo," *Journal of Extracellular Biology*, vol. 2, no. 10, Oct. 2023, doi: 10.1002/jex2.119.

[320] M. Herzog, I. Verdenik, K. Černe, and B. Kobal, "Extracellular Vesicle Characteristics in Local Fluid and Plasma Measured by Nanoparticle Tracking Analysis Can Help Differentiate High-Grade Serous Carcinoma from Benign Ovarian Pathology," *Diagnostics*, vol. 14, no. 19, Oct. 2024, doi: 10.3390/diagnostics14192235.

[321] L. Cortes-Dericks and R. A. Schmid, "CD44 and its ligand hyaluronan as potential biomarkers in malignant pleural mesothelioma: Evidence and perspectives," Apr. 12, 2017, *BioMed Central Ltd.* doi: 10.1186/s12931-017-0546-5.

[322] T. Hanagiri *et al.*, "Effects of hyaluronic acid and CD44 interaction on the proliferation and invasiveness of malignant pleural mesothelioma.," *Tumour Biol*, vol. 33, no. 6, pp. 2135–2141, 2012, doi: 10.1007/s13277-012-0473-5.

[323] R. L. Attanoos, R. Webb, and A. R. Gibbs, "CD44H expression in reactive mesothelium, pleural mesothelioma and pulmonary adenocarcinoma," 1997.

[324] A. M. Afify, R. Stern, and C. W. Michael, “Differentiation of mesothelioma from adenocarcinoma in serous effusions: The role of hyaluronic acid and CD44 localization,” *Diagn Cytopathol*, vol. 32, no. 3, pp. 145–150, Mar. 2005, doi: 10.1002/dc.20201.

[325] J. M. Porcel, A. Esquerda, F. Rodriguez-Panadero, A. Martínez-Iribarren, and S. Bielsa, “The use of pleural fluid sCD44v6/std ratio for distinguishing mesothelioma from other pleural malignancies,” *Journal of Thoracic Oncology*, vol. 6, no. 1, pp. 190–194, 2011, doi: 10.1097/JTO.0b013e318200f447.

[326] G. Pasello *et al.*, “Malignant pleural mesothelioma immune microenvironment and checkpoint expression: Correlation with clinical-pathological features and intratumor heterogeneity over time,” *Annals of Oncology*, vol. 29, no. 5, pp. 1258–1265, May 2018, doi: 10.1093/annonc/mdy086.

[327] L. V. Klotz *et al.*, “Impact of T Cell Ratios on Survival in Pleural Mesothelioma: Insights from Tumor Microenvironment Analysis,” *Cancers (Basel)*, vol. 16, no. 19, Oct. 2024, doi: 10.3390/cancers16193418.

[328] Z. Rivera *et al.*, “CSPG4 as a target of antibody-based immunotherapy for malignant mesothelioma,” *Clinical Cancer Research*, vol. 18, no. 19, pp. 5352–5363, Oct. 2012, doi: 10.1158/1078-0432.CCR-12-0628.

[329] K. M. Ilieva *et al.*, “Chondroitin sulfate proteoglycan 4 and its potential as an antibody immunotherapy target across different tumor types,” Jan. 10, 2018, *Frontiers Media S.A*. doi: 10.3389/fimmu.2017.01911.

[330] R. E. Beard *et al.*, “Multiple chimeric antigen receptors successfully target chondroitin sulfate proteoglycan 4 in several different cancer histologies and cancer stem cells,” *J Immunother Cancer*, vol. 2, no. 1, Aug. 2014, doi: 10.1186/2051-1426-2-25.

[331] Y. Dai *et al.*, “A Multivariate Diagnostic Model Based on Urinary EpCAM-CD9-Positive Extracellular Vesicles for Prostate Cancer Diagnosis,” *Front Oncol*, vol. 11, Nov. 2021, doi: 10.3389/fonc.2021.777684.

[332] M. S. Ostenfeld *et al.*, “miRNA profiling of circulating EpCAM+ extracellular vesicles: promising biomarkers of colorectal cancer,” *J Extracell Vesicles*, vol. 5, no. 1, Jan. 2016, doi: 10.3402/jev.v5.31488.

[333] P. T. Went *et al.*, “Frequent EpCam Protein Expression in Human Carcinomas,” 2004, doi: 10.1016/S0046-8177(03)00502-1.

[334] B. Sandfeld-Paulsen *et al.*, “Exosomal proteins as prognostic biomarkers in non-small cell lung cancer,” *Mol Oncol*, vol. 10, no. 10, p. 1595, Dec. 2016, doi: 10.1016/j.molonc.2016.10.003.

[335] E. Roca *et al.*, “Detection of EpCAM-positive microparticles in pleural fluid: A new approach to mini-invasively identify patients with malignant pleural effusions.” [Online]. Available: www.impactjournals.com/oncotarget

[336] K. Asleh, V. Dery, C. Taylor, M. Davey, M. A. Djeungoue-Petga, and R. J. Ouellette, “Extracellular vesicle-based liquid biopsy biomarkers and their application in precision immuno-oncology,” Dec. 01, 2023, *BioMed Central Ltd*. doi: 10.1186/s40364-023-00540-2.

Supplement

Machine learning algorithm:

The following section outlines the machine learning algorithm applied in this study, which was developed by Ádám Rák.

Data Acquisition and Preprocessing

Data were obtained from the multiplex bead-based analyses of the 82 patients. In addition to the initial three-category diagnosis, more refined four-category classification schemes were developed, representing different clinical perspectives.

These included: (1) a tumor-focused classification (distinguishing cancer, PM, and pleuritis); (2) a classification based on pleura involvement (distinguishing tumors affecting the pleura, tumors not affecting the pleura, PM, and pleuritis); (3) a tumor type-based classification (NSCLC, PM, other cancer, pleurits); and (4) a "strict criteria" classification retaining only unambiguous cases (pleura-affecting NSCLC, PM, pleuritis). An "X" label was used to denote unknown or non-applicable classifications.

Classification scheme	**Labels**
'tumor focused'	X, cancer, PM, pleuritis
'pleura involvement'	X, cancer in pleura, PM, cancer not in pleura, pleuritis
'tumor-type'	X, NSCLC, PM, other cancer, pleuritis
'strict criteria'	X, NSCLC in pleura, PM, pleuritis

SupTable1: Classification schemes and labels

Let x_{ij} represent the raw measured value for marker j on patient i, where $i \in \{1, 2, \ldots, 82\}$ and $j \in \{1, 2, \ldots, 37\}$. Due to the nature of the assay, some measurements were missing. Let m_{ij} be an indicator variable such that $m_{ij} = 1$ if x_{ij} is present and $m_{ij} = 0$ if x_{ij} is missing.

The data were preprocessed as follows:

1. **Missing Value Imputation:** Missing values (where $m_{ij} = 0$) were imputed using the mean value of the corresponding marker across all patients *for which that marker was present*. That is, for each marker j, the mean μ_j was calculated as:

$$\mu_j = \frac{\sum_{i=1}^{82} m_{ij} \cdot x_{ij}}{\sum_{i=1}^{82} m_{ij}}$$

   Missing values were then replaced: if $m_{ij} = 0$, then $x_{ij} \leftarrow \mu_j$.

2. **Standardization:** Each marker was standardized to have zero mean and unit variance. For each marker j, the standard deviation σ_j was calculated using only the *present* values:

$$\sigma_j = \sqrt{\frac{\sum_{i=1}^{82} m_{ij} \cdot \left(x_{ij} - \mu_j\right)^2}{\sum_{i=1}^{82} m_{ij}}}$$

   If $\sigma_j > 0$, the standardized value z_{ij} was calculated as:

$$z_{ij} = \frac{x_{ij} - \mu_j}{\sigma_j}$$

If $\sigma_j = 0$, all values of z_{ij} for that marker were set to 0. This handles the edge case where a marker has no variance. This is robust standardization.

The preprocessed data matrix is thus $\mathbf{Z} = [z_{ij}]$, and the mask matrix is $\mathbf{M} = [m_{ij}]$. The input to the model is the concatenation of the data matrix and the mask for each record, which is $\mathbf{X} = [\mathbf{Z}, \mathbf{M}] \in \mathrm{R}^{82\times37\times2}$.
For each of the four classification schemes, a label vector $\mathbf{y}^{(k)} \in \{0, 1, 2, 3, 4\}^{82}$ was created, where $k \in \{1, 2, 3, 4\}$ indexes the scheme. The "X" label was encoded as 0. Since classes are highly imbalanced, class weights were determined for each class.

Neural Network Architecture

A multi-task feedforward neural network was designed to simultaneously predict the diagnosis for all four classification schemes. The network architecture is as follows:

1. **Input Layer:** The input layer receives the preprocessed data matrix X reshaped, of size 37 × 2, representing the standardized marker values and the mask.
2. **Optional Feature Exclusion** An optional feature exclusion was implemented using a mask. The layer is multi- plied element-wise by a vector that has a single zero and otherwise only ones. The index of the zero is given by exclude MeasIndex parameter.
3. **Shared Layers:**
   - A dense layer with H units and no activation function.
   - A Gaussian noise layer with standard deviation σ_s.
   - B residual blocks, each consisting of:
     - Layer normalization.
     - A dense layer with H units and GELU activation.
     - A Gaussian noise layer with standard deviation σ_n.
     - A dropout layer with dropout rate p.
     - A residual connection adding the input of the block to the output.
   - A final Gaussian noise layer with standard deviation σ_n.
   - A final Dropout layer with dropout rate p.
4. **Output Layers:** Four separate dense output layers, one for each classification scheme. The output layer for scheme k has C_k units, where C_k is the number of classes in that scheme (including the "X" class). Each output layer uses a softmax activation function to produce a probability distribution over the classes:

$$\hat{y}^{(k)} = softmax\left(W^{(k)}h + b^{(k)}\right)$$

where $\mathbf{h}$ is the output of the shared layers, $\boldsymbol{W}^{(k)}$ is the weight matrix for output layer k, and $\boldsymbol{b}^{(k)}$ is the bias vector for output layer k.

The use of residual blocks, Gaussian noise, and dropout are key to mitigating overfitting on the small dataset. The shared layers learn common features across all classification tasks, while the separate output layers allow for specialization to each specific task.

Training Procedure

The model was trained using the AdamW optimizer, which combines Adam with weight decay regularization (weight decay parameter λ). The learning rate was initialized at α_0 and

exponentially decayed to α_{end} over *E* epochs, with a decay step of M, which equals to the sample size after augmentation.

The loss function for each classification scheme is a weighted sparse categorical cross-entropy. Due to significant class imbalance, each class was weighted inversely proportional to its frequency in the training set. Let $\omega_c^{(k)}$ be the weight for class *c* in classification scheme *k*. The loss of function for scheme *k* is:

$$L_k\left(y^{(k)}, \hat{y}^{(k)}\right) = -\frac{1}{N}\sum_{i=1} \omega_{y_i^{(k)}}^{(k)} \, log\left(\hat{y}_{i,y_i^{(k)}}^{(k)}\right)$$

where $y_i^{(k)}$ is the true class label for patient *i* in scheme *k*, and $\hat{y}_{i,c}^{(k)}$ is the predicted probability for class *c* for patient *i* in scheme *k*. The overall loss is the sum of the losses for all four schemes:

$$L = \sum_{k=1}^{4} L_k$$

The training dataset was simply 'augmented', repeating the records *M* times. This served a computational effectiveness on the hardware only. The training dataset was the entire dataset except for the single record, which was used for validation. The neural network was trained with a batch size of N − 1, where *N* equals the sample count, which is 82.

Leave-One-Out Cross-Validation (LOOCV)

Due to the small sample size (*N* = 82), model performance was evaluated using Leave-One-Out Cross-Validation (LOOCV). In LOOCV, the model is trained *N* times. In each iteration *i*, data from patient *i* is held out a the validation set, and the model is trained on the remaining *N* − 1 patients. The validation loss, calculated on the singleheld-out sample, is recorded for each iteration. The final LOOCV validation loss is the average of the validation losses across all *N* iterations:

$$LOOCVLoss = \frac{1}{N}\sum_{i=1}^{N} L_{val}^{(i)}$$

where $L_{val}^{(i)}$ is the validation loss for iteration *i*.

Hyperparameter Optimization via Meta-Learning

Due to the limited size of the dataset, a sophisticated hyperparameter optimization strategy was employed to identify the optimal configuration for the neural network. This strategy involved a two-stage process: initial random search followed by iterative meta-learning.
The hyperparameters include: number of blocks, hidden dimension, noise, dropout, exclude index, learning rates and the number of epochs. First a random set of hyperparameters were generated and evaluated. The best hyperparameters were selected based on their validation performance, and added to the hyper-training dataset. A neural network was trained on this set to predict validation loss. Using this meta-model, new candidate hyperparameters were predicted, and the best ones were used for model training and added to the meta-training dataset. This approach allowed for efficient exploration of the hyperparameter space and identification of configurations that generalize well despite the limited data.
Initial Random Search

An initial set of hyperparameter configurations was generated randomly. The ranges for each

hyperparameter are detailed in SupTable 1. For each configuration, a full LOOCV training procedure was performed as described above, and the resulting LOOCV validation loss was recorded.

Hyperparameter	Range/Values	Distribution/Notes
Number of Blocks ('numBlock')	1, 2, 3, 4, 5, 6, 7, 8, 9, 10	Discrete uniform
Hidden Dimension ('hiddenDim')	128, 256, 512, 1024, 2048	Discrete uniform
Noise Standard Deviation ('noiseDev')	0.1, 0.2, 0.3, 0.4, 0.5, 0.6, 0.7, 0.8, 0.9, 1.0	Discrete uniform
Sample Noise Standard Deviation ('sampleNoiseDev')	0.1, 0.2, 0.3, 0.4, 0.5, 0.6, 0.7, 0.8, 0.9, 1.0	Discrete uniform
Dropout Rate ("dropoutVal')	0.1, 0.2, 0.3, 0.4, 0.5, 0.6, 0.7, 0.8	Discrete uniform
Weight Decay ('weight_decay')	0.1, 0.12, 0.15, 0.18, 0.22, 0.27, 0.33, 0.40, 0.49, 0.60, 0.73, 0.89, 1.08, 1.32, 1.61, 1.96, 2.39, 2.91, 3.54, 4.31, 5.24, 6.38, 7.77, 9.46, 11.51, 14.01, 17.05, 20.75, 25.26, 30.74, 37.42, 45.55, 55.44, 67.48, 82.14, 100.00	Long uniform
Initial Learning Rate ('learning rate')	1E-03	Fixed
Final Learning Rate ('end learning rate')	1E-05	Fied
Epochs ('epochs')	5	Fixed

SupTable2: Hyperparameters explored during the initial random search phase. *The "Distribution/Notes" column indicates how values were chosen within the specified range. For the continuous 'weight decay', values are log-spaced, and the rounded values are shown.*

Meta-Learning Model

A secondary neural network, termed the "meta-model," was trained to predict the LOOCV validation loss of the primary neural network, given its hyperparameters as input. The meta-model architecture consisted of:

1. **Input Layer**: An input layer accepting a vector representing the hyperparameters of the primary neural network. Hyperparameters that were expected to have a logarithmic relationship with the validation loss (e.g., learning rate, weight decay) were log-transformed before being input to the meta-model.
2. **Hidden Layers:** Three dense hidden layers with 128, 64, and 32 units, respectively, each using the GELU activation function. Dropout layers (with a dropout rate of 0.2) were included after the first and second hidden layers for regularization.
3. **Output Layer**: A single output unit with a linear activation, predicting the LOOCV validation loss.

The meta-model was trained using the AdamW optimizer with a learning rate of 0.0001 and a weight decay of 1.8. The mean squared error (MSE) was used as the loss function. The meta-model was trained on the data collected during the initial random search, 'augmented' M=1000 times for computational effectiveness.

Iterative Optimization

Following the initial random search and meta-model training, an iterative optimization process was used:

4. **Candidate Generation:** A large batch of random hyperparameter configurations was generated.
5. **Prediction:** The trained meta-model was used to predict the LOOCV validation loss for each candidate configuration.
6. **Selection and Evaluation:** The hyperparameter configuration predicted to have the lowest validation loss was selected. The primary neural network was trained with this configuration using the full LOOCV procedure, and the actual validation loss was recorded.
7. **Dataset Augmentation:** The newly obtained hyperparameter configuration and its corresponding validation loss were added to the training data for the meta-model.
8. **Meta-Model Retraining:** The meta-model was retrained using the augmented dataset.

Steps 1-5 were repeated iteratively. This process allowed for efficient exploration of the hyperparameter space, guided by the meta-model's predictions. The process was terminated when the meta-model's predictions did not significantly improve upon the best observed validation loss. This indicates the search is around the global optimum.

Cell lines	EV treatment			
	Less agressive EV		More agressive EV	
	Migration Parameters			
	MSD	TTD	MSD	TTD
Mel Pt-1 pre	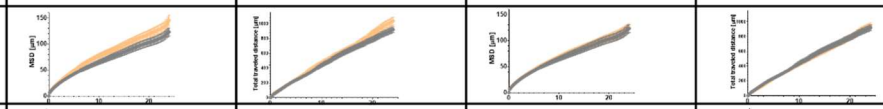			
Mel Pt-1 post				
Mel Pt-3 pre				
Mel Pt-3 post	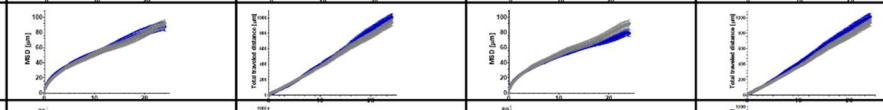			
Mel Pt-4 pre				
Mel Pt-4 post				
WM983A				
WM983B				
A2058				
M1	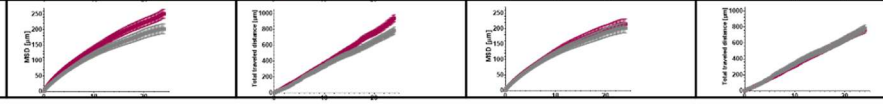			

Table S1. EVs effects on single cell migration. *Cells were tracked for 24 hours semiautomatically with CellTracker and Mean square displacement (MSD) and total travelled distance (TTD) was calculated, the two parameters are represented as a function of time Results of three independent measurements are shown as mean ± SEM. Grey indicates the vehicle treatment and colorful curves the EV-treated cells. Modified figure from Németh et al. 2024.*

Cell lines	EV TREATMENT					
	Vemurafenib		Less agressive EV + Vem		More agressive EV + Vem	
	Migration parameters					
	MSD	TTD	MSD	TTD	MSD	TTD
Mel Pt-1 pre						
Mel Pt-1 post						
Mel Pt-3 pre						
Mel Pt-3 post						
Mel Pt-4 pre						
Mel Pt-4 post						
WM983A						
WM983B						
A2058						
M1						

Table S2. Vemurafenib and EV + Vemurafenib (Vem) combination effects on single cell migration. *Cells were tracked for 24 hours semiautomatically with CellTracker and Mean square displacement (MSD) and total travelled distance (TTD) was calculated, the two parameters are represented as a function of time. Results of three independent measurements are shown as mean ± SEM. Grey indicates the vehicle treatment and colorful curves the treated cells. Modified figure from Németh et al. 2024.*

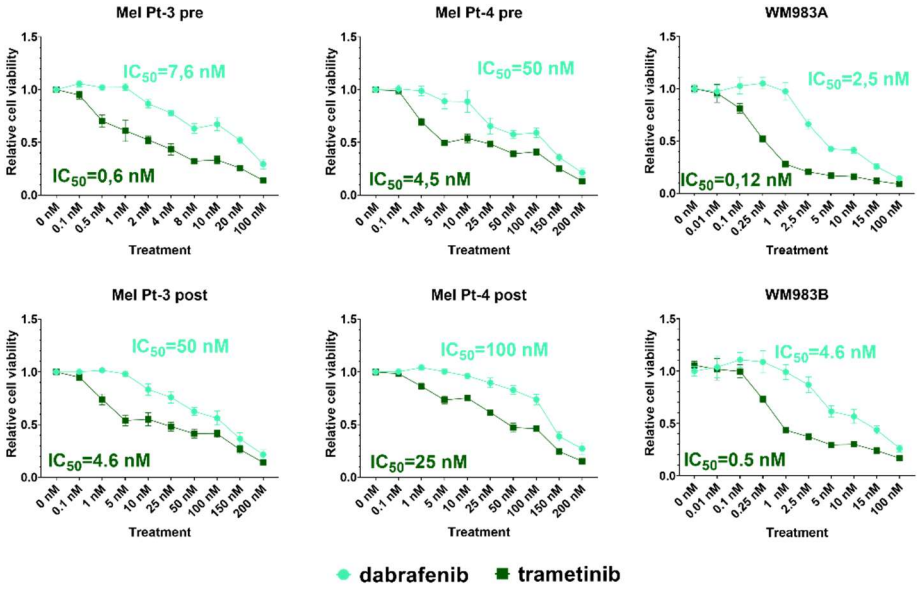

Supplementary Figure 1: Melanoma cell lines dabrafenib and trametinib sensitivity. *Relative cell viability was determined by SRV cell viability assay following 72 hours of drug treatment. The GI_{50} values for each treatment are highlighted. Data for three independent measurements represented as mean ± 95% confidence interval of. Modified figure from Németh et al. 2024.*

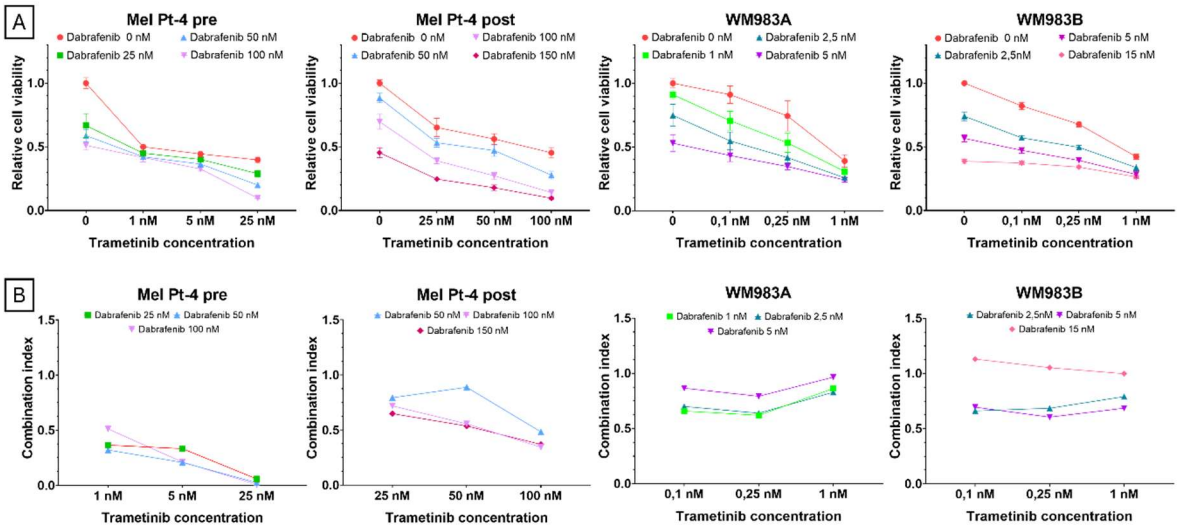

Supplementary Figure2: Dabrafenib and trametinib combination treatment sensitivity of Mel Pt-4 pre/post and WM983A/WM983B cell lines. *A) Relative cell viability for the selected three concentrations of BRAFi and MEKi, which was determined using SRB cell viability assay. Data represented as mean± 95% confidence interval (N=3; B) Calculated combination indexes (CI) for each combination, CI<1 synergism, CI=1 additive effect, CI>1 antagonism. Modified adapted of Németh et al. 2024.*

Cell lines	EV TREATMENT					
	Dabrafenib		Less agressive EV + Dab		More agressive EV + Dab	
	Migration parameters					
	MSD	TTD	MSD	TTD	MSD	TTD
Mel Pt-3 pre						
Mel Pt-3 post						

Cell lines	EV TREATMENT					
	Trametinib		Less agressive EV + Tram		More agressive EV + Tram	
	Migration parameters					
	MSD	TTD	MSD	TTD	MSD	TTD
Mel Pt-3 pre						
Mel Pt-3 post						

Cell lines	EV TREATMENT					
	Dabrafenib+Trametinib		Less agressive EV + Dab-Tram		More agressive EV + Dab-Tram	
	Migration parameters					
	MSD	TTD	MSD	TTD	MSD	TTD
Mel Pt-3 pre						
Mel Pt-3 post						

Table S3. Single cell migration under treatment of dabrafenib (drab), trametinib (ram), dabrafenib-trametinib and these drugs with combination of EVs. *Cells were tracked for 24 hours semiautomatically with CellTracker and Mean square displacement (MSD) and total travelled distance (TTD) was calculated, the two parameters are represented as a function of time. Results of three independent measurements are shown as mean ± SEM. Grey indicates the vehicle treatment and blue curves the treated cells. Modified figure from Németh et al. 2024.*

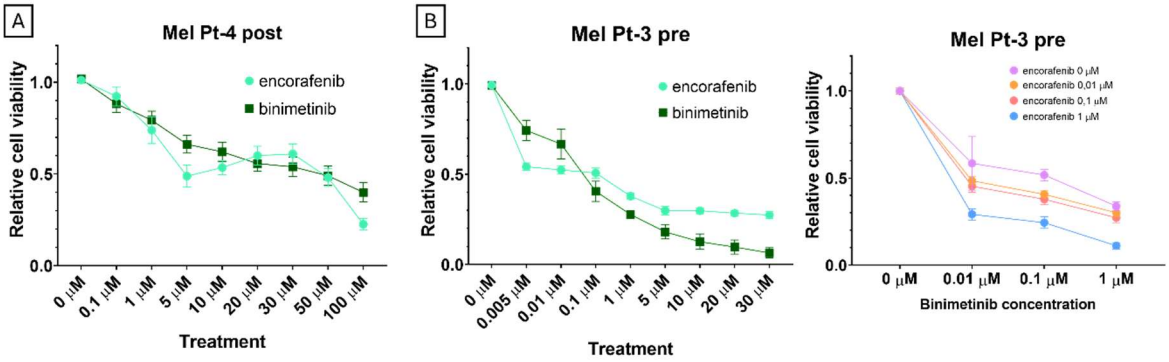

Supplementary Figure 3. Melanoma cells baseline encorafenib, binimetinib and their combination sensitivity. *A) Encorafenib and binimetinib monotherapy of Mel Pt-4 post cells; B) Mel Pt-3 pre sensitivity to encorafenib, binimetinib and their combination. Data represented as mean± 95% confidence interval (N=3).*

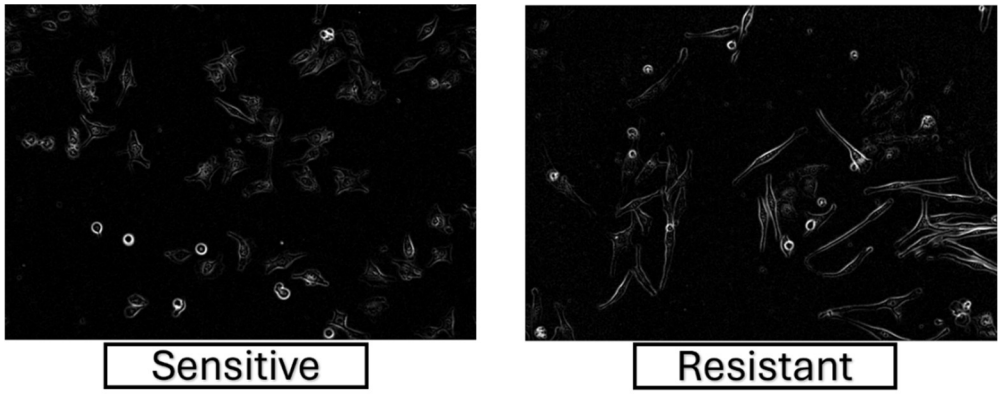

Supplementary Figure 4. Representative images of Mel Pt-4 post sens and res cell line clones.

Cell lines	TREATMENT						
	Sens EV	Res EV	Enco-Bini	Senss EV + Enco-Bini	Res EV + Enco-Bini	Seq Sens EV + Enco-Bini	Seq Ress EV + Enco-Bini
Mel Pt-4 post sens							
Mel Pt-4 post res							

Table S4. Single cell migration under treatment of sens/res EV, enco-bini, sens/res EV + enco-bini simultaneously, sequentially sens/res EV + enco-bini. *Cells were tracked for 24 hours semiautomatically with CellTracker and Mean square displacement (MSD) was calculated and represented as a function of time. Results of three independent measurements are shown as mean ± SEM. Grey indicates the vehicle treatment and pink curves the treated cells.*

A

Biological functions	Surface markers
EV markers	CD9, CD63, CD81
Cancer-associated/Stemness marker	CD24, CD326, ROR1, CD133
Immune-associated	CD2, CD8, CD14, CD25, CD40, CD45, CD56, HLA-ABC, HLA-RDRDPQ
Adhesion and migration markers	CD29, CD49e, CD44, CD146
Platelet-associated	CD41b, CD42a, CD62p
Angiogenesis and endothelial markers	CD31, CD105

B

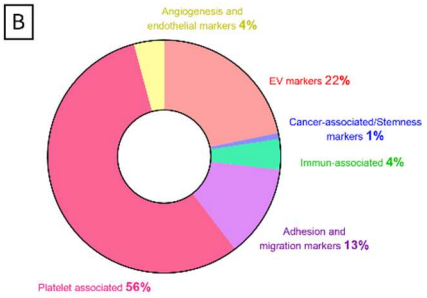

Supplementary Figure 5. Functional classification and relative distribution of EV surface marker signals in a breast cancer patient's plasma*. A) The surface markers that were present in the patients' plasma-derived EVs categorized into six groups according to their biological functions and cellular origin; B) Donut plots represent the proportional contribution of each group to the overall EV surface marker profile. Group-level signals were calculated as the normalized mean APC intensity of all markers within each functional category.*

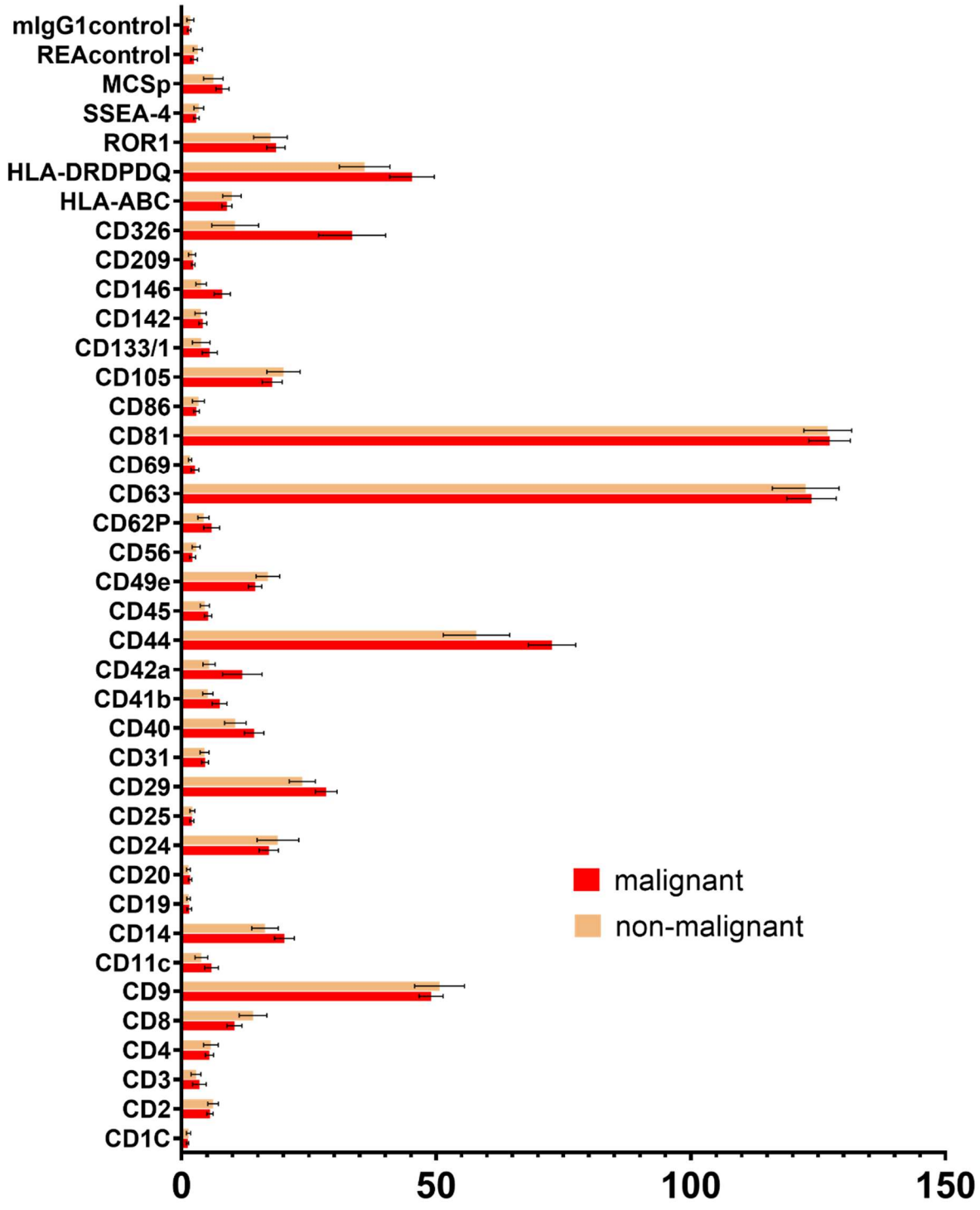

Supplementary Figure 6. EV surface marker profiles among malignant and non-malignant patients. *Extracellular vesicles isolated from pleural effusion samples were analyzed for surface marker expression using a multiplex bead-based flow cytometry assay. Each sample was assessed in triplicate to ensure technical reproducibility. Raw fluorescence intensities were first corrected for background using PBS controls and then normalized to the average signal of the tetraspanins CD9, CD63, and CD81. Results are expressed as mean ± SEM.*

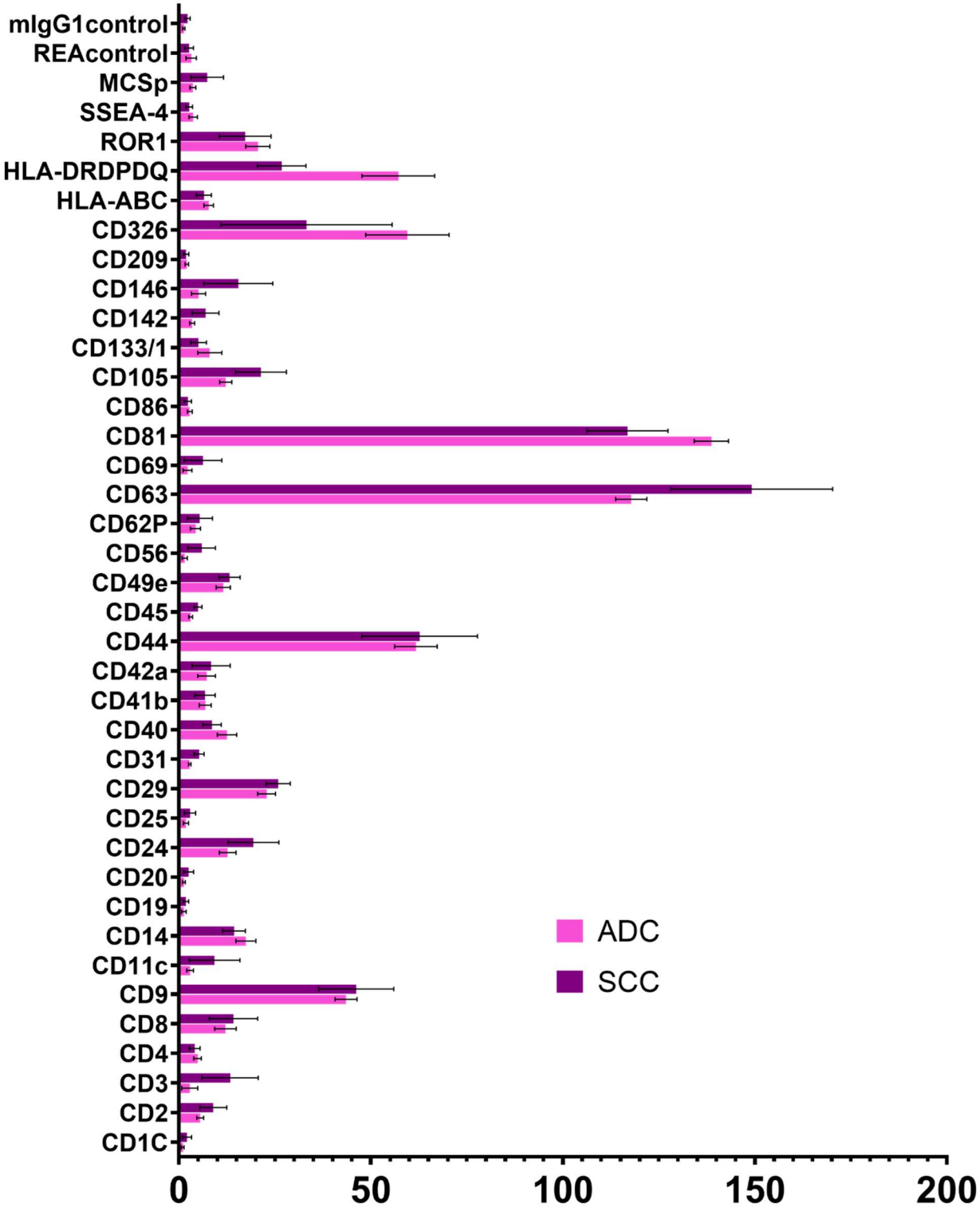

Supplementary Figure 7. EV surface marker profiles among NSCLC subtypes: adenocarcinoma (ADC) and squamous cell carcinoma (SCC). *Extracellular vesicles isolated from pleural effusion samples were analyzed for surface marker expression using a multiplex bead-based flow cytometry assay. Each sample was assessed in triplicate to ensure technical reproducibility. Raw fluorescence intensities were first corrected for background using PBS controls, and then normalized to the average signal of the tetraspanins CD9, CD63, and CD81. Results are expressed as mean ± SEM.*

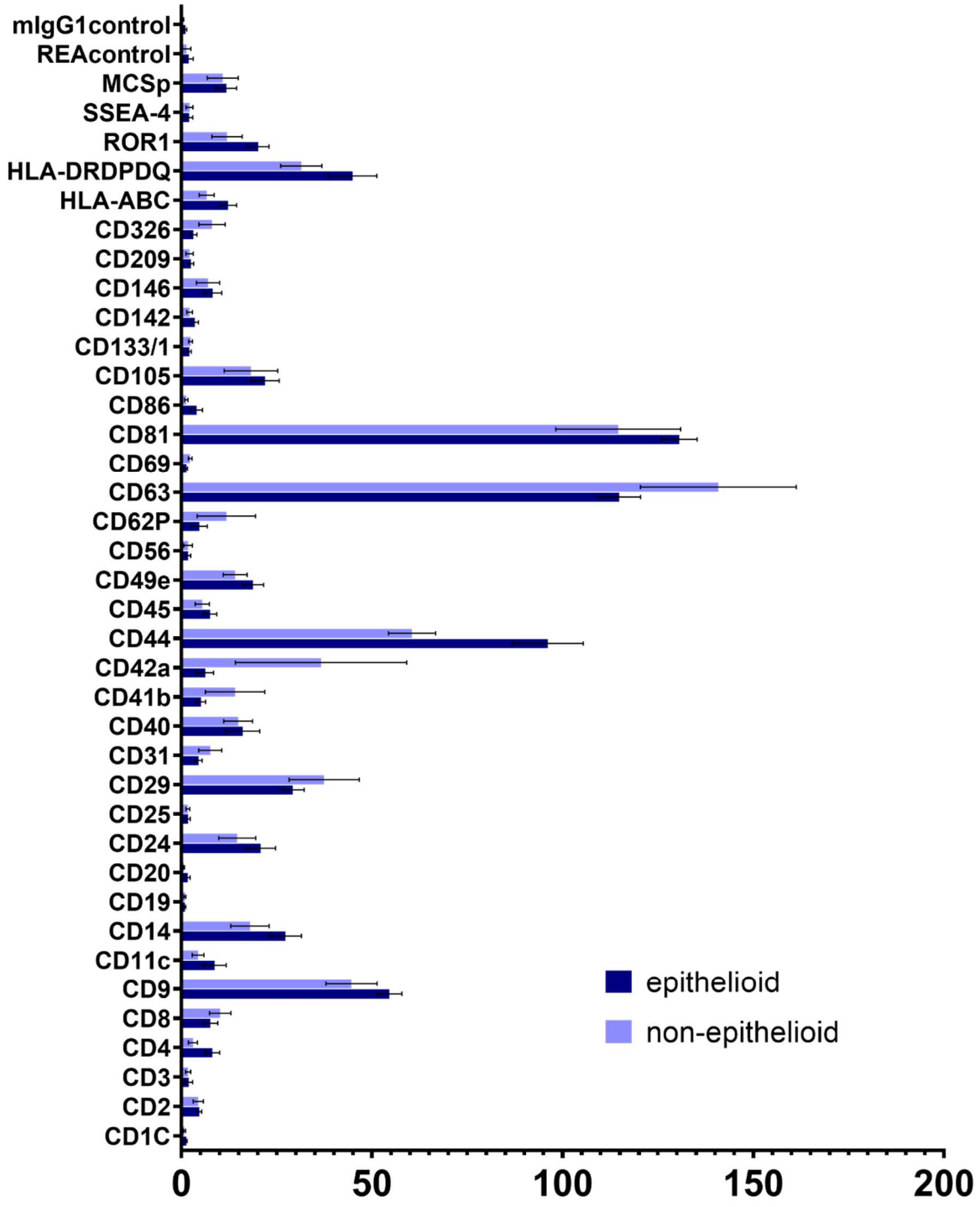

Supplementary Figure 8. EV surface marker profiles among PM subtypes: epithelioid and non-epithelioid. *Extracellular vesicles isolated from pleural effusion samples were analyzed for surface marker expression using a multiplex bead-based flow cytometry assay. Each sample was assessed in triplicate to ensure technical reproducibility. Raw fluorescence intensities were first corrected for background using PBS controls, and then normalized to the average signal of the tetraspanins CD9, CD63, and CD81. Results are expressed as mean ± SEM.*

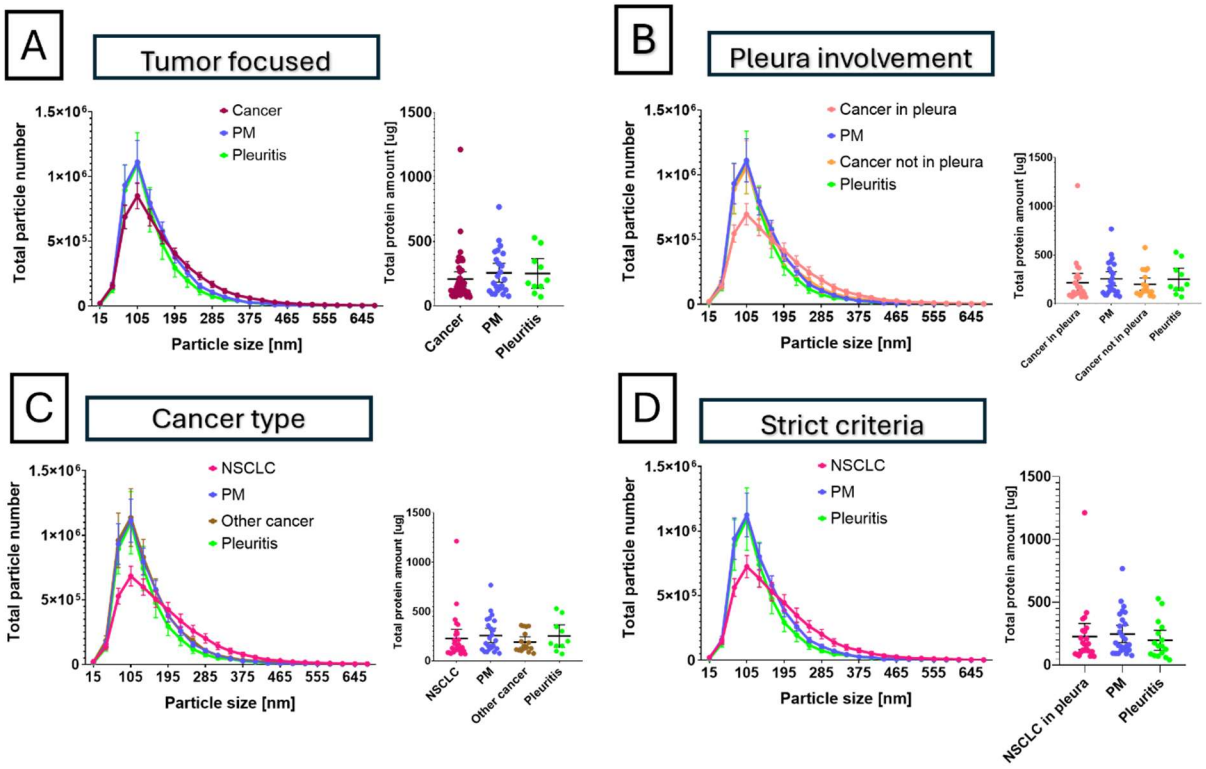

Supplementary Figure 9. EV characteristics in the alternative classifications. *The amount of EVs across particle sizes measured via Nanoparticle Tracking Analysis (NTA), illustrated as mean ± SEM. Total protein amount (mean ± 95% CI) measured by Qubit protein assay. A) "Tumor focused" classification; B) "Pleura involvement" classification; C) "Cancer type" classification; D) "Strict criteria" classification.*

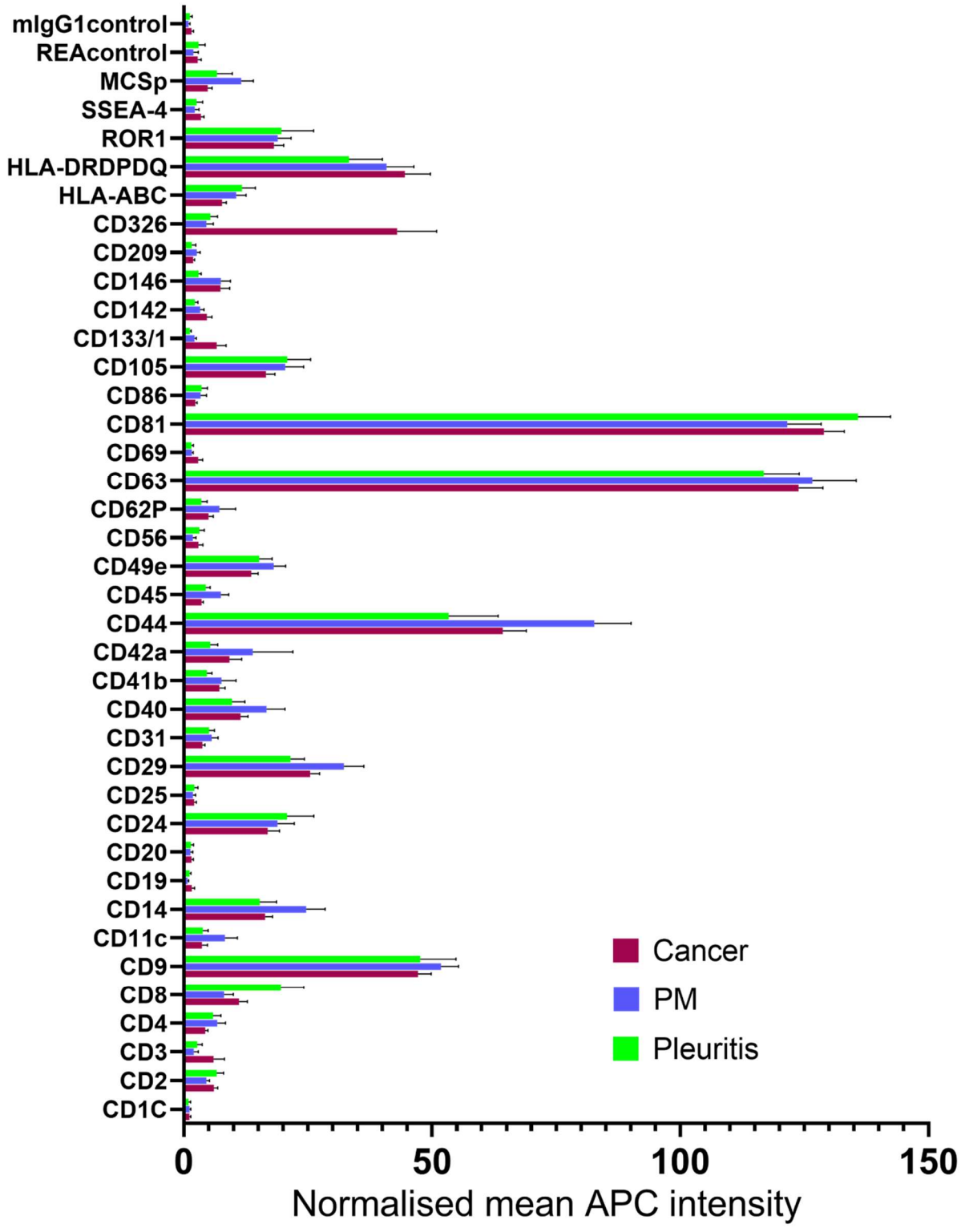

Supplementary Figure 10. EV surface marker profiles in the 'tumor focused' classification. *Extracellular vesicles isolated from pleural effusion samples were analyzed for surface marker expression using a multiplex bead-based flow cytometry assay. Each sample was assessed in triplicate to ensure technical reproducibility. Raw fluorescence intensities were first corrected for background using PBS controls, and then normalized to the average signal of the tetraspanins CD9, CD63, and CD81. Results are expressed as mean ± SEM.*

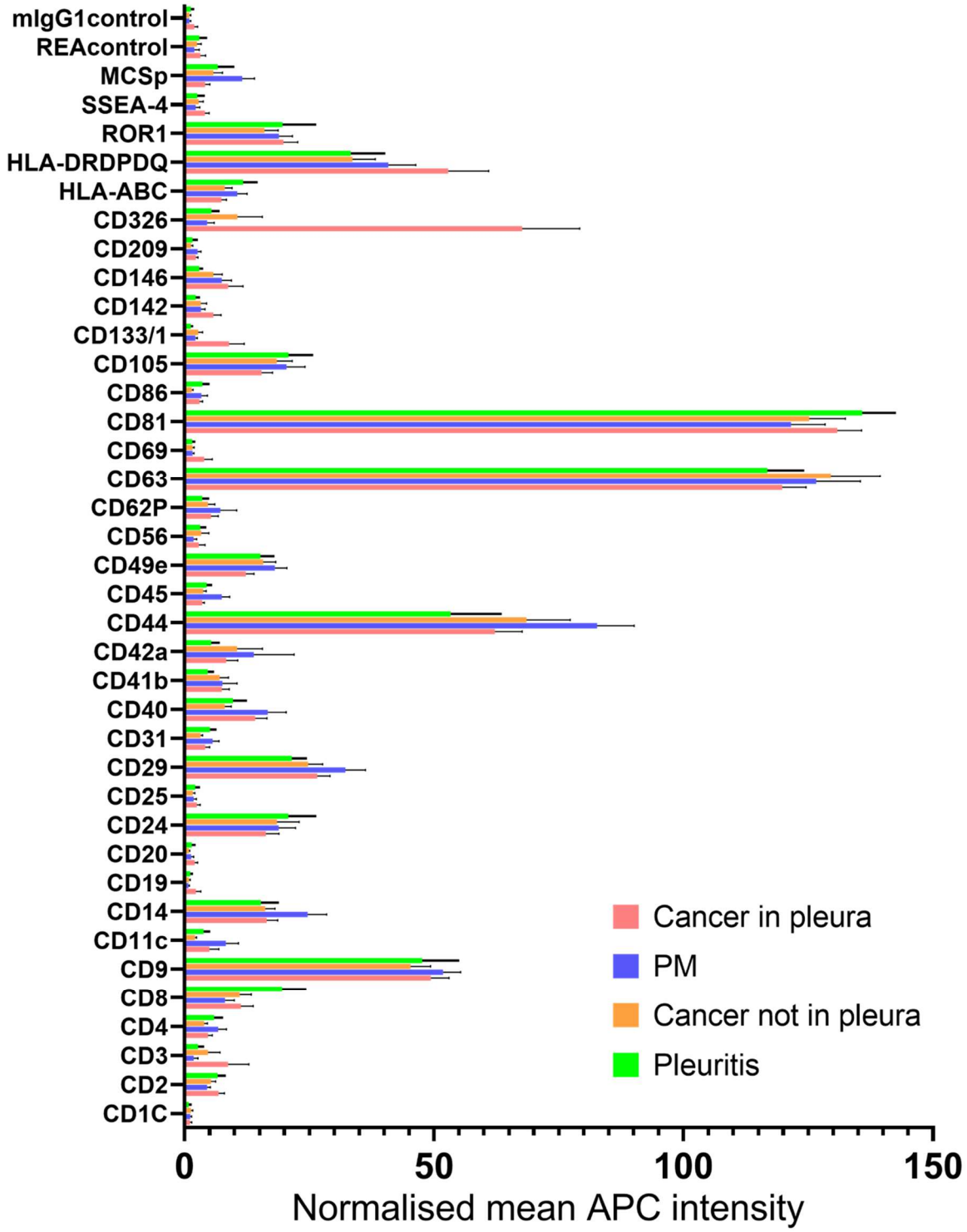

Supplementary Figure 11. EV surface marker profiles in the 'pleura involvement' classification. *Extracellular vesicles isolated from pleural effusion samples were analyzed for surface marker expression using a multiplex bead-based flow cytometry assay. Each sample was assessed in triplicate to ensure technical reproducibility. Raw fluorescence intensities were first corrected for background using PBS controls, and then normalized to the average signal of the tetraspanins CD9, CD63, and CD81. Results are expressed as mean ± SEM.*

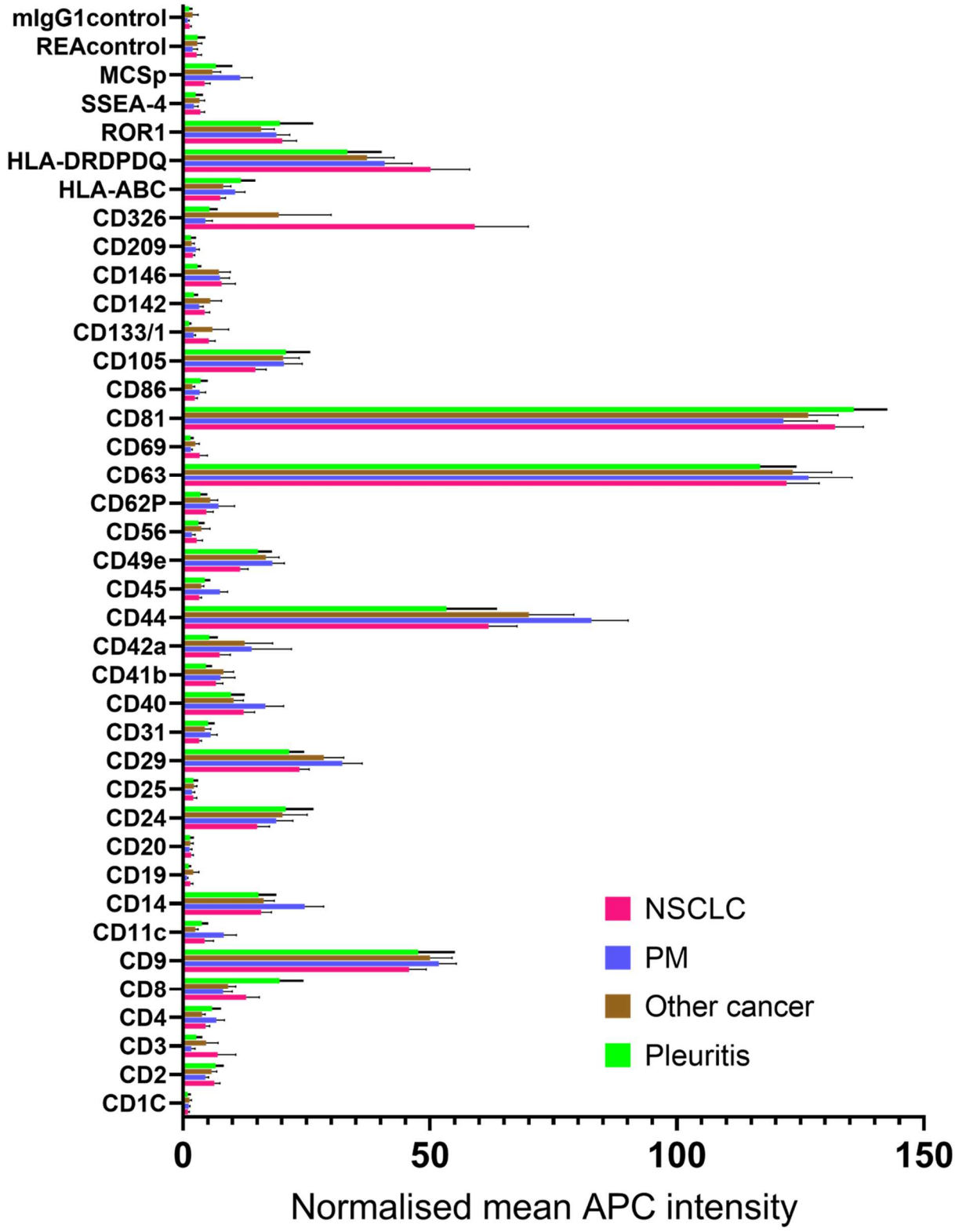

Supplementary Figure 12. EV surface marker profiles in the 'cancer type' classification. *Extracellular vesicles isolated from pleural effusion samples were analyzed for surface marker expression using a multiplex bead-based flow cytometry assay. Each sample was assessed in triplicate to ensure technical reproducibility. Raw fluorescence intensities were first corrected for background using PBS controls, and then normalized to the average signal of the tetraspanins CD9, CD63, and CD81. Results are expressed as mean ± SEM.*

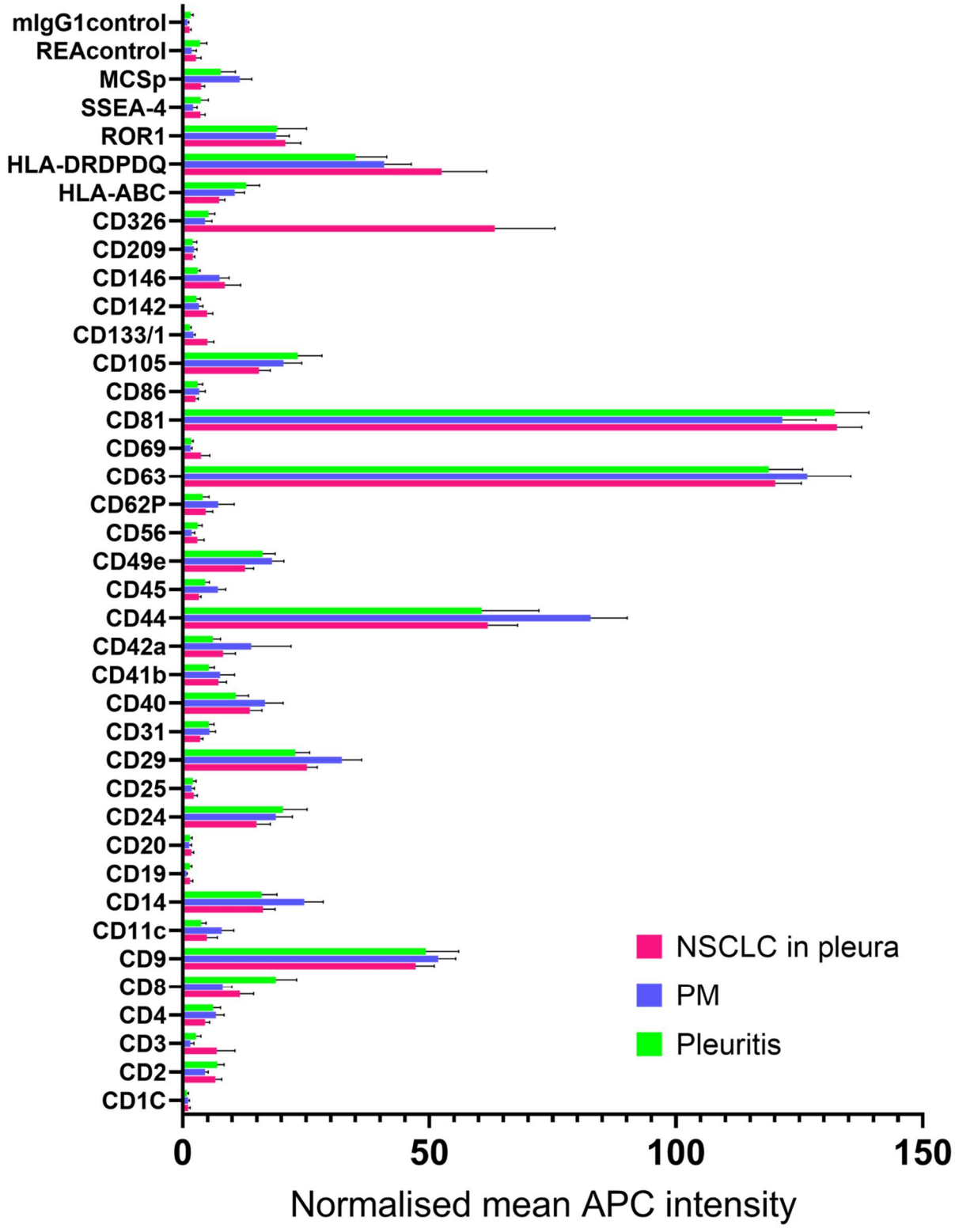

Supplementary Figure 13. EV surface marker profiles in the 'strict criteria' classification. *Extracellular vesicles isolated from pleural effusion samples were analyzed for surface marker expression using a multiplex bead-based flow cytometry assay. Each sample was assessed in triplicate to ensure technical reproducibility. Raw fluorescence intensities were first corrected for background using PBS controls, and then normalized to the average signal of the tetraspanins CD9, CD63, and CD81. Results are expressed as mean ± SEM.*